

A PARAMETRIC STUDY ON PLANETARY GEAR DYNAMICS

A THESIS SUBMITTED TO
THE GRADUATE SCHOOL OF NATURAL AND APPLIED SCIENCES
OF
MIDDLE EAST TECHNICAL UNIVERSITY

BY

VEYSEL YALIN ÖZTÜRK

IN PARTIAL FULFILLMENT OF THE REQUIREMENTS
FOR
THE DEGREE OF DOCTOR OF PHILOSOPHY
IN
MECHANICAL ENGINEERING

JUNE 2018

Approval of the thesis:

A PARAMETRIC STUDY ON PLANETARY GEAR DYNAMICS

submitted by **VEYSEL YALIN ÖZTÜRK** in partial fulfillment of the requirements for the degree of **Doctor of Philosophy in Mechanical Engineering Department, Middle East Technical University** by,

Prof. Dr. Halil Kalıpçılar
Dean, Graduate School of **Natural and Applied Sciences** _____

Prof. Dr. M. A. Sahir Arıkan
Head of Department, **Mechanical Engineering** _____

Prof. Dr. H. Nevzat Özgüven
Supervisor, **Mechanical Engineering Dept., METU** _____

Assoc. Prof. Dr. Ender Ciğeroğlu
Co-Supervisor, **Mechanical Engineering Dept., METU** _____

Examining Committee Members:

Asst. Prof. Dr. Gökhan O. Özgen
Mechanical Engineering Dept., METU _____

Prof. Dr. H. Nevzat Özgüven
Mechanical Engineering Dept., METU _____

Prof. Dr. Nihat Yıldırım
Mechanical Engineering Dept., Gaziantep University _____

Asst. Prof. Dr. M. Bülent Özer
Mechanical Engineering Dept., METU _____

Asst. Prof. Dr. Can U. Doğruer
Mechanical Engineering Dept., Hacettepe University _____

Date: 05.06.2018

I hereby declare that all information in this document has been obtained and presented in accordance with academic rules and ethical conduct. I also declare that, as required by these rules and conduct, I have fully cited and referenced all material and results that are not original to this work.

Name, Last name : Veysel Yalın ÖZTÜRK

Signature :

ABSTRACT

A PARAMETRIC STUDY ON PLANETARY GEAR DYNAMICS

Öztürk, Veysel Yalın

Ph.D., Department of Mechanical Engineering

Supervisor: Prof. Dr. H. Nevzat Özgüven

Co-Supervisor: Assoc. Prof. Dr. Ender Cigeroğlu

June 2018, 188 pages

An extended parametric study is performed for Planetary Gear Train (PGTs) dynamics. A purely torsional, non-linear time-varying model is used for the dynamic simulation of PGTs. Time-dependent stiffness functions are calculated by using dedicated contact mechanics software that is specialized in gears. Multi-term Harmonic Balance Method (HBM) is used for the solution of the model. The fundamental modal characteristics of PGTs are explored. The initial parametric studies are performed for the basic dynamic factors in PGTs, namely for different mesh phasing configurations, varying damping levels, different amounts of backlash and different contact ratios for the mating sun-planet and ring-planet meshes. The effect of ring gear elasticity on torsional PGT dynamics is investigated in detail. The direct effects of parameters, which influence the ring gear elasticity, on PGT dynamics are studied. Tooth Profile Modifications (TPMs), which are one of the most effective means of reducing the vibration in gears, are first studied on spur gears. The differences between the ideal TPM designs for different objective

functions of minimizing Loaded Static Transmission Error (LSTE) and Dynamic Transmission Error (DTE) are analyzed for gears mounted on rigid and compliant shafts. The positive influence of proper TPM applications on increasing the bending fatigue lives are shown by analyzing the stress cycles on TPM applied spur gear pairs. Next, a comprehensive study is performed on the characteristics of ideal TPMs in PGTs. The dependence of ideal TPM designs on modal characteristics of PGTs is shown. The conditions in which the ideal TPM differs from the TPM configurations that minimize LSTE are explored.

Keywords: Planetary gear dynamics, Tooth Profile Modifications, Harmonic Balance Method with multiple harmonics, Loaded Static Transmission Error, elastic ring gears, mesh phasing.

ÖZ

GEZEĞEN DİŞLİ DİNAMIĞI ÜZERİNE PARAMETRİK BİR ÇALIŞMA

Öztürk, Veysel Yalın

Doktora, Makina Mühendisliği Bölümü

Tez Yöneticisi: Prof. Dr. H. Nevzat Özgüven

Ortak Tez Yöneticisi: Doç. Dr. Ender Cigeroğlu

Haziran 2018, 188 sayfa

Gezegen dişli dinamiği için kapsamlı bir parametrik çalışma gerçekleştirilmiştir. Çalışma kapsamında yapılan dinamik benzetim çalışmalarında, yalnızca burulma yönündeki serbestlik derecelerini içeren, doğrusal olmayan değişken zamanlı bir model tercih edilmiştir. Zamana bağlı dişli kavrama direngenlikleri dişlilere özelleşmiş bir kontak mekaniği yazılımı vasıtasıyla hesaplanmıştır. Modeldeki denklemlerin çözümünde çok harmonikli Harmonik Dengeleme Metodu kullanılmıştır. Gezegen dişli dinamiğinin temel dinamik modal özellikleri incelenmiştir. Yapılan ilk parametrik çalışmalarda, farklı kavrama safhalaması özelliklerine, farklı sönümlenme seviyelerine, farklı diş boşluklarına ve güneş-gezegen ve halka-gezegen dişli çiftleri için farklı temas oranlarına sahip gezegen dişli sistemleri incelenmiştir. Halka dişli esnekliğinin gezegen dişli dinamiğine etkileri detaylı bir şekilde incelenmiştir. Halka dişli esnekliğini etkileyen faktörler ile gezegen dişli dinamiği karakteristikleri arasında direk ilişkiler kurulmuştur. Dişli titreşimini azaltmada kullanılan en etkili yöntemlerden biri dişli profil

değişiklikleridir. Dişli profil değişikliklerinin dişli dinamiğine etkileri ilk olarak düz dişliler özelinde çalışılmıştır. Yüklü Statik İletim Hatası'nı (YSİH) azaltmaya yönelik dişli profil değişiklikleri ile Dinamik İletim Hatası'nı (DİH) azaltmaya yönelik ideal dişli profil değişiklikleri arasındaki farklar, esnek ve rijit miller üzerine yerleştirilmiş düz dişliler için ortaya konmuştur. Dişli profil değişikliklerinin dişli eğilme ömürleri üzerindeki olumlu etkileri, uygun dişli profil değişikliği uygulanmış düz dişlilerde gerinim devirlerinin yorulma analizleri vasıtasıyla gösterilmiştir. Bir sonraki adımda, dişli profil değişikliklerinin gezegen dişli dinamiği üzerindeki etkileri incelenmiştir. İdeal dişli profil değişikliklerinin gezegen dişli dinamik mod tiplerine bağlılığı gösterilmiştir. Gezegen dişlilerde YSİH değerini en düşük veren dişli profil değişiklikleri ile dinamik etkileri en aza indirgeyen dişli profil değişikliği tasarımlarının birbirinden ayrıştığı koşullar ortaya konmuştur.

Anahtar kelimeler: Gezegen dişli dinamiği, dişli profil değişikliği, çok harmonikli Harmonik Denge Yöntemi, Yüklü Statik İletim Hatası, halka dişli esnekliği, dişli kavrama safhalaması

*To My Wife,
Diclehan
&
To My Daughter
Defne*

ACKNOWLEDGEMENTS

I would like to thank my supervisor Prof. Dr. H. Nevzat Özgüven and my co-supervisor Assoc. Prof. Dr. Ender Ciğerođlu for their supervision, help and guidance from the beginning to end of this dissertation.

I want to thank Asst. Prof. Dr. Gökhan Özgen and Asst. Prof. Dr. Can Ulař Dođruer for their guidance as members of thesis progress committee.

I would like to thank TÜBİTAK for the funding they have provided during my Ph.D. study through 2211 Scholarship Programme.

I also want to thank my daughter Defne for being a good child and letting her father finish his Ph.D.

My deepest appreciation goes to my wife, Diclehan, for her endless support, patience and encouragement throughout this study. Without her, neither this thesis nor my life would be complete.

TABLE OF CONTENTS

ABSTRACT	v
ÖZ.....	vii
ACKNOWLEDGEMENTS	x
TABLE OF CONTENTS	xi
LIST OF TABLES	xiv
LIST OF FIGURES.....	xvi
LIST OF SYMBOLS	xxi
CHAPTERS	
1 INTRODUCTION.....	1
1.1 Introduction	1
1.2 Literature Survey.....	4
1.3 Motivation, Scope and Objective	8
2 OVERVIEW of PLANETARY GEAR DYNAMICS	11
2.1 Mathematical model.....	11
2.2 Harmonic Balance Method.....	14
2.2.1 Newton’s Method with Arc-Length Continuation	18
2.3 Validation of Multi-Term HBM with Direct Time Integration.....	20
2.4 Modal characteristics of PGTs	25
3 BASIC CONCEPTS IN PLANETARY GEAR DYNAMICS	31
3.1 Mesh Phasing in Planetary Gear Trains	31
3.2 Effects of PGT Model Parameters on PGT Dynamics.....	40

3.2.1 Backlash	40
3.2.2 Damping	46
3.2.3 Contact ratio	49
3.3 Summary and Conclusion	55
4 EFFECTS of RING GEAR ELASTICITY on PGT DYNAMICS	57
4.1 Introduction	57
4.2 Analytical modeling of ring gear elasticity	57
4.3 Effects of ring gear elasticity parameters on PGT dynamic response.....	70
4.4 Summary and Conclusion	78
5 TOOTH PROFILE MODIFICATIONS IN SPUR GEARS	81
5.1 Introduction	81
5.2 Optimum profile modifications for the minimization of dynamic transmission error.....	83
5.3 Optimization of Tooth Bending Fatigue Characteristics using TPMs	95
5.4 Summary and Conclusion	108
6 TOOTH PROFILE MODIFICATIONS IN DYNAMIC ANALYSES of PGTs.....	113
6.1 Introduction	113
6.2 Nonlinear time-variant mathematical model using LSTE.....	113
6.3 Parametric studies.....	121
6.4 Summary and conclusion	133
7 DYNAMIC CHARACTERIZATION OF DOUBLE-RELIEF PROFILE MODIFICATIONS IN PLANETARY GEAR SYSTEMS.....	137
7.1 Introduction	137

7.2 Double-relief TPMs.....	138
7.3 Mathematical Model and Solution Method.....	140
7.4 Validation of Solutions Obtained by Multi-Term HBM.....	145
7.5 Comparison of Dynamic Response for HCR PGTs with Linear Relief and Double-Relief TPMs	147
7.6 Summary and Conclusion	154
8 SUMMARY and FUTURE WORK.....	157
8.1 Summary	157
8.2 Future work	159
REFERENCES.....	161
APPENDIX	
APPENDIX A PUBLISHED PAPERS DURING PHD	169
CURRICULUM VITAE	187

LIST OF TABLES

Table 2-1 Parameters for example planetary gear set used in HBM vs. time integration comparison	21
Table 2-2 Sun-planet mesh stiffness harmonics	22
Table 2-3 Ring-planet mesh stiffness harmonics	22
Table 2-4 Natural frequencies of the example PGT for different boundary conditions	26
Table 2-5 Mass-normalized modal vectors for fixed sun gear configuration	27
Table 2-6 Mass-normalized modal vectors for fixed ring gear configuration	27
Table 2-7 Mass-normalized modal vectors for fixed carrier configuration	28
Table 3-1 Different mesh-phasing configurations for the example PGT in Table 2-1	34
Table 3-2 Natural frequencies for the example PGT in Table 2-1	36
Table 4-1 Parameters for analytical rim model validation study	64
Table 4-2 Parameters of ring gear for mesh stiffness variation study	67
Table 4-3 PGT used in elastic rim dynamic response simulations.....	71
Table 5-1 Properties of gear pair used for comparison of both models	85
Table 5-2 Characteristics of the dynamic system.....	88
Table 5-3 Details of the example cases	92
Table 5-4 S-N Curve Properties for 42CrMo6.....	97
Table 5-5 Example spur gear pair	100
Table 5-6 Duty cycle under consideration	100
Table 5-7 Rainflow stress cycles for Case 3	102
Table 5-8 Fatigue live summary for the gear pair	103
Table 5-9 Cycles to fail for the respective stress cycles.....	104
Table 5-10 Damage summaries obtained for different parameter configurations	106
Table 6-1 Example planetary gear set used in analytical model validation	116

Table 6-2 Example planetary gear set used in HBM vs. time integration comparison	120
Table 6-3 Natural modes of the example PGT with no TPM	129
Table 6-4 TPMs leading to minimum LSTE for sun-planet and ring-planet meshes	132
Table 7-1 Parameters of example PGT	146

LIST OF FIGURES

Figure 1-1 A schematic of a simple planetary gear train [1].....	1
Figure 1-2 Planetary gearbox for Bell-47 helicopter [4].....	3
Figure 1-3 Planetary gearbox for a wind turbine [5].....	3
Figure 2-1 Schematic for the PGT dynamics model	12
Figure 2-2 Exact sun-planet mesh stiffness and 6-harmonic approximation	23
Figure 2-3 Exact ring-planet mesh stiffness and 6-harmonic approximation	23
Figure 2-4 TI vs HBM comparison for sun displacement (rms)	24
Figure 2-5 TI vs HBM comparison for planet displacement (rms).....	25
Figure 2-6 Mode shapes for fixed-ring configuration	29
Figure 3-1 Example sun-planet mesh stiffness plots for a) sequentially-phased, b) in-phase, c) counter-phased mesh configurations. Note that in b), all stiffness curves overlap with each other while in c), P1-S overlaps with P3-S and P2-S overlaps with P4-S	33
Figure 3-2 Sun-planet mesh displacement (rms) for different mesh phasing configurations given in Table 3-1	35
Figure 3-3 Ring-planet mesh displacement (rms) for different mesh phasing configurations given in Table 3-1	35
Figure 3-4 Sun-planet mesh displacement for 3 rd configuration, excited modes and excitation sources	37
Figure 3-5 Sun-planet displacements (rms) for PGTs with different number of planets with Sequentially-phased (SP) and Counter-phased (CP) configurations .	38
Figure 3-6 Ring-planet displacements (rms) for PGTs with different number of planets with Sequentially-phased (SP) and Counter-phased (CP) configurations .	38
Figure 3-7 Sun displacement (rms) response with different amount of backlash ..	41
Figure 3-8 Planet displacement (rms) response with different amount of backlash	41
Figure 3-9 Dynamic sun-planet elastic force (rms) for different amount of backlash	42

Figure 3-10 Dynamic ring-planet elastic force (rms) for different amount of backlash	43
Figure 3-11 Sun displacement (rms) for $b=0.5\text{mm}$ for sun-planet and $b=0.005\text{mm}$ for ring-planet pairs, respectively. Region 1: No-impact for sun-planet, single-sided impact for ring-planet, Region 2: No-impact for sun-planet, double-sided impact for ring-planet, Region 3: Single-sided impact for sun-planet, double-sided impact for ring-planet pairs.....	44
Figure 3-12 Time histories for sun-planet and ring-planet mesh forces, a) $\omega=2553\text{Hz}$, Region 1, b) $\omega=2600\text{Hz}$, Region 2, c) $\omega=2660\text{Hz}$, Region 3.	45
Figure 3-13 Sun displacement (rms) response with different amount of backlash for ring-planet pair – no backlash for sun-planet.....	46
Figure 3-14 Dynamic sun displacement (rms) for different damping ratios.....	48
Figure 3-15 Dynamic elastic sun-planet force (rms) for different damping ratios	48
Figure 3-16 Dynamic sun-planet elastic forces (rms) for different contact ratios of sun-planet gears.....	50
Figure 3-17 Dynamic ring-planet elastic forces (rms) for different contact ratios of ring-planet gears	51
Figure 3-18 Sun displacement (rms) for different contact ratios of ring-planet gears	52
Figure 3-19 Dynamic sun-planet elastic forces (rms) for different contact ratios of ring-planet gears.....	52
Figure 3-20 Ring-planet displacement (rms) for different contact ratios of sun-planet gears	53
Figure 3-21 Dynamic ring-planet elastic forces (rms) for different contact ratios of sun-planet gears.....	54
Figure 4-1 Uniformly deformed curved beam	59
Figure 4-2 Ring gear model as a combination of uniformly deformed curved beams	61
Figure 4-3 Mesh displacements and mesh forces imposed on the rim structure....	63

Figure 4-4 1D FE model with applied forces and boundary conditions	65
Figure 4-5 Comparison of radial displacement results between analytical model and FE model	66
Figure 4-6 Variation of mesh stiffness between constraints for different rim thickness parameters.....	68
Figure 4-7 Effect of number of constraints (N_c) for the mesh stiffness of the ring planet pair, $T = 0.04$	69
Figure 4-8 Ring-planet mesh stiffness for a PGT with 4 planets and 12 constraints around ring gear, a) Rigid ring gear, b) Elastic ring gear.....	70
Figure 4-9 Sun-planet displacement (rms) comparison for elastic vs. rigid ring gear	72
Figure 4-10 Sun displacement (rms) for different values of rim thickness values (T).....	73
Figure 4-11 Planet displacement (rms) for different values of rim thickness values (T).....	73
Figure 4-12 Sun-planet dynamic elastic force (rms) for different rim thickness values (T) between 1000-9000 rpm	74
Figure 4-13 Sun-planet dynamic elastic forces (rms) for different rim thickness values (T) between 12000-20000 rpm	75
Figure 4-14 Ring-planet dynamic elastic forces (rms) for different rim thickness values (T) between 1000-20000 rpm	76
Figure 4-15 Sun displacement (rms) for different number of constraints (N_c).....	76
Figure 4-16 Sun-planet dynamic elastic force (rms) for different number of constraints (N_c), 1000-9000 rpm.....	77
Figure 4-17 Ring-planet dynamic elastic force (rms) for different number of constraints, 12000-60000 rpm.....	78
Figure 5-1 Linear and parabolic profile modifications	82
Figure 5-2 Model comparison for a) $\zeta=0.1$ and b) $\zeta=0.05$	86
Figure 5-3 Second MDOF model configuration	87

Figure 5-4 Response of MDOF and SDOF models for “short shafts” case.....	89
Figure 5-5 Response of MDOF and SDOF models for “long shafts” case.....	90
Figure 5-6 Sample optimization results for Case 1 and Case 2	93
Figure 5-7 Sample optimization results for Case 3, Case 4 and Case 5.....	95
Figure 5-8 Procedure for gear tooth bending life estimation	99
Figure 5-9 Tooth root normal stress results	101
Figure 5-10 Stress cycle information for the sample case	104
Figure 5-11 Tooth root normal stress time histories for the optimal TPM configuration	107
Figure 6-1 A view of the FE model for the example planetary gear train used in validation study	117
Figure 6-2 Comparison of the frequency response for analytical and FE models	118
Figure 6-3 Time histories for sun displacement at a) 1680rpm and b) 2230 rpm	119
Figure 6-4 Comparison of HBM and time integration response.....	121
Figure 6-5 Maximum dynamic to static sun-planet mesh force ratios for a) Torque=1600Nm, linear TPM, b) Torque=1600Nm, parabolic TPM, c) Torque=2400Nm, linear TPM, d) Torque=2400Nm, parabolic TPM, e) Torque=3200Nm, linear TPM, f) Torque=3200Nm, parabolic TPM, g) Torque=4000Nm, linear TPM, h) Torque=4000Nm, parabolic TPM.	123
Figure 6-6 Maximum dynamic to static mesh force ratio for a) Torque=1600Nm, parabolic TPM, sun-planet, b) Torque=1600Nm, parabolic TPM, ring-planet, c) Torque=4000Nm, linear TPM, sun-planet, d) Torque=4000Nm, linear TPM, ring-planet.....	125
Figure 6-7 Maximum dynamic displacement response for ideal TPMs for a) Torque=1600Nm, b) Torque=2400Nm, c) Torque=3200Nm, d) Torque=4000Nm, e) Torque=4800Nm.....	127
Figure 6-8 Effect of TPMs on rms sun-planet and ring-planet mesh displacements for a) 2500-6000 sun rpm, b) 6000-10000 sun rpm, c) 12000-16000 sun rpm....	130
Figure 7-1 Combined tooth profile plot for a gear pair with double-relief TPM.	140

Figure 7-2 Comparison of sun gear displacement (rms) obtained by using TI and HBM.....	147
Figure 7-3 LSTE for double-relief (top) and linear TPMs (bottom). The load is increased from no-load (curves at the bottom of the plots) to maximum design load in 10% intervals.....	148
Figure 7-4 Sun gear displacement (rms) for a) 50%, b) 60%, c) 70%, d) 80%, e) 90% and f) 100% design load.....	149
Figure 7-5 Planet gear displacement (rms) for a) 50%, b) 60%, c) 70%, d) 80%, e) 90% and f) 100% design load.....	150
Figure 7-6 Maximum dynamic force for double-relief and short-relief cases in the interval of 50-100% of the design load	150
Figure 7-7 Sun gear displacement (rms) for a) 20%, b) 30%, c) 40%, d) 50% design load	152
Figure 7-8 Maximum dynamic force for double-relief and short-relief cases in the interval of 20-50% of the design load	153

LIST OF SYMBOLS

FE	Finite element
M	Equivalent mass
t	Time
c	Viscous damping coefficient
z	Mesh displacement
g	Nonlinear spring force
k	Stiffness
f	Equivalent force
x	Displacement
T	Torque
b	Half of the backlash between mating teeth
r	Base radius of gear
n_p	Number of planets
e	Error term on mesh displacement
S	Vector of nonlinear equations
ω	Frequency
n	Harmonic index
HPSTC	Highest point of single tooth contact
LPSTC	Lowest point of single tooth contact

rms Root mean square

Subscripts

s Sun gear

sp Sun-planet mesh

si i^{th} sun-planet mesh

r Ring gear

rp Ring-planet mesh

ri i^{th} ring-planet mesh

c Carrier

p Planet

CHAPTER 1

INTRODUCTION

1.1 Introduction

A planetary gear train (also known as epicyclic gear train) consists of two central geared members. The inner central member is named as “sun gear” whereas the outer central member which is an internal gear is called “ring (annulus) gear”. A number of “planet gears” (number of planets usually between 3 and 8) revolve around the sun gear with the help of a carrier, on which the planet gears are mounted. The planet gears also mesh with the ring gear. Figure 1-1 shows the schematic of a simple planetary gear train (PGT).

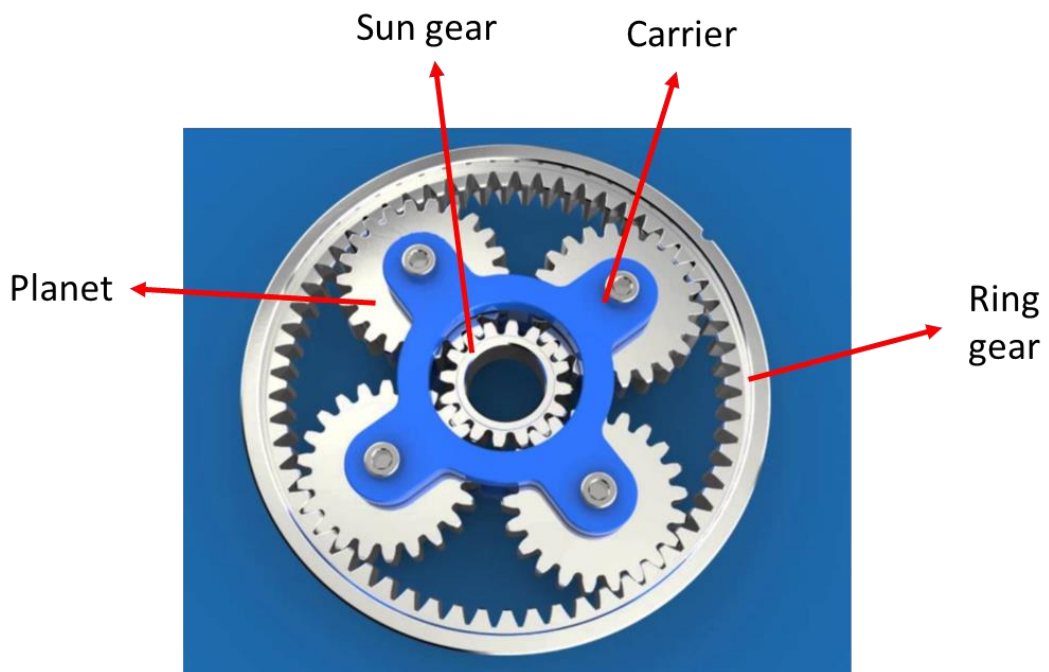


Figure 1-1 A schematic of a simple planetary gear train [1]

Different speed and torque conversion ratios are obtained simply by different assignments of input, output and the fixed members between sun gear, ring gear and carrier. Since the power splits into a number of parallel planet branches, PGTs typically have higher power density (power transmitted / total volume) compared to counter-shaft gearbox configurations. Their coaxial design allows compact gearbox cross-sections with no or little radial support (bearings) requirements. All gear mesh and bearing forces on the transverse plane of the gear set cancel out nominally, leaving only pure torsion. They are less sensitive to variety of manufacturing errors since they can self-center (or deflect) to compensate for such errors. Moreover they are perceived to be quieter than their counter-shaft counterparts.

PGTs are used extensively in automotive, rotorcraft and wind energy industries. Figure 1-2 and Figure 1-3 show examples for PGTs that are used in helicopters and wind turbines, respectively. Although they are being used in quiet a wide range of applications for many years, problems related to dynamic behavior of planetary gears are still common. In addition to the fatigue related problems because of the vibration; noise is also an important concern for many applications, including rotorcraft and wind turbine industries. In helicopters, planetary gears are held responsible for being the main source of cabin noise [2]. Cost of maintenance is an important factor in wind turbine industry because of the significant downtimes. It has been shown that planetary gearbox failures due to dynamic loading of the components is a very common failure mode for wind turbines [3]. Planetary gear dynamics studies are aimed at understanding the physical phenomena behind the problems similar to these examples and finding remedies for them.

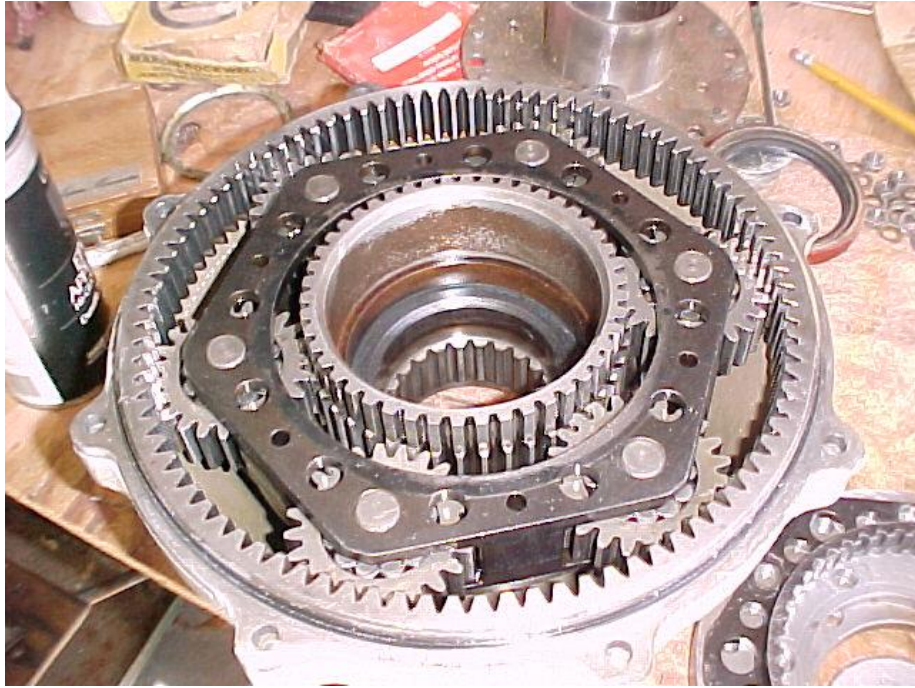


Figure 1-2 Planetary gearbox for Bell-47 helicopter [4]



Figure 1-3 Planetary gearbox for a wind turbine [5]

A detailed literature survey is presented here, to give the state of the art in the field and discuss the further needs in planetary gear dynamics studies.

1.2 Literature Survey

Although most of the PGT dynamics studies available in the literature stem from the research in parallel-axis gearing, the literature survey information provided here is going to be mostly limited to PGT dynamics studies. However it should be underlined here that fundamental knowledge regarding gear dynamics was obtained through many precious documented works in the literature, before going forward with PGT dynamics studies.

The wide use of PGTs also made the PGT dynamics studies attractive for many researchers. The studies for PGT dynamics stem back to 1970s, following the start of the gear dynamics studies in 1960s [6]. Most of these studies aimed at the ultimate goal of reducing the vibration levels in PGTs, since vibration-induced dynamic loads are one of the major sources of failures of these components. Depending on the applications, PGT failures may result in serious consequences, ranging from extended downtimes (e.g. for wind turbines) to loss of lives (e.g. for helicopters).

The use of lumped-parameter models is quite popular for PGT dynamics studies. Depending on the nature of the PGT design under consideration, the lumped-parameter models vary from purely torsional (1D) models (e.g. models used in [7,8]) to 3D models where the out-of-plane vibration is also considered along with the vibrations in torsional rotation and in-plane translation directions. The models used in [9,10] can be given as examples to those 3D models mentioned.

Similar to parallel-axis gear systems, the modeling of the mesh stiffness and tooth contact loss phenomenon play an important role in the accuracy of the dynamic simulation of PGTs. For modal analysis of PGTs, models employing constant mesh stiffness values for sun-planet and ring-planet meshes can be preferred as it is the case in the study of Kahraman [11]. In forced response analysis of a PGT, this modeling approach is also used frequently. In this methodology, forcing term is modeled as the static deflection of the respective meshes multiplied by a constant stiffness term. In parallel-axis gear terminology, this deflection is defined as the static transmission error. However, the use of this terminology in planetary gear systems may lead to ambiguity, as it is not clear whether one refers to the individual error due to the deflection of a single gear-pair or the global deflection of a planetary gear system [6]. Although this modeling approach is shown to have limitations when compared to time-varying mesh stiffness models [12], it also offers advantages in terms of model simplicity and ability to represent the fundamental features of PGT dynamics. References [13,14] are examples to the studies using this modeling approach.

During the rotation of the gears, the stiffness of the contact between meshing gears vary, due to the geometry of the gears and the change in the number of teeth in contact. The parametric excitation due to the time-varying stiffness is especially important for PGTs comprised of spur gears. The effects of these parametric excitations are also studied for PGTs [15,16]. However calculating mesh stiffness as a function of time is usually a complicated task. The calculation of the time-varying mesh stiffness is possible through using finite element methods or dedicated computational tools specialized in loaded tooth contact analysis.

Models that include variable mesh stiffness and tooth contact loss phenomenon lead to more accurate forced response predictions. Both phenomena are especially important in PGTs with spur gears as the experimental studies [17,18] showed

strong nonlinear behavior for spur gears. Although similar experiments are not conducted yet for PGTs, the analytical studies performed for PGTs showed also that nonlinear effects can also be expected for PGTs in general [16,19–22].

PGTs show distinct modal properties mostly due to their cyclic symmetry and these modal characteristics are also analyzed in the literature. In the earlier studies of Cunliffe [23] and Botman [24], which were limited to example planetary gear sets consisting of 3 planets, a first classification was made as the natural modes are categorized as “axisymmetric” and “nonaxisymmetric” modes. An improved and more detailed classification is made by Kahraman for the torsional modes [11]. Later the classification is extended to 2D and 3D models by Parker [25]. Ericson and Parker also correlated these findings with experiments [26]. Various researchers extended the related studies for simple PGTs to compound PGTs [27–29].

As the studies on the modal characteristics of PGTs showed, the phasing relationships between gear pairs are also very important regarding the forced response characteristics of PGTs. These phase relationships depend on the number of planets and number of gear teeth of sun and ring gears [30]. The effectiveness of mesh phasing in reducing the PGT vibration is studied extensively by many researchers [31–33]. It is possible to suppress some of the natural modes of a PGT by configuring the design via modification of the mentioned parameters. This approach is very effective in reducing the dynamic response of PGTs [34].

In some applications like rotorcraft PGTs, use of thin-rimmed ring gears is preferred due to the advantages in weight and load-sharing [35]. Kahraman et al. [36] used a combined FE-contact mechanics tool to study the dynamic characteristics of such PGTs. An analytical model incorporating the effect of elastic thin ring gears with time-varying mesh stiffness is used by Canchi and Parker [33] in their related study. Abosleiman and Velez combined their lumped-parameter model with a FE

formulation to analyze the effects of ring gear elasticity [37,38]. Chen et al. [39] performed time-integration simulation on their model which includes the torsional effects of having compliant ring gears. The effects of having compliant members in a PGT are extensively studied by Helsen et al. [40–42] for wind turbines both analytically and experimentally.

The initial studies on profile modifications were mainly focused on the effect of these modifications on reducing the loaded static transmission error (LSTE) on parallel-axis gearing. LSTE optimization efforts go back to the study of Tavakoli and Houser in 1986 [43]. In their study, an objective function based on the mean value of the transmission error harmonics under different design torques was used in search of optimal tooth profile. In 2005, Fonseca et al. [44] employed a genetic optimization algorithm to the same static model of Tavakoli and Houser. These studies reveal that optimization efforts based on LSTE fluctuation minimization are very effective when torque is the only parameter considered regarding the operational characteristics of gear pairs. Different concepts regarding the application of profile modifications were studied in order to improve the effectiveness of these modifications at different torque levels [45].

Afterwards, effect of profile modifications on reducing the vibration in geared systems was studied by using the direct approach of including profile modifications in the dynamic models. The references [12,18,46] are only a few examples to the mentioned studies. The experiments on parallel-axis have also shown us that the use of proper tooth profile modifications is a very effective way of reducing the gear vibration [47,48]. Further improvement towards reducing actual vibration levels can be achieved via optimization efforts targeted at DTE minimization. Bonori et al. [49] performed dynamic analyses on a spur gear pair to check the quality of their genetic algorithm based LSTE optimization method. In 2011, Faggioni et al. [50] developed an optimization model with 8 parameters and concluded that optimization

which is directly targeted minimizing DTE produced better results than an optimization study which aims to minimize LSTE for spur gears.

Similar to parallel-axis gear systems, profile modifications are also effective in decreasing the vibration levels in PGTs. Abousleiman and Vex [37] showed that it is possible to eliminate resonances by applying proper profile modifications. In another study, Bahk and Parker [51] studied the effect of linear profile modifications on PGTs and concluded that a full-system approach is necessary in evaluating the effects of profile modifications on PGTs. They showed that static evaluations for individual sun-planet and ring-planet pairs are inadequate. When compared to the parallel-axis gear systems, because of the more complex nature of PGTs, there is still a need for studies which would address the different aspects of the PGT design and tooth profile modifications together.

1.3 Motivation, Scope and Objective

Gear dynamics have been extensively studied during the last 40 years. PGTs present unique features when compared to parallel-axis geared systems, which need special attention. The number of studies which focused on planetary gear dynamics started to increase steadily during the 2000s.

Many parameters, including mesh stiffness of gears, nonlinearity due to backlash, damping characteristics, component elasticity, errors due to manufacturing and assembly, profile modifications and mesh phasing, have strong effects on dynamic characteristics of planetary gears. Some of these parameters are irrelevant for the parallel-axis gear systems, whereas some of them affect the dynamics of PGTs in a different manner when compared with how they affect parallel-axis gear sets. Although the influence of some of these parameters on PGT dynamics have been

studied extensively, there is still need for research in order to fully understand the influence of some parameters on PGT dynamics.

This dissertation aims to address the following topics:

- A review of planetary gear dynamics and torsional modal characteristics of PGTs based on the analytical formulations using a nonlinear time-variant modeling scheme. Information about solution using HBM with arc-length continuation (Chapter 2).
- Parametric study related to PGTs with different mesh phasing configurations. Investigations on the effects of backlash, level of damping, external force and gear mesh contact ratio on PGT dynamics (Chapter 3).
- Investigation of rim stiffness effects on torsional dynamics of PGTs. Study of the effects of rim design parameters on PGT dynamics (Chapter 4).
- Analyses of the effects of TPMs on spur gear dynamics by using both SDoF and MDoF dynamic models. Demonstration of the effects of proper TPMs on reducing the dynamic loads and increasing the bending fatigue lives of spur gears (Chapter 5).
- Investigation of the effects of TPMs on PGT dynamics. The relationship between the static mesh displacements and dynamic response for various natural modes of PGTs. The sensitivity of TPM designs to dynamic response considering applied loads, operational speed intervals, manufacturing tolerances, wear, etc. (Chapter 6).

- Investigation of the effects of double-relief TPMs on the dynamic characteristics of PGTs with high contact ratio (HCR) spur gears. Comparisons between dynamic responses of PGTs with linear TPMs and PGTs with double-relief TPMs (Chapter 7).

CHAPTER 2

OVERVIEW of PLANETARY GEAR DYNAMICS

2.1 Mathematical model

In this study, a purely torsional mathematical model, as shown in Figure 2-1, is used. It is a time-varying nonlinear model, including time-varying stiffness and backlash nonlinearity. Kahraman [9] showed that a purely torsional model for PGT dynamics is reasonably accurate even for the cases where floating central members are present. Each gear blank is assumed to be rigid and only the mesh stiffness between interfacing gear teeth is modeled. Sun and ring gears are mounted on rigid bearings. Similarly planets are mounted on rigid carriers through rigid planet bearings. Each gear and the planet carrier are assumed to move in the torsional direction only, i.e. the model has (number of planets + sun + ring + carrier) degrees of freedom. Damping between the mating gear teeth is modeled as viscous damping with constant damping coefficients. The mesh stiffness is modeled with a time-varying parameter in order to simulate the variation of stiffness during rotation of the gears caused by changing contact point and number of teeth in contact. Variation of mesh stiffness is known to act as a parametric excitation to the dynamic system.

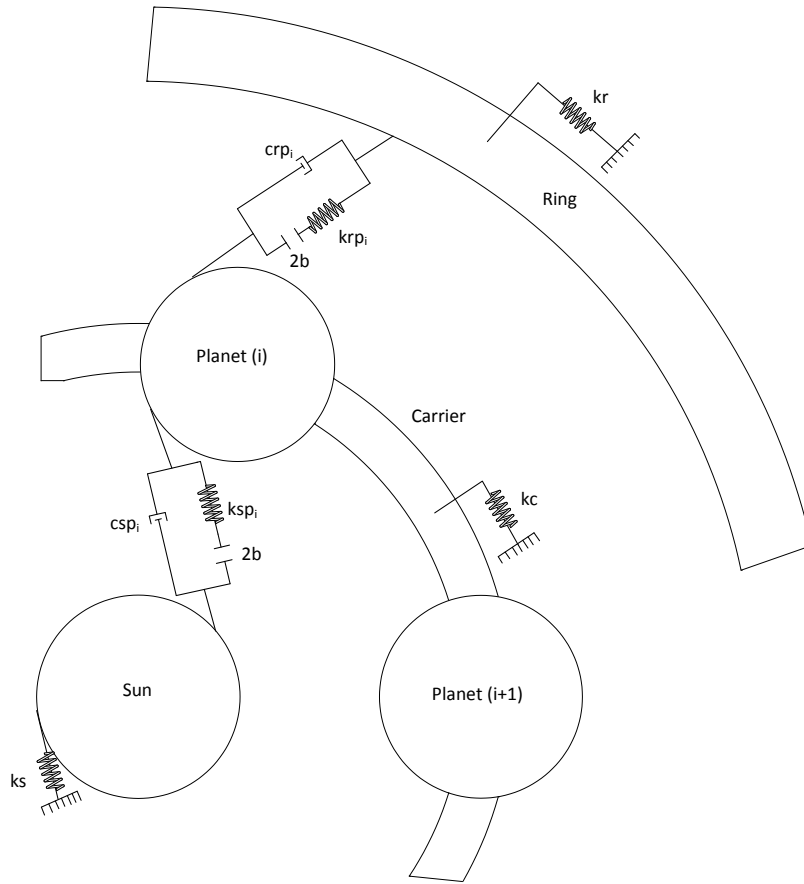


Figure 2-1 Schematic for the PGT dynamics model

Equations of motion for the torsional model given in Figure 2-1 can be written as follows

$$M_s \ddot{x}_s(t) + c_{sp} \sum_{i=1}^{n_p} \dot{z}_{si}(t) + \sum_{i=1}^{n_p} g_{si}(t) + k_s x_s(t) = f_s, \quad (2.1)$$

$$M_r \ddot{x}_r(t) + c_{rp} \sum_{i=1}^{n_p} \dot{z}_{ri}(t) + \sum_{i=1}^{n_p} g_{ri}(t) + k_r x_r(t) = f_r, \quad (2.2)$$

$$M_c \ddot{x}_c(t) - c_{sp} \sum_{i=1}^{n_p} \dot{z}_{si}(t) - c_{rp} \sum_{i=1}^{n_p} \dot{z}_{ri}(t) - \sum_{i=1}^{n_p} g_{si}(t) - \sum_{i=1}^{n_p} g_{ri}(t) + k_c x_c(t) = f_c, \quad (2.3)$$

$$M_i \ddot{x}_i(t) + c_{sp} \dot{z}_{si}(t) - c_{rp} \dot{z}_{ri}(t) + g_{si}(t) - g_{ri}(t) = 0, \quad \text{for } i=1, 2, \dots, n_p, \quad (2.4)$$

where,

$$M_s = \frac{I_s}{r_s^2}, \quad M_r = \frac{I_r}{r_r^2}, \quad M_c = \frac{I_c}{r_c^2} + n_p m_i, \quad (2.5)$$

$$f_s = \frac{T_s}{r_s}, \quad f_r = \frac{T_r}{r_r}, \quad f_c = \frac{T_c}{r_c}. \quad (2.6)$$

Here $x_s(t)$ and $x_r(t)$ denote the linear displacement of sun gear and ring gear along the respective line of actions (angular rotation times the gear base radii). $x_c(t)$ denotes the linear displacement of the carrier (angular rotation times the radius to the center of a planet); whereas, $x_i(t)$ is the linear displacement of the i^{th} planet along its line of action. $z_{si}(t)$ and $z_{ri}(t)$ are mesh displacement functions for the i^{th} sun-planet and ring-planet meshes, respectively. They can be expressed as

$$z_{si}(t) = x_s(t) + x_i(t) - x_c(t) - e_{si}(t), \quad (2.7)$$

$$z_{ri}(t) = x_r(t) - x_i(t) - x_c(t) - e_{ri}(t), \quad (2.8)$$

where $e_{si}(t)$ and $e_{ri}(t)$ are the geometric error terms for the i^{th} sun-planet and ring-planet meshes. The error terms $e_{si}(t)$ and $e_{ri}(t)$ are used both for profile deviations as well as the intended tooth profile modifications (TPMs). M_s , M_r and M_c are the equivalent masses for sun, ring and carrier, respectively. Similarly, f_s , f_r and f_c denote the equivalent external forces applied on sun, ring and carrier, respectively. k_s , k_r and k_c are the terms representing the constant stiffness between ground and the respective components. Note that for the fixed member, the respective stiffness

value can be assumed to be infinite; whereas, they can be set equal to zero for the other members. c_{sp} and c_{rp} are the constant damping coefficients for sun-planet and ring-planet meshes, respectively. n_p stands for the number of planets; whereas, m_i is the mass of the i^{th} planet. $g_{si}(t)$ and $g_{ri}(t)$ are the nonlinear spring force functions due to the backlash between the mating gear teeth for the sun-planet and ring-planet meshes, respectively. Loss of contact between the teeth of mating gears is one of the most dominant and the most studied nonlinear phenomena in gear dynamics studies. The sudden loss of contact results in a softening type of behavior that results in shift of resonance frequencies to the left in frequency domain. The backlash is included in the model as a gap element. Therefore the nonlinear spring force functions can be defined as

$$g_{si}(t) = \begin{cases} k_{si}(t)[z_{si}(t) - b] & \text{for } z_{si}(t) > b \\ 0 & \text{for } -b \leq z_{si}(t) \leq b \\ k_{si}(t)[z_{si}(t) + b] & \text{for } z_{si}(t) < -b \end{cases}, \quad (2.9)$$

and

$$g_{ri}(t) = \begin{cases} k_{ri}(t)[z_{ri}(t) - b] & \text{for } z_{ri}(t) > b \\ 0 & \text{for } -b \leq z_{ri}(t) \leq b \\ k_{ri}(t)[z_{ri}(t) + b] & \text{for } z_{ri}(t) < -b \end{cases}. \quad (2.10)$$

One can refer to “List of Symbols” section given at the beginning of the thesis, for the remaining symbols that are not explained here.

2.2 Harmonic Balance Method

Solution of differential equations of motion using direct time integration is computationally expensive for parametric studies of planetary gear dynamics that

require a vast number of simulations. Since steady state solutions are of interest, in this study, Harmonic Balance Method (HBM) is used. HBM is based on the simple idea where an assumed form of periodic solution, which is expressed as Fourier series, is inserted into the nonlinear equation where the periodic excitation is similarly expressed as Fourier series and coefficients of similar terms are balanced to determine the unknown ones.

Using multi-term HBM, nonlinear differential equations of motion given by Eqs. 2.1 - 2.4 can be converted into a set of nonlinear algebraic equations. The periodic parametric excitations for both sun-planet and ring-planet meshes given by Eqs. 2.9 and 2.10, can be represented in Fourier series as

$$k_{si}(t) = k_{si,1} + \sum_{n=1}^N (k_{si,2n} \cos(n\omega t) + k_{si,2n+1} \sin(n\omega t)), \quad (2.11)$$

$$k_{ri}(t) = k_{ri,1} + \sum_{n=1}^N (k_{ri,2n} \cos(n\omega t) + k_{ri,2n+1} \sin(n\omega t)). \quad (2.12)$$

Similarly, the periodic error terms which may represent gear profile errors or TPMs, i.e. $e_{si}(t)$ and $e_{ri}(t)$, can be expressed as

$$e_{si}(t) = E_{si,1} + \sum_{n=1}^N (E_{si,2n} \cos(n\omega t) + E_{si,2n+1} \sin(n\omega t)), \quad (2.13)$$

$$e_{ri}(t) = E_{ri,1} + \sum_{n=1}^N (E_{ri,2n} \cos(n\omega t) + E_{ri,2n+1} \sin(n\omega t)). \quad (2.14)$$

In PGTs, phase relationships shall be considered in formulating the mesh stiffness and error terms, based on a reference mesh, both for sun-planet and ring-planet meshes. The related phasing equations can be expressed as follows

For sun-planet mesh:

$$k_{si,2n} = k_{s1,2n} \cos(n Z_s \Phi_i), \quad (2.15)$$

$$k_{si,2n+1} = k_{s1,2n+1} \sin(n Z_s \Phi_i). \quad (2.16)$$

$$E_{si,2n} = E_{s1,2n} \cos(n Z_s \Phi_i), \quad (2.17)$$

$$E_{si,2n+1} = E_{s1,2n+1} \sin(n Z_s \Phi_i). \quad (2.18)$$

For ring-planet mesh:

$$k_{ri,2n} = k_{r1,2n} \cos(n Z_r \Phi_i + n \varphi_{sr}), \quad (2.19)$$

$$k_{ri,2n+1} = k_{r1,2n+1} \sin(n Z_r \Phi_i + n \varphi_{sr}). \quad (2.20)$$

$$E_{ri,2n} = E_{r1,2n} \cos(n Z_r \Phi_i + n \varphi_{sr}), \quad (2.21)$$

$$E_{ri,2n+1} = E_{r1,2n+1} \sin(n Z_r \Phi_i + n \varphi_{sr}). \quad (2.22)$$

Here Z_s and Z_r denote the number of teeth for sun and ring gears, respectively. Φ_i is the angular position of the i^{th} planet (i.e. for an equally spaced 4-planet system, planets are positioned at $0, \pi/2, \pi$ and $3\pi/2$, respectively). φ_{sr} is the phase difference between the sun-planet and the ring-planet meshes.

The assumed solutions for Eqs. 2.1 - 2.4 can be expressed in Fourier series as follows

$$x_a(t) = X_{a,1} + \sum_{n=1}^N (X_{a,2n} \cos(n \omega t) + X_{a,2n+1} \sin(n \omega t)) \quad (2.23)$$

Here X_a , where $a = s, r, c, i, i+1, \dots, n_p$, represents the harmonic terms of the displacement of the sun, ring, carrier and planets, respectively.

The resulting nonlinear algebraic equation vector is

$$\mathbf{R} = \left\{ \begin{array}{l} \left(R_{s,1}, \dots, R_{s,2N+1}, R_{r,1}, \dots, R_{r,2N+1}, R_{c,1}, \dots, R_{c,2N+1} \right)^T \\ \left(R_{1,1}, \dots, R_{1,2N+1}, R_{2,1}, \dots, R_{2,2N+1}, \dots, R_{n_p,1}, \dots, R_{n_p,2N+1} \right)^T \end{array} \right\}. \quad (2.24)$$

The equations can be listed for sun gear as

$$R_{s,1} = k_s X_{s,1} + \sum_{i=1}^{n_p} G_{si,0} - F_{s,1} = 0, \quad (2.25)$$

$$R_{s,2n} = k_s X_{s,2n} - n\omega^2 M_s X_{s,2n} + 2n\omega c_{sp} \sum_{i=1}^{n_p} Z_{si,2n+1} + \sum_{i=1}^{n_p} G_{si,2n} - F_{s,2n} = 0, \quad (2.26)$$

$$R_{s,2n+1} = k_s X_{s,2n+1} - n\omega^2 M_s X_{s,2n+1} - 2n\omega c_{sp} \sum_{i=1}^{n_p} Z_{si,2n} + \sum_{i=1}^{n_p} G_{si,2n+1} - F_{s,2n+1} = 0. \quad (2.27)$$

For ring gear:

$$R_{r,1} = k_r X_{r,1} + \sum_{i=1}^{n_p} G_{ri,1} - F_{r,1} = 0, \quad (2.28)$$

$$R_{r,2n} = k_r X_{r,2n} - n\omega^2 M_r X_{r,2n} + 2n\omega c_{rp} \sum_{i=1}^{n_p} Z_{ri,2n+1} + \sum_{i=1}^{n_p} G_{ri,2n} - F_{r,2n} = 0, \quad (2.29)$$

$$R_{r,2n+1} = k_r X_{r,2n+1} - n\omega^2 M_r X_{r,2n+1} - 2n\omega c_{rp} \sum_{i=1}^{n_p} Z_{ri,2n} + \sum_{i=1}^{n_p} G_{ri,2n+1} - F_{r,2n+1} = 0. \quad (2.30)$$

For carrier:

$$R_{c,1} = k_c X_{c,1} - \sum_{i=1}^{n_p} G_{si,1} - \sum_{i=1}^{n_p} G_{ri,1} - F_{c,1} = 0, \quad (2.31)$$

$$R_{c,2n} = k_c X_{c,2n} - n\omega^2 M_c X_{c,2n} - 2n\omega c_{sp} \sum_{i=1}^{n_p} Z_{si,2n+1} - 2n\omega c_{rp} \sum_{i=1}^{n_p} Z_{ri,2n+1} - \sum_{i=1}^{n_p} G_{si,2n} - \sum_{i=1}^{n_p} G_{ri,2n} - F_{c,2n} = 0 \quad , (2.32)$$

$$R_{c,2n+1} = k_c X_{c,2n+1} - n\omega^2 M_c X_{c,2n+1} + 2n\omega c_{sp} \sum_{i=1}^{n_p} Z_{si,2n} + 2n\omega c_{rp} \sum_{i=1}^{n_p} Z_{ri,2n} - \sum_{i=1}^{n_p} G_{si,2n} - \sum_{i=1}^{n_p} G_{ri,2n+1} - F_{c,2n+1} = 0 \quad . (2.33)$$

For planets:

$$R_{i,1} = G_{si,1} - G_{ri,1} = 0 , \quad (2.34)$$

$$R_{i,2n} = -n\omega^2 M_i X_{i,2n} + 2n\omega c_{sp} Z_{si,2n+1} - 2n\omega c_{rp} Z_{ri,2n+1} + G_{si,2n} - G_{ri,2n} = 0 , \quad (2.35)$$

$$R_{i,2n+1} = -n\omega^2 M_i X_{i,2n+1} - 2n\omega c_{sp} Z_{si,2n} + 2n\omega c_{rp} Z_{ri,2n} + G_{si,2n+1} - G_{ri,2n+1} = 0 , \quad (2.36)$$

where $n = 1, 2, \dots, N$, N being the total number of harmonics used in the solution. Z_{si} and Z_{ri} , where $i = 1, 2, \dots, n_p$, denote the harmonic terms of sun-planet and ring-planet mesh displacement functions given in Eqs. 2.7 and 2.8, respectively. Similarly G_{si} and G_{ri} are the harmonic terms of non-linear spring force functions for sun-planet and ring-planet meshes given in Eqs. 2.9 and 2.10, respectively. n stands for the harmonic number and ω represents the mesh frequency.

2.2.1 Newton's Method with Arc-Length Continuation

The nonlinear algebraic equations obtained for PGT model (Eqs. 2-25 – 2.36) can be solved iteratively by utilizing Newton's method, for the unknown displacement vector of:

$$\mathbf{X} = \left\{ \begin{array}{l} \left(X_{s,1}, \dots, X_{s,2N+1}, X_{r,1}, \dots, X_{r,2N+1}, X_{c,1}, \dots, X_{c,2N+1} \right)^T \\ \left(X_{1,1}, \dots, X_{1,2N+1}, X_{2,1}, \dots, X_{2,2N+1}, \dots, X_{n_p,1}, \dots, X_{n_p,2N+1} \right)^T \end{array} \right\}. \quad (2.37)$$

However, during solution, the solution path can reverse its direction which causes Jacobian matrix to become very close to being singular and hence leads to convergence problems. This problem can be avoided by introducing a new continuation parameter, arc-length, instead of the frequency. By using arc-length parameter, it is possible to follow the solution path, even at turning points. Arc-length parameter, s , is defined as the radius of a hypothetical n -dimensional sphere having its center located at the previous converged iteration. To apply arc-length continuation method, the vector of unknowns is expanded as $\mathbf{v} = (\mathbf{X}^T, \omega)^T$. The solution of the new system of nonlinear equations is located on the surface of this n -dimensional sphere, defined by $s^2 = \Delta \mathbf{v}_k^T \times \Delta \mathbf{v}_k$. The additional equations are introduced as

$$h(\mathbf{v}_k) = \Delta \mathbf{v}_k^T \times \Delta \mathbf{v}_k - s^2 = 0, \quad (2.38)$$

$$\Delta \mathbf{v}_k = \mathbf{v}_k - \mathbf{v}_{k-1}. \quad (2.39)$$

Here \mathbf{v}_{k-1} is the converged solution at the previous solution point; whereas, \mathbf{v}_k is the current solution point. Eqn. 2.38 is added to Eqs. 2.25 – 2.36 to obtain a new set of nonlinear algebraic equations for the PGT model, $\mathbf{S}(\mathbf{v}) = (\mathbf{R}(\mathbf{X})^T h(\mathbf{v}))^T$. A single step of Newton iteration is therefore formulated as

$$\mathbf{v}_k^{(m)} = \mathbf{v}_k^{(m-1)} - \mathbf{J}(\mathbf{v}_k^{(m-1)})^{-1} \mathbf{S}(\mathbf{v}_k^{(m-1)}), \quad (2.40)$$

where $\mathbf{J}(\mathbf{v}_k^{(m-1)})$ is the Jacobian matrix of \mathbf{S} calculated at the $(m-1)^{\text{th}}$ iteration for the k^{th} solution point. The iterations continue until the norm of $\mathbf{S}(\mathbf{v}_k^{(m)})$ settles within the given tolerance band.

Further details of Newton's method with arc-length continuation can be found in references [52–54].

2.3 Validation of Multi-Term HBM with Direct Time Integration

Besides its advantages in terms of computational speed, HBM coupled with a path following algorithm such as arc-length continuation is able to show multiple solutions for the speed ranges where nonlinear effects are still dominant. Using time integration method, one can obtain only a single solution depending on the initial conditions. In order to validate HBM solutions, for an example PGT, the solution of the system is obtained by utilizing direct time integration and results are compared with HBM solutions. Parameters of this example gear set are given in Table 2-1.

Table 2-1 Parameters for example planetary gear set used in HBM vs. time integration comparison

	SUN	PLANET	RING
Number of planets	4		
Number of teeth	38	22	82
Module [mm]	4		
Pressure angle [deg]	21.3		
Effective outside diameter [mm]	158	95	323
Root diameter [mm]	142	80	336
Facewidth [mm]	30		
Transverse tooth thickness [mm]	5.3	6.8	5.3
Diameter at measured tooth thickness	152	88	328
Average mesh stiffness [1E6 N/m]	538.0		665.5
Mesh damping coefficients [Ns/m]	1872.7		2078.5
Inertia/r² [kg]	2.42	0.82	10
Torque applied [Nm]	2400	-	-
Young's modulus [GPa]	206.8		

In this example PGT, the ring gear is fixed and carrier is modeled as a large inertia. No TPM is applied on any of the gears. The mesh stiffness for the example PGT is calculated from gear contact mechanics tool WindowsLDP of Ohio State University. 6 harmonic terms are used for representation of time-dependent mesh stiffness functions in HBM solution. Table 2-2 and Table 2-3 give the information related to the mesh stiffness harmonics regarding the example PGT in Table 2-1, for sun-planet and ring-planet meshes, respectively.

Table 2-2 Sun-planet mesh stiffness harmonics

Mesh Stiffness Harmonic #	Amplitude [1E6 N/m]	Phase angle [deg]
1	141.35	-134.41
2	90.94	-57.54
3	16.10	39.22
4	34.58	-131.63
5	37.37	-57.74
6	11.27	13.21

Table 2-3 Ring-planet mesh stiffness harmonics

Mesh Stiffness Harmonic #	Amplitude [1E6 N/m]	Phase angle [deg]
1	174.14	-122.02
2	119.06	-65.34
3	28.77	-6.99
4	34.94	-132.87
5	49.12	-74.32
6	17.06	-25.17

Figure 2-2 and Figure 2-3 show the calculated mesh stiffness functions along with their 6-harmonic approximations.

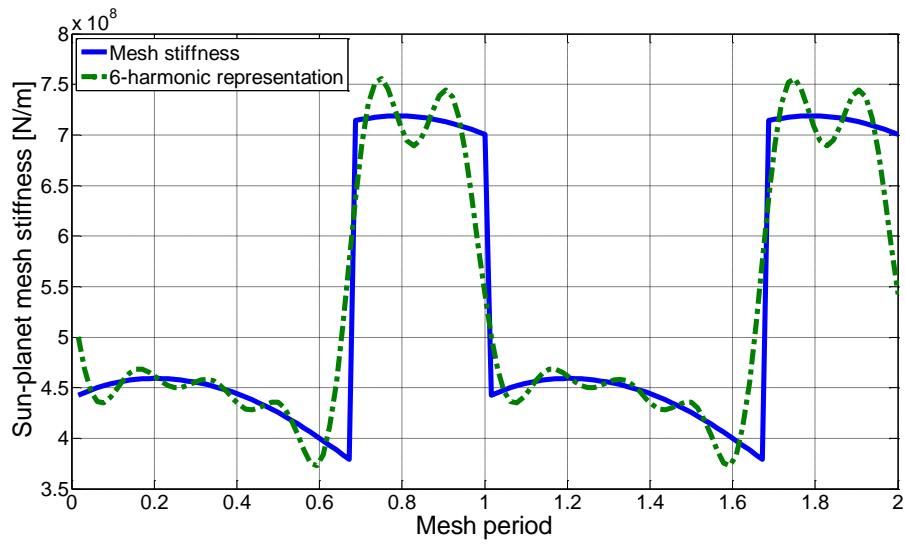


Figure 2-2 Exact sun-planet mesh stiffness and 6-harmonic approximation

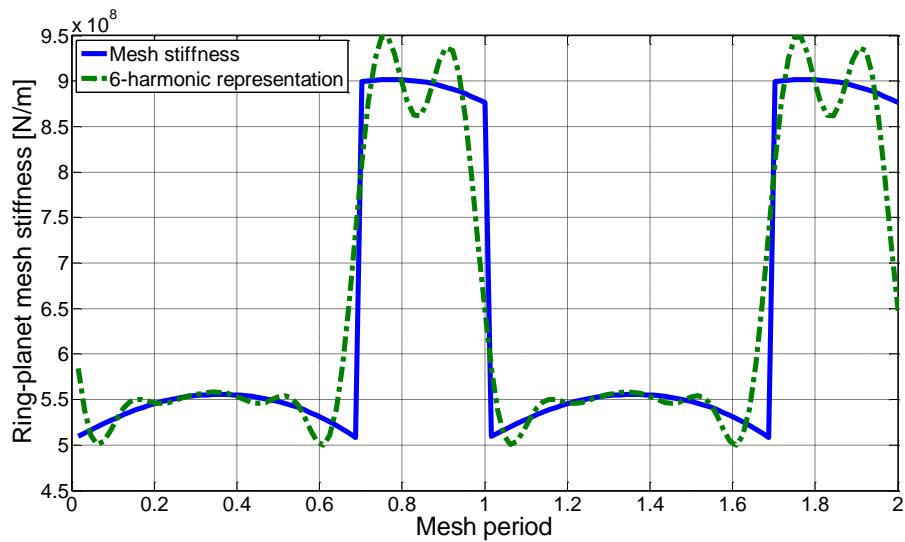


Figure 2-3 Exact ring-planet mesh stiffness and 6-harmonic approximation

Eqs. 2.1 – 2.4 are solved by using direct time integration for the example PGT. Time-integration solution is obtained using the ODE45 routine in MATLAB[®]. For time-integration solution, rms of the response is calculated after the steady state is

reached. Similarly for HBM solution, rms of the harmonic terms of the displacement response is calculated for sun gear and planet gear, respectively, as

$$X_s^{rms} = \left\{ \sum_{n=1}^N \left(\frac{X_{s,2n}^2 + X_{s,2n+1}^2}{2} \right) \right\}^{\frac{1}{2}}, \quad (2.41)$$

$$X_i^{rms} = \left\{ \sum_{n=1}^N \left(\frac{X_{i,2n}^2 + X_{i,2n+1}^2}{2} \right) \right\}^{\frac{1}{2}}, \quad i = 1, 2, \dots, n_p. \quad (2.42)$$

Comparisons between results obtained using direct time-integration and HBM solution using 6 harmonics are shown in Figure 2-4 and Figure 2-5 for sun displacement and planet displacement, respectively.

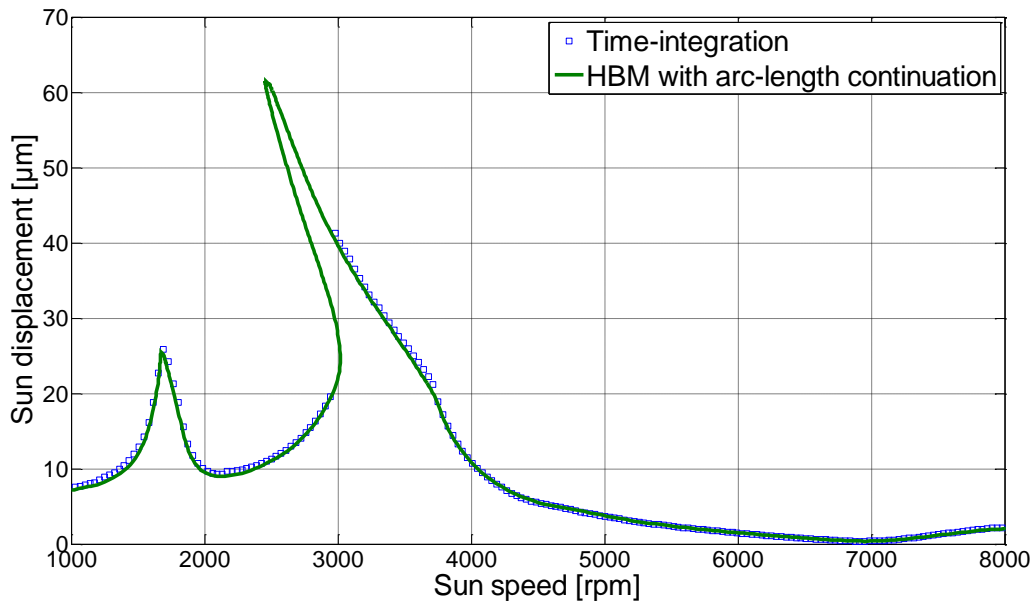


Figure 2-4 TI vs HBM comparison for sun displacement (rms)

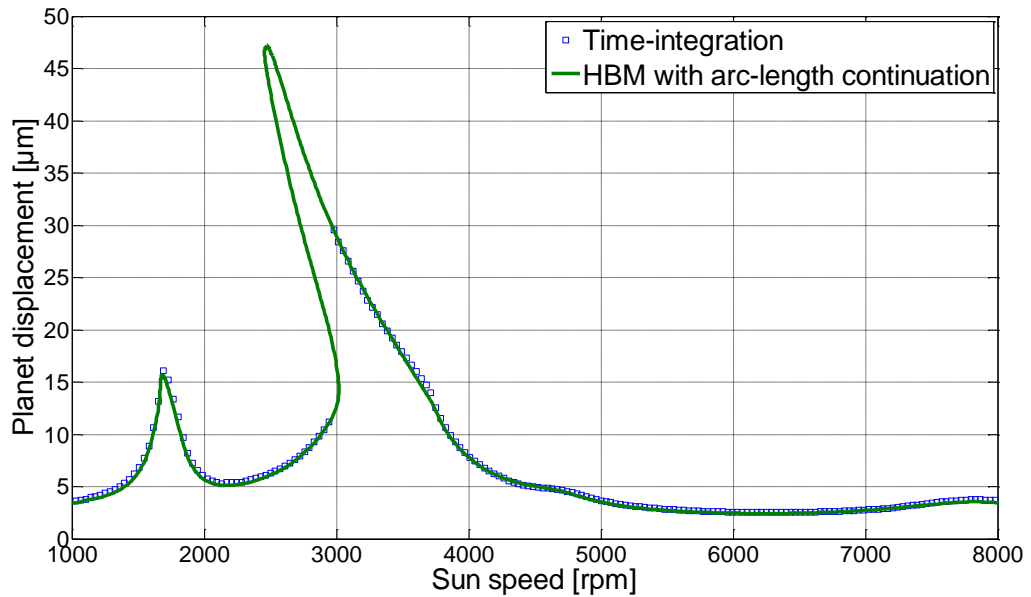


Figure 2-5 TI vs HBM comparison for planet displacement (rms)

Results of the comparison study show that HBM with 6 harmonics captures the steady state response of the PGT system under consideration accurately. Multiple solutions are obtained with HBM at the resonant frequency around 3000 rpm which are not determined by TI. In the rest of the study, HBM is used to determine the steady state response of gear trains.

2.4 Modal characteristics of PGTs

PGTs show unique characteristics in terms of modal properties. Modal analysis is performed for the example PGT provided in Table 2-1, except that this time the carrier has a finite equivalent inertia of 10kg, in order to clearly understand and draw conclusions regarding the characteristics of torsional modes.

Modal analyses are performed for the different cases where sun, ring and carrier are fixed in each case.

Table 2-4 shows the natural frequencies for these different cases.

Table 2-4 Natural frequencies of the example PGT for different boundary conditions

Mode number	Natural frequency in Hz (Ring-fixed)	Natural frequency in Hz (Sun-fixed)	Natural frequency in Hz (Carrier-fixed)
1	0	0	0
2	4559	3775	3709
3	6099	6099	6099
4	6099	6099	6099
5	6099	6099	6099
6	7146	6469	7256

Table 2-5, Table 2-6 and Table 2-7 show the mass-normalized mode shapes for the configurations in Table 2-4. The first mode for each configuration is the rigid-body mode where the relative sun-planet and ring-planet mesh displacements are zero. Modes 3-5 are pinion modes in which neither of sun, carrier or ring gears rotate. Natural frequencies for these modes are also observed to be independent of the number of planets. Moreover sum of rotations for the planets equal to zero in these modes. These modes are called as “sequentially-phased” modes. The mode shapes for the second and 6th modes are such that all planets rotate equally. These modes are categorized as “in-phase” modes. The details of the terms “in-phase” and “sequentially-phased” will be given in Chapter 3.

Table 2-5 Mass-normalized modal vectors for fixed sun gear configuration

Fixed sun						
Mode number	1	2	3	4	5	6
Carrier	-0,137	-0,281	0	0	0	-0,047
Ring	-0,274	0,116	0	0	0	0,108
Planet-1	-0,137	0,153	-0,169	0,831	0,442	-0,513
Planet-2	-0,137	0,153	0,904	-0,268	0,160	-0,513
Planet-3	-0,137	0,153	-0,140	0,105	-0,940	-0,513
Planet-4	-0,137	0,153	-0,595	-0,668	0,338	-0,513

Table 2-6 Mass-normalized modal vectors for fixed ring gear configuration

Fixed ring						
Mode number	1	2	3	4	5	6
Carrier	0,209	-0,281	0	0	0	-0,047
Sun	0,417	0,309	0	0	0	-0,379
Planet-1	-0,209	-0,258	0,189	0,863	0,366	-0,441
Planet-2	-0,209	-0,258	0,644	-0,630	0,320	-0,441
Planet-3	-0,209	-0,258	-0,876	-0,275	0,269	-0,441
Planet-4	-0,209	-0,258	0,042	0,042	-0,954	-0,441

Table 2-7 Mass-normalized modal vectors for fixed carrier configuration

Fixed carrier						
Mode number	1	2	3	4	5	6
Ring	-0,252	0,178	0	0	0	-0,067
Sun	0,252	0,484	0	0	0	0,339
Planet-1	-0,252	-0,187	-0,411	0,776	-0,378	0,454
Planet-2	-0,252	-0,187	0,935	0,005	-0,200	0,454
Planet-3	-0,252	-0,187	-0,401	-0,785	-0,370	0,454
Planet-4	-0,252	-0,187	-0,123	0,004	0,948	0,454

Table 2-5, Table 2-6 and Table 2-7 show that the characteristics mentioned here are independent of which member of the PGT is fixed, i.e. similar modal characteristics are observed for different PGTs irrespective of the power configuration. Figure 2-6 shows mode shapes for the fixed-ring configuration given in Table 2-6. Note that carrier is not shown in this figure for clarity.

The modal characteristics of PGTs are important for the forced response dynamic analyses. It is possible to suppress some of these natural modes through proper configuration of mesh phasing. The details of mesh phasing for PGTs are provided in the next chapter. Moreover these mode shapes also affect the design of TPMs which are applied in order to reduce vibration of PGTs. The effect of mode shapes on the design of ideal TPMs are addressed in Chapter 6.

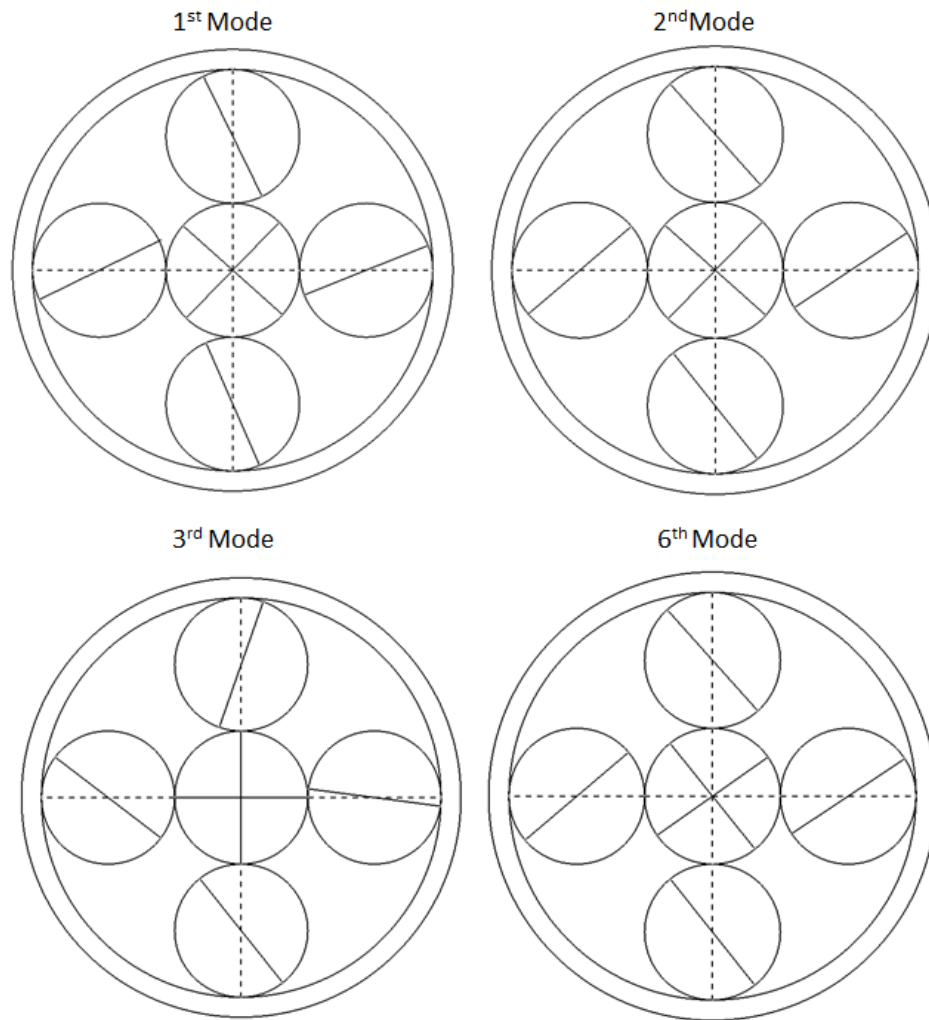


Figure 2-6 Mode shapes for fixed-ring configuration

CHAPTER 3

BASIC CONCEPTS IN PLANETARY GEAR DYNAMICS

3.1 Mesh Phasing in Planetary Gear Trains

Phase differences between gear mesh actions for planet-sun and planet-ring gear meshes are important in characterizing the dynamic properties of a PGT. In order to reduce the vibration in planetary gears, one of the most effective remedies is the proper phasing of the contact between different teeth of a planetary gear system. By doing so, it is possible to cancel out some of the harmonics of the gear mesh forces.

Since it is one of the key elements affecting the characteristics of PGT dynamics, additional care should be taken when defining the phase relationships between the multiple tooth pairs that continuously come into contact with each other. These phase relationships have great influence on the dynamic response of planetary gear sets.

There exists a difference in the phase for mesh stiffness functions between gear pairs in a PGT. The mesh phasing difference between individual sun-planet and ring-planet meshes depend on the number of teeth of sun and ring gears and the position of the planets. Therefore number of planets in a PGT also indirectly affects the mesh phasing characteristics.

In order to also show the effect of contact ratio on the mesh stiffness, consider a rectangular wave approximation for mesh stiffness functions of both sun-planet and ring-planet pairs. The stiffness functions for different sun-planet and ring-planet pairs can be defined as [7]:

For sun gear:

$$k_{si}(t) = k_{si,1} + \sum_{n=1}^N (k_{si,2n} \cos(n \omega t) + k_{si,2n+1} \sin(n \omega t)) \quad (3.1)$$

$$k_{si,2n} = k_{si,1} \frac{2}{n\pi C_{sp}} \sin(n\pi(C_{sp} - \bar{C})) \cos(nZ_s \phi_i) \quad (3.2)$$

$$k_{si,2n+1} = k_{si,1} \frac{-2}{n\pi C_{sp}} \sin(n\pi(C_{sp} - \bar{C})) \sin(nZ_s \phi_i) \quad (3.3)$$

For ring gear:

$$k_{ri}(t) = k_{ri,1} + \sum_{n=1}^N (k_{ri,2n} \cos(n \omega t) + k_{ri,2n+1} \sin(n \omega t)) \quad (3.4)$$

$$k_{ri,2n} = k_{ri,1} \frac{2}{n\pi C_{rp}} \sin(n\pi(C_{rp} - \bar{C})) \cos(nZ_r \phi_i + n \gamma_{sr}) \quad (3.5)$$

$$k_{ri,2n+1} = k_{ri,1} \frac{-2}{n\pi C_{rp}} \sin(n\pi(C_{rp} - \bar{C})) \sin(nZ_r \phi_i + n \gamma_{sr}) \quad (3.6)$$

In these equations, C_{sp} and C_{rp} are contact ratios between sun-planet and ring-planet gear meshes respectively. \bar{C} denotes the minimum number of tooth pairs in contact during a mesh cycle, which can be defined as the periodic amount of gear rotation after which the next tooth arrives at the position of the present tooth which is in contact with its mating tooth. ϕ_i is the angular position of the planet i . Z_s and Z_r are the number of teeth for sun and ring gears, respectively. n stands for the harmonic number and γ_{sr} is the phase difference between sun-planet and ring-planet meshes.

The mesh phasing relationships between individual sun-planet and ring-planet pairs can be classified under 2 categories. When the meshing action between individual sun-planet or ring-planet pairs occur simultaneously, the gear meshes are “in-phase”. For “sequentially-phased” meshes, adjacent sun-planet or ring-planet meshing actions are out-of-phase. A special case for sequentially-phased meshes is “counter-phased” meshes where the phase difference between adjacent meshes is π , i.e. diametrically-opposed planets are at the same phase and the phase difference with the other mesh pair is half of the mesh cycle. This is a possible configuration for PGTs with number of planets equal to 4.

Figure 3-1 shows example sun-planet mesh stiffness plots for such mesh-phasing configurations for a PGT with 4 planets.

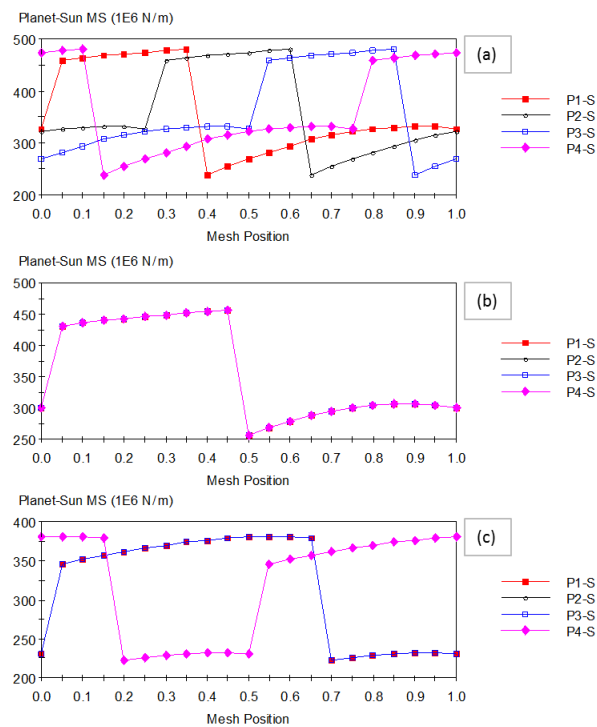


Figure 3-1 Example sun-planet mesh stiffness plots for a) sequentially-phased, b) in-phase, c) counter-phased mesh configurations. Note that in b), all stiffness curves overlap with each other while in c), P1-S overlaps with P3-S and P2-S overlaps with P4-S

For a PGT having equally-spaced planets, the i^{th} harmonic of parametric stiffness excitation for individual sun-planet gear pairs will be in phase if iZ_s/n is integer and sequentially phased if iZ_r/n is not an integer [55]. The same is also valid for ring-planet meshes.

Table 3-1 lists different configurations for mesh-phasing based on the number of gear teeth. Dynamic simulations are performed for these configurations of the example PGT given in Table 2-1.

Table 3-1 Different mesh-phasing configurations for the example PGT in Table 2-1

Configuration number	Mesh-phasing configuration	Z_s	Z_r	Z_p
1	Sequentially-phased (counter-phased)	38	82	18
2	In-phase	36	80	18
3	Sequentially-phased	35	81	18

Figure 3-2 and Figure 3-3 show an initial comparison of sun-planet and ring-planet displacements for the configurations listed in Table 3-1. For this comparison, the performed analyses are limited to linear solutions; in order clearly address the resonance regions with the harmonics of the parametric excitations of respective configurations. All damping ratios for the performed simulations are equal to 0.035. Damping ratio definitions are provided in section 3.2.2. It is clearly apparent from both Figure 3-2 and Figure 3-3 that dynamic responses of PGTs are strongly dependent on their mesh phasing characteristics.

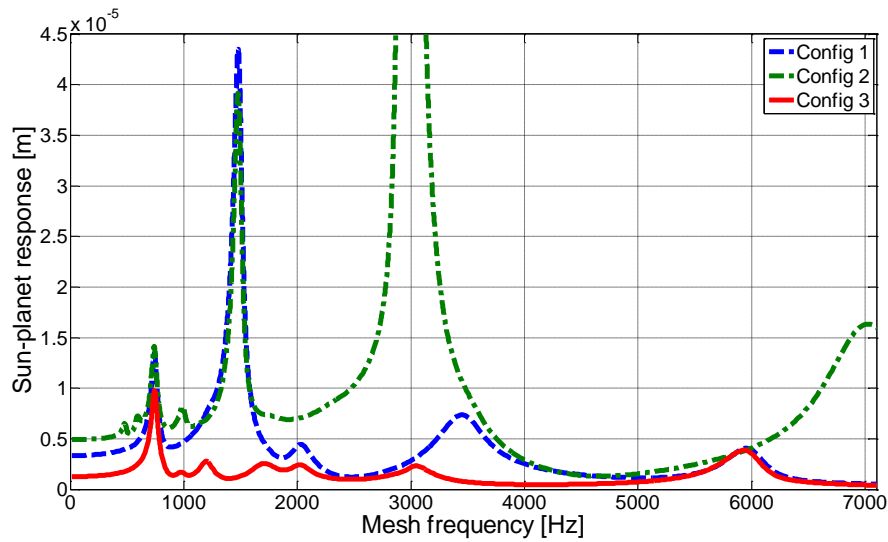


Figure 3-2 Sun-planet mesh displacement (rms) for different mesh phasing configurations given in Table 3-1

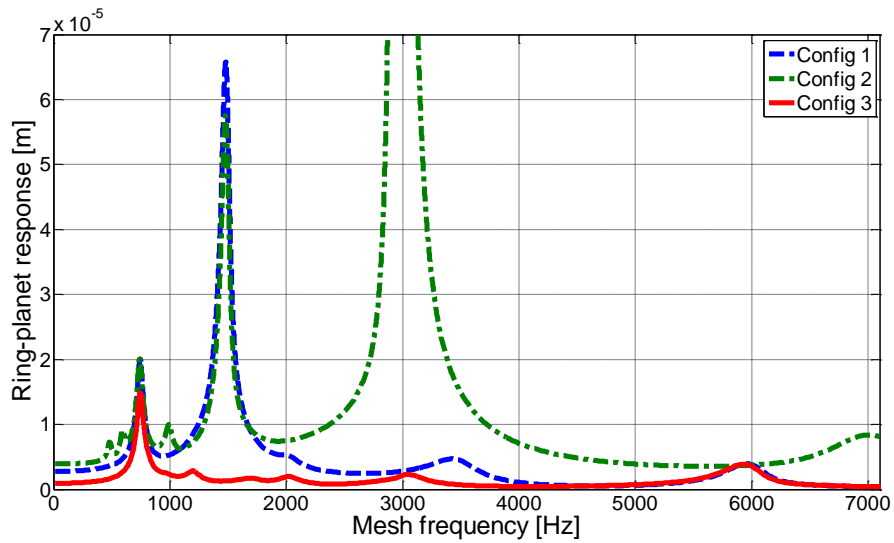


Figure 3-3 Ring-planet mesh displacement (rms) for different mesh phasing configurations given in Table 3-1

The first observation is that “sequentially-phased” PGT configurations are much quieter than their “in-phase” counterparts. The excitations tend to cancel each other for equally spaced planets. Table 3-2 provides information regarding the natural

frequencies of the PGT, parameters of which are given in Table 2-1. Information regarding the harmonics of the mesh stiffness for this PGT is already provided in Table 2-5 and Table 2-6.

Table 3-2 Natural frequencies for the example PGT in Table 2-1

Mode number (n)	1	2	3	4	5	6
Natural frequency, ω [Hz]	0	2994	6033	6033	6033	7038

Another important outcome of the comparison study is that the excited natural modes depend on the phasing configuration. “In-phase” modes are only excited by “in-phase” harmonics of excitation, whereas the same also holds for the “sequentially-phased” modes. This also results in the fact that, for “in-phase” PGT configurations, “sequentially-phased” modes never get excited. For the example PGT under consideration, in configuration 1, excitation of the first in-phase mode was possible through the parametric excitation of the second and the 4th harmonics of the mesh stiffness. Moreover the second in-phase mode is also excited by the second harmonic of the mesh stiffness for this configuration. For the second configuration, all 6 harmonics of the mesh stiffness excitations excited the first in-phase mode. The second in-phase mode is also excited by the first harmonic of the mesh stiffness functions. For the 3rd configuration, although the responses are relatively lower, the 4th harmonic of the mesh stiffness excitation excited the first in-phase mode. The sequentially-phased modes are excited by the first 3 harmonics and the 5th harmonic of the mesh stiffness excitation. The excited dynamic modes for this configuration can be clearly identified in Figure 3-4, using the natural frequency information provided in Table 3-2.

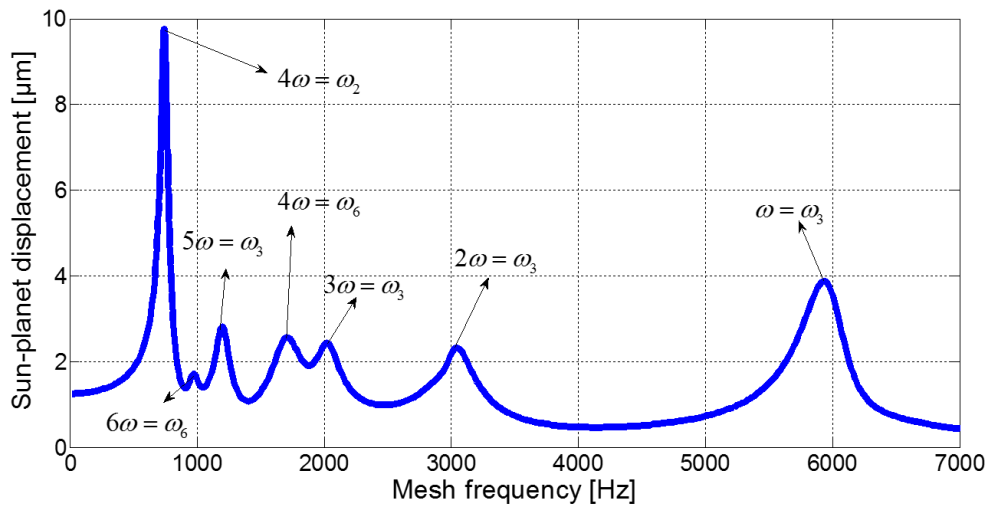


Figure 3-4 Sun-planet mesh displacement for 3rd configuration, excited modes and excitation sources

The amplitudes of the sequentially-phased modes are also observed to be much lower than the amplitudes of the in-phase modes. Especially, response amplitudes at the first in-phase mode are significantly higher compared to the amplitudes at other modes. However, this observation may not be valid for the TPM applied PGTs. This subject is going to be investigated in detail in Chapter 6. Although the response of sequentially-phased modes are not as high as those for “in-phase” modes, the dynamic effects can still be considered as significant and therefore, additional means for improvement, such as application of TPMs, may be required. Dynamic loading factors, which can be simply defined as the ratio of dynamic load to the static load at a single gear mesh, may still be high enough to reduce the fatigue lives of PGTs for sequentially-phased modes.

Mesh phase differences are inevitably dependent on the number of planets for equally-spaced PGTs. It is possible to use equally spaced planets in the first configuration, i.e. sequentially-phased, given in Table 3-1. Dynamic responses obtained for PTGs with 3, 4 and 5 planets are given in Figure 3-5 and Figure 3-6.

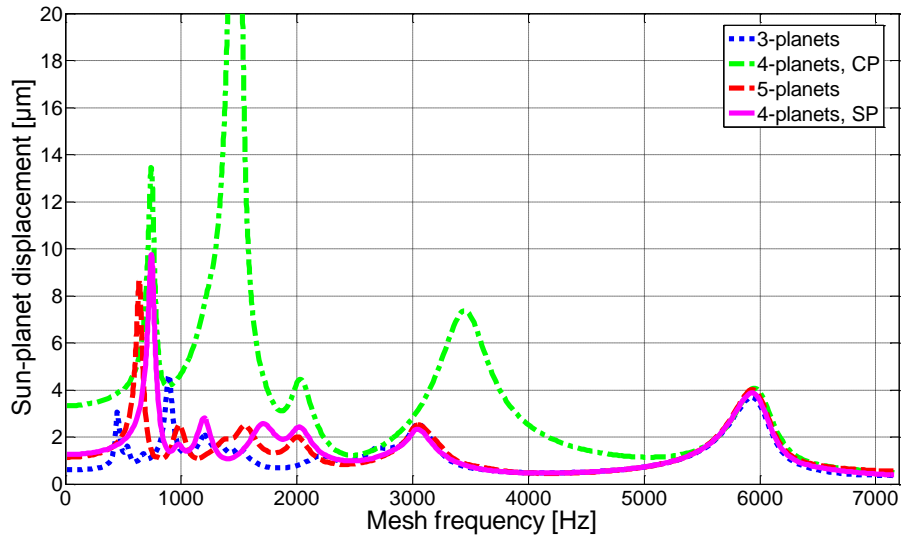


Figure 3-5 Sun-planet displacements (rms) for PGTs with different number of planets with Sequentially-phased (SP) and Counter-phased (CP) configurations

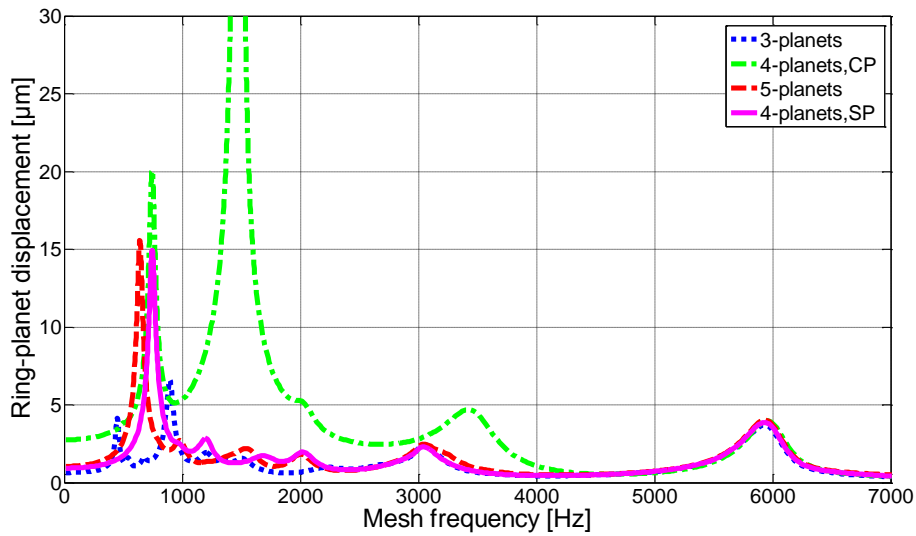


Figure 3-6 Ring-planet displacements (rms) for PGTs with different number of planets with Sequentially-phased (SP) and Counter-phased (CP) configurations

For this comparison, static mesh loads between all meshes are kept constant in all cases, irrespective of the number of planets, by adjusting the external torque applied on the sun-gear, which is equal to 2400Nm for the example PGT with 4 planets. The excitation of in-phase mode by the 3rd harmonic of the 4-planet configuration resulted in the highest vibration. This figure suggests that it is good practice to avoid in-phase modes in the first harmonics of mesh stiffness excitation. Since mesh stiffness variation shows similar frequency decomposition characteristics with a rectangular wave, the excitation will be lower for higher harmonics of the mesh stiffness variation. Another interesting outcome of these simulations is that the 3-planet configuration, which has a phase-difference of $2\pi/3$ between respective sun-planet and ring-planet gear meshes, resulted in the most favorable dynamic response. Moreover, it is also clearly seen that the natural frequencies for the sequentially-phased modes are independent of the number of planets; however, the natural frequencies for the in-phase modes slightly change depending on the number of planets.

Based on the mentioned effects of different mesh phasing scenarios on the dynamics of PGT, the design of a PGT should consider achieving favorable mesh-phasing configurations in order to reduce the dynamic effects, provided an operational spectrum defining the expected speed intervals. It is possible to eliminate some of the resonances within the operational speed range by the selection of proper mesh-phasing arrangements. Harmonics of mesh stiffness have to be considered when performing such a study which aims to optimize the dynamic characteristics of a PGT. For a wide range of operational speed, one can also consider to give priority to the elimination of in-phase modes, as these modes show the highest dynamic response amplitudes.

3.2 Effects of PGT Model Parameters on PGT Dynamics

Aside from mesh-phasing, PGT dynamics are also dependent on many design parameters. In this chapter, effects of backlash, damping ratio, external force and contact ratio on PGT dynamics are investigated. The effect of ring gear thickness is analyzed in Chapter 4. Chapter 6 is dedicated to a detailed discussion of the effects of TPMs on PGT dynamics.

3.2.1 Backlash

Backlash is simply defined as the clearance between the mating gear teeth. The main purpose of backlash is to allow for a film of lubricating oil to form such that tooth damage due to overheating is avoided. Moreover, in practice, backlash is also necessary for installation of the gears. On the contrary side, backlash has negative effects for the positioning equipment such as those used in robots etc. due to the loss in accuracy.

In gear dynamics, backlash is the primary source for nonlinearity. Effect of backlash on spur gears can be found in several references [56,57]. The example PGT given in Table 2-1 is considered here for investigating the effect of backlash amount. Note that the “in-phase” configuration ($Z_s = 36$, $Z_r = 80$) of this example PGT is used in order to make a clear demonstration of the effect of backlash, due to the fact that higher dynamic responses are observed for in-phase configuration relative to the sequentially-phased PGTs. All parameters other than the amount of backlash are kept the same for all simulations. Results obtained for sun displacement and planet displacement are given in Figure 3-7 and Figure 3-8, respectively. All damping ratios are equal to 0.08 in these simulations.

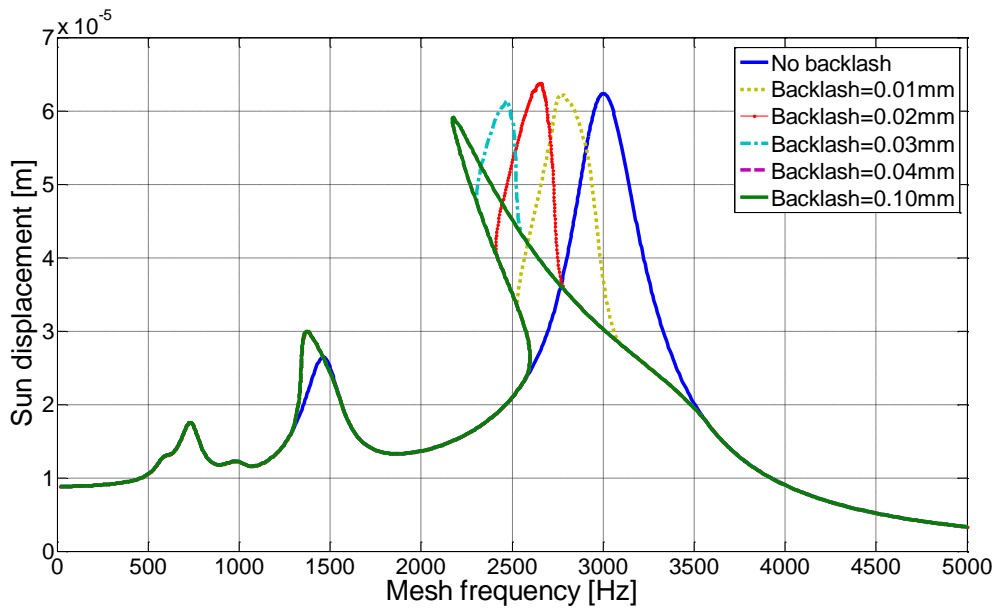


Figure 3-7 Sun displacement (rms) response with different amount of backlash

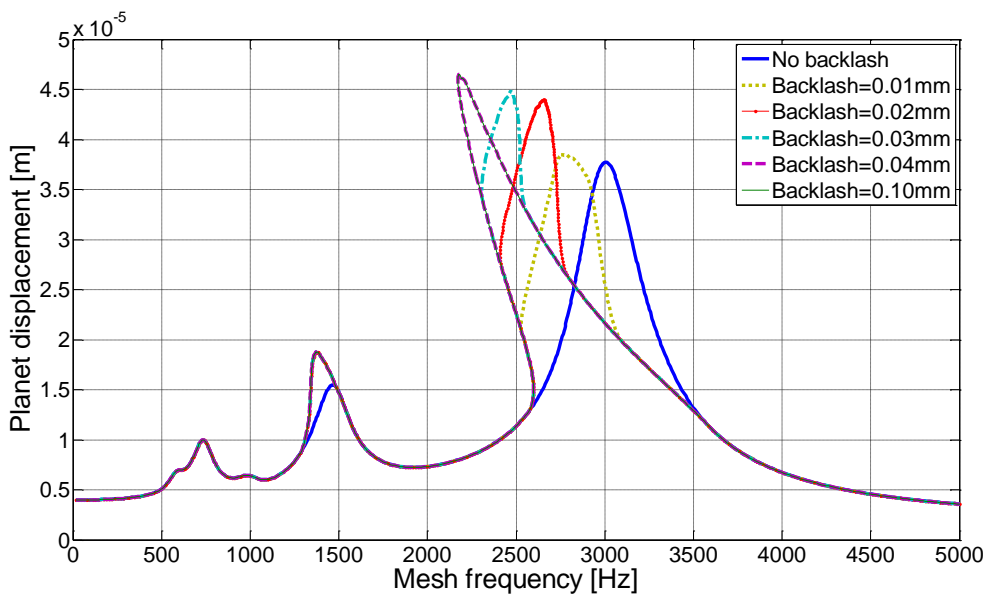


Figure 3-8 Planet displacement (rms) response with different amount of backlash

A softening-type nonlinearity is observed for the example PGT due to backlash. A shift of resonance frequency to the lower frequencies occurs. This shows that, similar to parallel-axis spur gears, modeling of nonlinearity is critical for the forced-

response analysis of PGTs with spur gears. It should also be noted that the occurrence of the nonlinear resonances are also possible at the speed intervals where a natural mode is excited by a higher harmonic of mesh stiffness excitation. For Figure 3-7 and Figure 3-8, this phenomenon is observed for the second harmonic of the mesh stiffness, i.e. at $\omega \approx 1500\text{Hz}$ where $2\omega = \omega_2$ (the first in-phase natural frequency of the system). Around resonance frequencies, multiple solutions are observed. It is also apparent from Figure 3-7 and Figure 3-8 that, for smaller backlash (i.e. backlash values less than 0.04mm), double-sided contact occurs for the mating gear teeth. The double-sided contact cannot be observed beyond a certain value of backlash. Accordingly, the responses shown in Figure 3-7 and Figure 3-8 for backlash values greater or equal to 0.04mm, are the same. Therefore, for dynamic analyses, one can avoid to model the double-sided contact phenomenon provided that the estimated response amplitudes are lower than the amount of backlash.

Figure 3-9 and Figure 3-10 show the dynamic elastic mesh forces between sun-planet and ring-planet pairs.

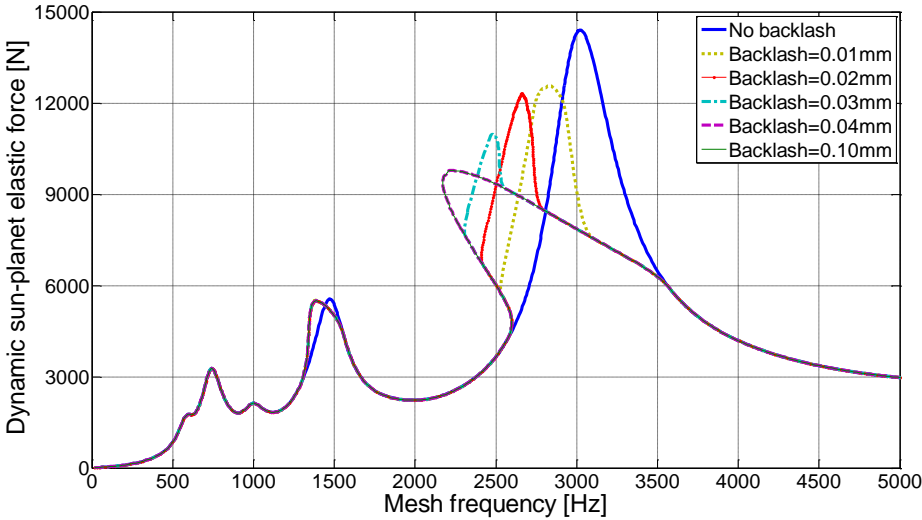


Figure 3-9 Dynamic sun-planet elastic force (rms) for different amount of backlash

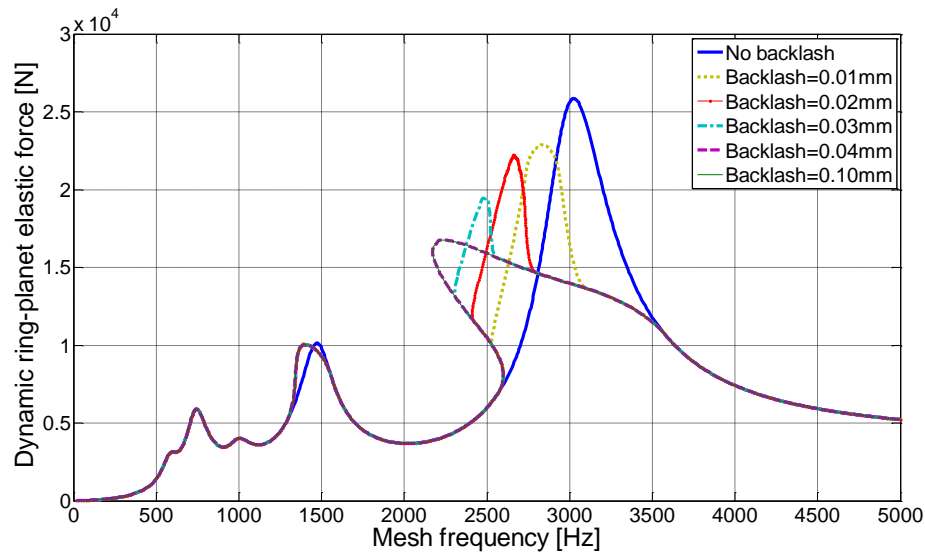


Figure 3-10 Dynamic ring-planet elastic force (rms) for different amount of backlash

The maximum dynamic force increases with decreasing amount of backlash, while the frequencies at which maximum dynamic force is obtained shift to higher speeds. Therefore, it is a better design practice to have sufficient backlash which would prevent having double-sided contact, especially, for the cases where the operational speed range covers resonance frequencies.

Here, it should also be underlined that the effect of external force also plays a role regarding the effect of backlash, i.e. double-sided contact condition is also dependent on the external force along with the amount of backlash. For higher external forces, double-sided contact can occur for a given amount of backlash.

Next, following case is investigated: The amount of backlash for either one of sun-planet or ring-planet pairs is such that double-sided contact occurs for one of the pairs; whereas, for the other pairs, only loss of contact is observed. In order to simulate such a condition, for the “in-phase” configuration ($Z_s = 36$, $Z_r = 80$) of the example PGT given in Table 2-1, backlash amount of sun-planet pairs is kept

constant at 1mm, which is large enough to avoid a double-sided contact, whereas the backlash of the ring-planet pairs is 0.01mm. The dynamic response in terms of rms of the sun displacement is given in Figure 3-11, for the resonance region around 2800Hz. Note that all damping ratios are taken as 0.06 in this simulation.

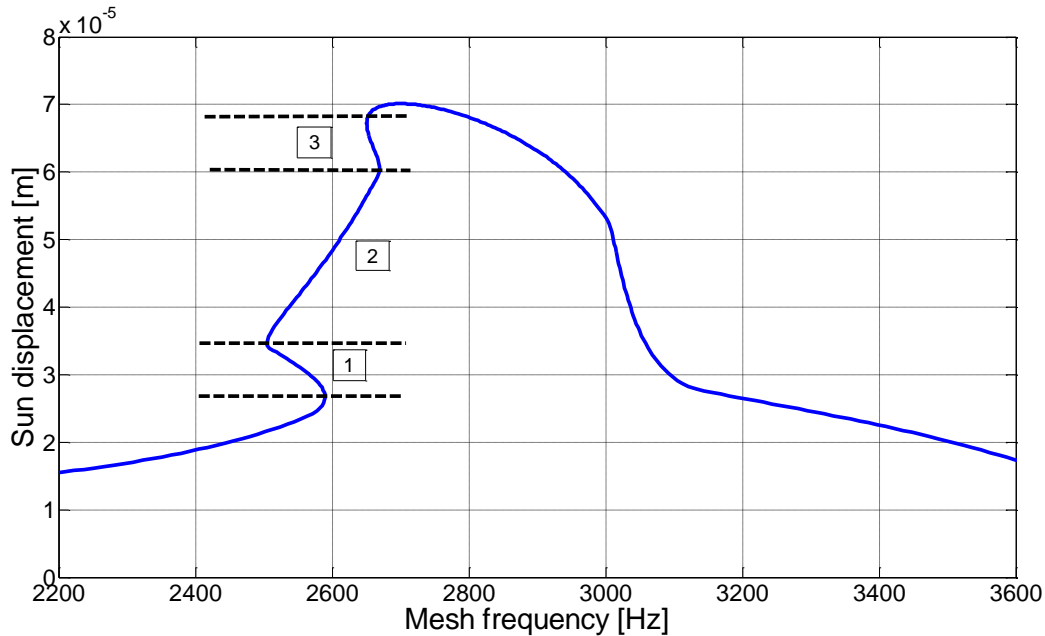


Figure 3-11 Sun displacement (rms) for $b=0.5\text{mm}$ for sun-planet and $b=0.005\text{mm}$ for ring-planet pairs, respectively. Region 1: No-impact for sun-planet, single-sided impact for ring-planet, Region 2: No-impact for sun-planet, double-sided impact for ring-planet, Region 3: Single-sided impact for sun-planet, double-sided impact for ring-planet pairs.

Figure 3-11 shows the different contact conditions near the resonance region. Although no double-sided contact occurs for sun-planet pairs, the sun-planet dynamics are also affected from the double-sided contact occurring at ring-planet meshes. Figure 3-12 gives dynamic sun-planet and ring-planet mesh forces for the example frequencies which fall into different regions depicted in Figure 3-11. From the time histories of the dynamic mesh forces, which are given for duration of a single mesh cycle, the contact conditions stated in Figure 3-11 are clearly identified.

Note that a dynamic force which is equal to 0 denotes no-contact condition, whereas a negative value indicates a back-side contact.

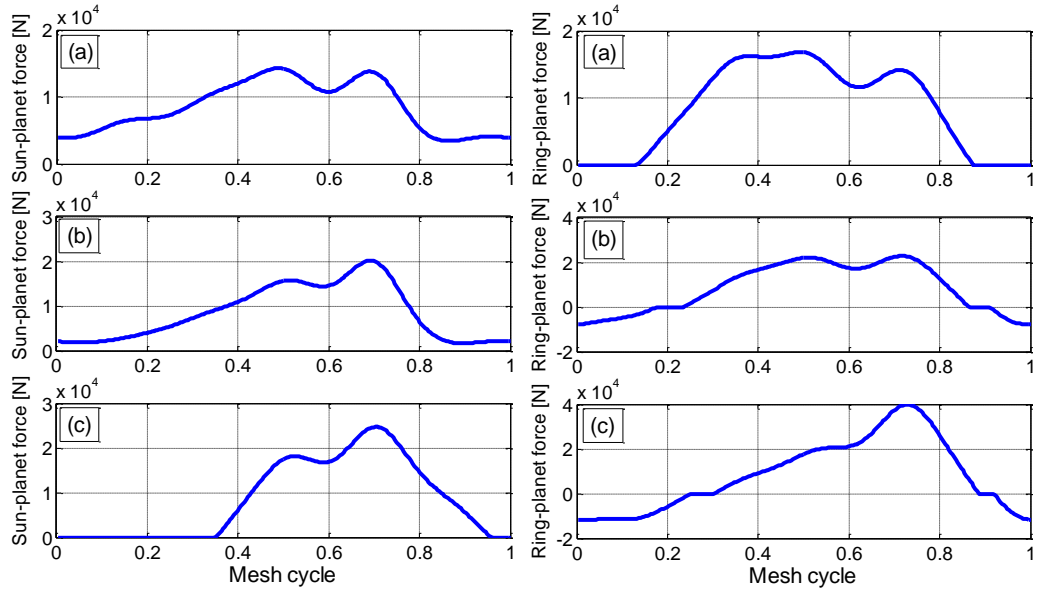


Figure 3-12 Time histories for sun-planet and ring-planet mesh forces, a) $\omega=2553\text{Hz}$, Region 1, b) $\omega=2600\text{Hz}$, Region 2, c) $\omega=2660\text{Hz}$, Region 3.

Another interesting case, which can be considered as a limit condition to the previous one, is that either one of sun-planet or ring-planet pairs have no backlash, whereas the other pairs have different amounts of backlash.

In such an example, for the “in-phase” configuration ($Z_s = 36$, $Z_r = 80$) of the example PGT considered, two different backlash conditions for the ring-planet pairs are compared; whereas, no backlash is defined for sun-planet. The backlash values of the ring-planet pairs used for the response comparison are 0.1mm and 0.03mm, respectively. Figure 3-13 shows the sun displacement response (rms) for the mentioned parameter sets.

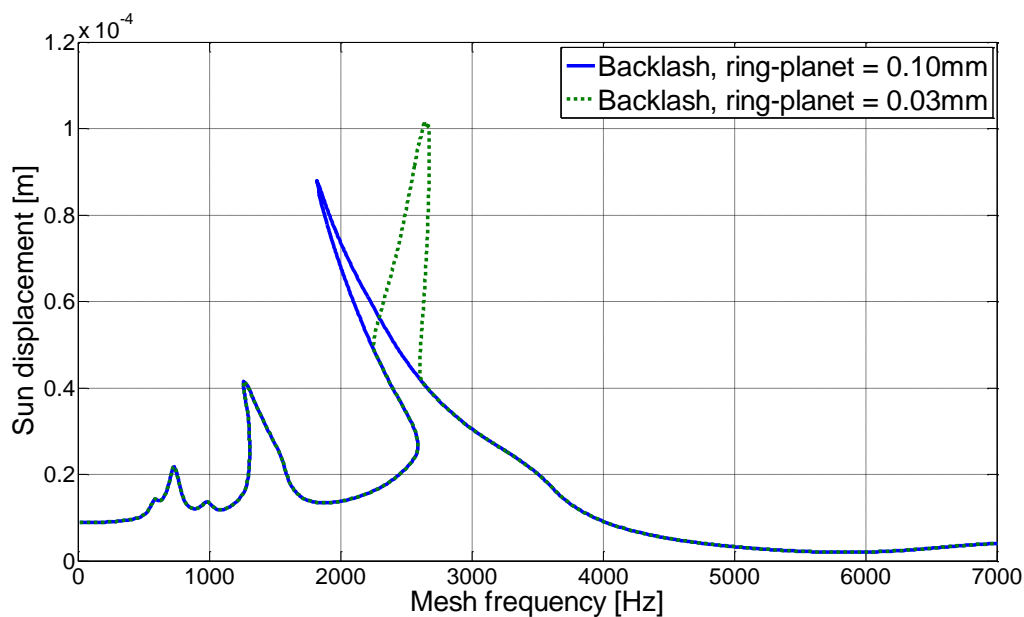


Figure 3-13 Sun displacement (rms) response with different amount of backlash for ring-planet pair – no backlash for sun-planet

It is observed that although the sun-planet mesh does not include any backlash, the effect of both loss of contact and double sided contact situations are also observed on the sun gear response.

3.2.2 Damping

Damping in geared systems is usually achieved by the lubrication. The amount of lubricating oil used is tried to be optimized in order to achieve a sufficient cooling of the geared systems which at the same time will not result in an excessive loss of power.

Since gearbox lubrication is the main source of damping in geared systems, in most of the gear dynamic studies, damping is modeled as viscous damping and usually defined by a constant viscous damping coefficient. Although the exact amount of

damping is hard to measure and depends on many parameters such as the oil type, operating temperature etc., it is a usual practice to apply damping ratios ranging from 0.01 to 0.1 depending on the gearbox under consideration in gear dynamics studies.

Damping ratios can be formulated in PGTs as follows

$$\begin{aligned} \xi_s &= \frac{c_{sp}}{2\omega_s M_s}, \xi_r = \frac{c_{rp}}{2\omega_r M_r}, \xi_{sc} = \frac{c_{sp}}{2\omega_{sc} M_c}, \\ \xi_{rc} &= \frac{c_{rp}}{2\omega_{rc} M_c}, \xi_{sp} = \frac{c_{sp}}{2\omega_{sp} M_p}, \xi_{rp} = \frac{c_{rp}}{2\omega_{rp} M_p} \end{aligned} \quad (3.7)$$

where

$$\begin{aligned} \omega_s &= \sqrt{\frac{k_{si}}{M_s}}, \quad \omega_r = \sqrt{\frac{k_{ri}}{M_r}}, \quad \omega_{sc} = \sqrt{\frac{k_{si}}{M_c}} \\ \omega_{rc} &= \sqrt{\frac{k_{ri}}{M_c}}, \quad \omega_{sp} = \sqrt{\frac{k_{si}}{M_p}}, \quad \omega_{rp} = \sqrt{\frac{k_{ri}}{M_p}} \end{aligned} \quad (3.8)$$

The example PGT given in Table 2-1 is used for investigating the effect of damping on the dynamic response. Note that the “in-phase” configuration ($Z_s = 36$, $Z_r = 80$) of this example PGT is used in order to make a clear demonstration of the effect of damping, due to the fact that higher dynamic effects are observed for in-phase configuration relative to the sequentially-phased PGTs. Figure 3-14 and Figure 3-15 show the dynamic response of the example PGT with different damping coefficients. Figure 3-14 and Figure 3-15 give rms sun displacement and rms sun-planet dynamic mesh force. In these simulations, all damping coefficients outlined in Equation 3.7 are equal to the given value of damping. Backlash values for both sun-planet and

ring-planet pairs are equal to 1.0mm. Other parameters besides damping are kept the same for simulations.

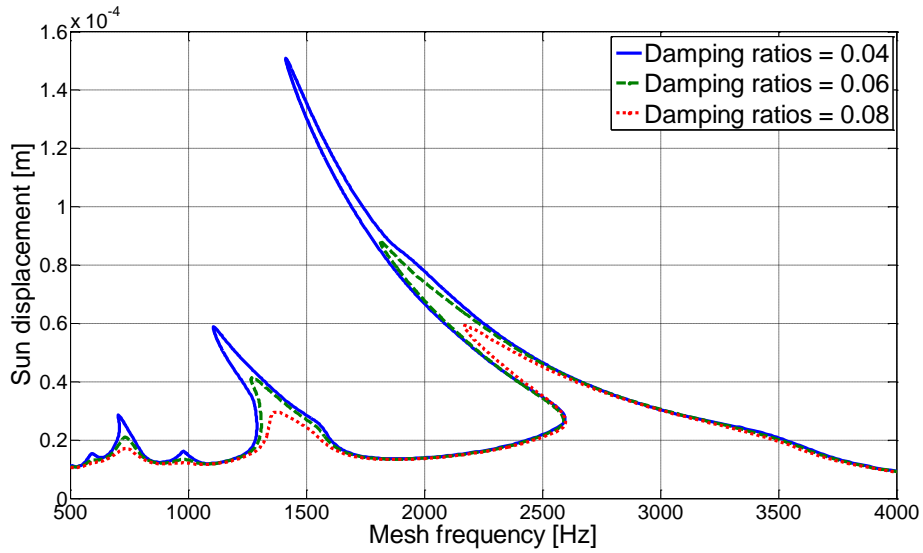


Figure 3-14 Dynamic sun displacement (rms) for different damping ratios

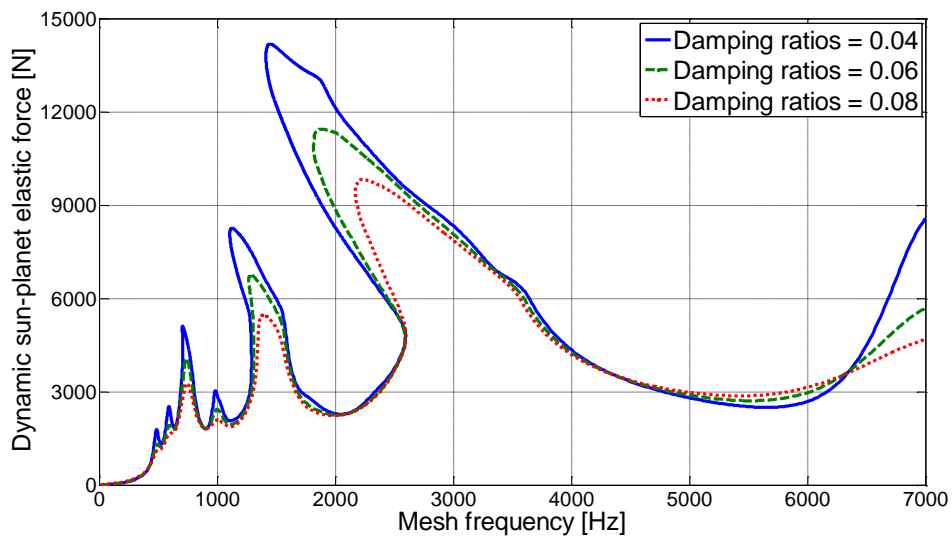


Figure 3-15 Dynamic elastic sun-planet force (rms) for different damping ratios

It is clear that damping not only reduces the dynamic response but also reduces the effect of nonlinearity, which is an expected result. The magnitude of the response is reduced and the resonant frequency shifts towards to linear resonant frequency as the damping ratio increases.

3.2.3 Contact ratio

Gear contact ratio is defined as the average number of gear tooth pairs in contact during a mesh cycle. It is a key parameter of gear design which also plays an important role in gear dynamics. In practice, most of the spur gears have contact ratios between 1 and 2, as higher contact ratios are often difficult to obtain considering limitations from other aspects of gear design. A higher contact ratio is known to be advantageous in terms of load sharing and static torque capacity. Besides these advantages, gear dynamics are also positively influenced for higher contact ratios, especially when the contact ratio is close to an integer value. As contact ratio gets closer to an integer value, the variation of mesh stiffness decreases; therefore, spur gears having contact ratios closer to 2 usually show more favorable dynamic characteristics.

To check the validity of these characteristics for PGTs composed of spur gear pairs, simulations are done for different sun-planet and ring-planet contact ratios, respectively. In all simulations in this section, backlash between mating gear pairs are constant at 1mm; whereas, all damping ratios are equal to 0.06. Three harmonics are used in the solution. In the first set of simulations, the contact ratio for ring-planet pair is kept as constant at 1.937. For this set, example PGT in Table 2-1 is used with $Z_s = 36$, $Z_r = 80$. Figure 3-16 shows the dynamic responses for both cases in terms of sun-planet dynamic elastic forces.

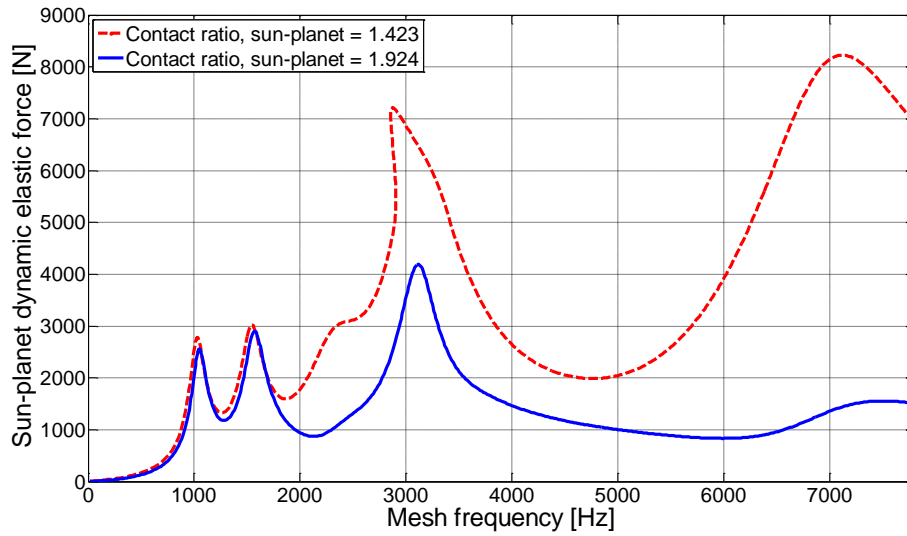


Figure 3-16 Dynamic sun-planet elastic forces (rms) for different contact ratios of sun-planet gears

Maximum of the sun-planet dynamic forces, which occur as a result of the excitation of the second in-phase mode by the first harmonic of mesh stiffness variation, is lower for the higher contact ratio of 1.924 compared contact ratio of 1.423. The same statement can also be made for the first in-phase mode. A similar comparison study is also performed for varying ring-planet contact ratios to observe the effects on ring-planet dynamic forces (Figure 3-17). Here contact ratio for the sun-planet meshes are held constant at 1.924; whereas, two different contact ratios for ring-planet meshes are studied. These results also show that contact ratios closer to an integer are favorable for better dynamic response. Slight increase in resonance frequencies is also observed for the higher contact ratio, due to the increased mean stiffness between sun and planet pairs.

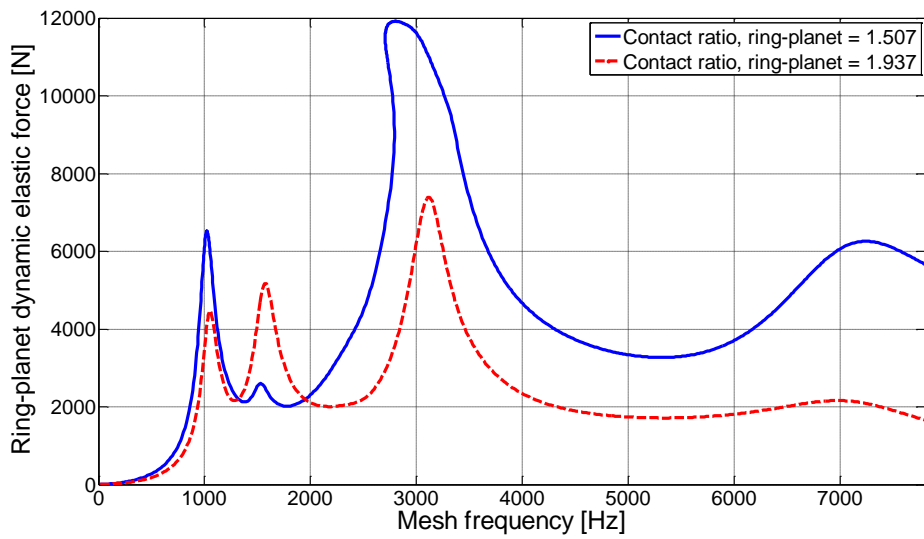


Figure 3-17 Dynamic ring-planet elastic forces (rms) for different contact ratios of ring-planet gears

For PGTs, since the sun-planet dynamics are coupled with ring-planet pairs, the effect of changing the contact ratio of the planet-ring pair also affects the dynamic response of sun gear. Figure 3-18 and Figure 3-19 show the response in terms of sun displacement and sun-planet dynamic forces respectively for the cases where sun-planet gear contact ratio is held constant at 1.924, whereas the contact ratios for ring-planet gear are 1.507 for the first case and 1.937 in the second one.

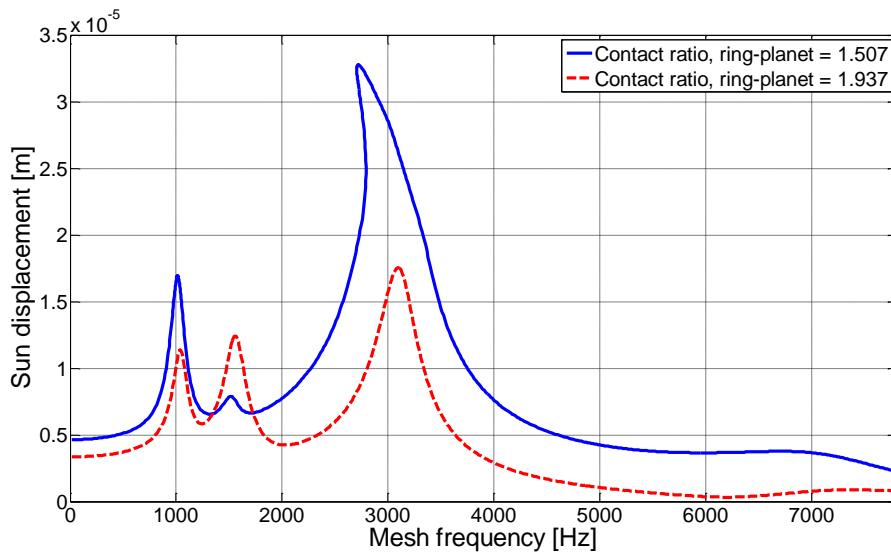


Figure 3-18 Sun displacement (rms) for different contact ratios of ring-planet gears

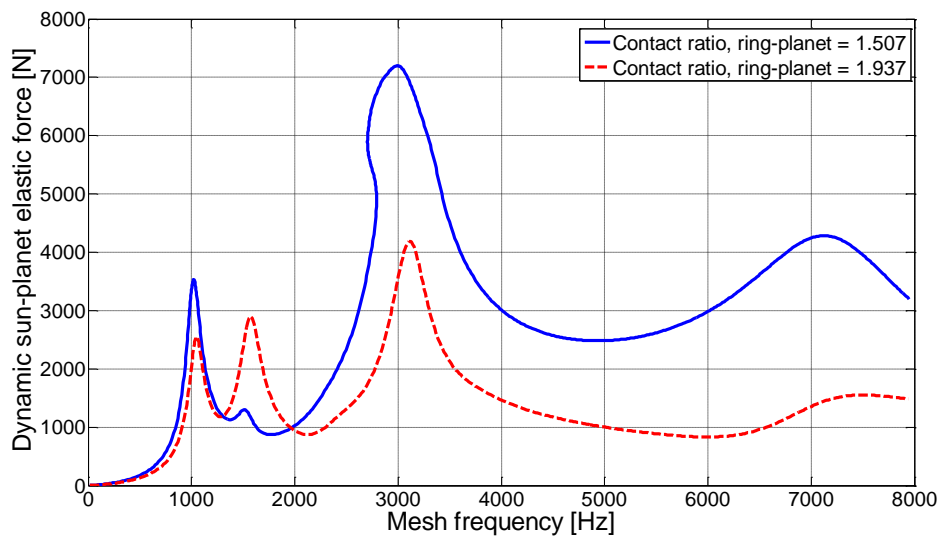


Figure 3-19 Dynamic sun-planet elastic forces (rms) for different contact ratios of ring-planet gears

The maximum values for both response types are lower for the case where the contact ratio of the ring-gear planet is 1.937, since the first harmonic of the mesh

stiffness variation is lower for this case. However for other harmonics of mesh stiffness excitation, different outcomes may be reached as this is also evident from Figure 3-18 and Figure 3-19.

A similar behavior is also observed for the ring-planet response for the first case where contact ratios of the ring-planet gears are held constant at 1.937. Two simulations with different sun-planet contact ratios are performed (Figure 3-20).

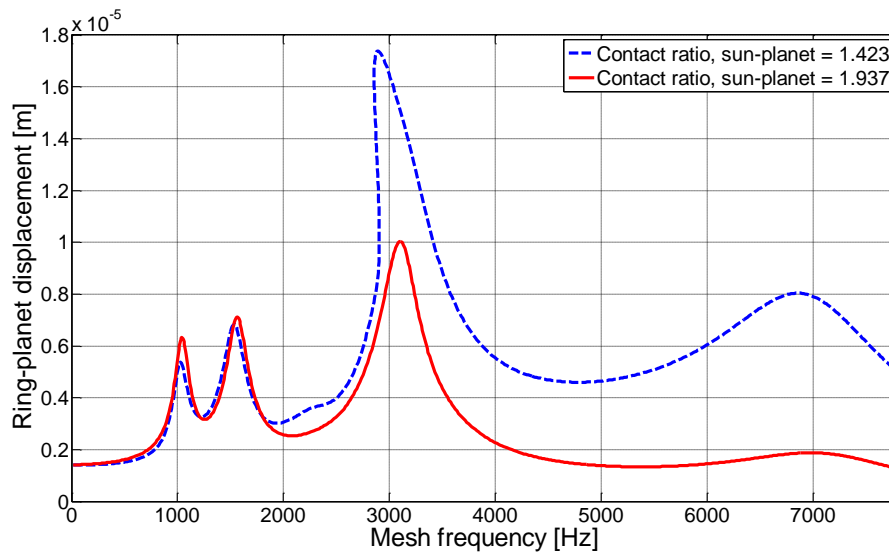


Figure 3-20 Ring-planet displacement (rms) for different contact ratios of sun-planet gears

The dynamic response in terms of ring-planet displacement is lower for the case where the contact ratio of sun-planet gear is higher.

Although gear designers usually do not want to have low contact ratios due to inferior static load carrying characteristics than their higher ratio counterparts; it is still interesting to observe the dynamic characteristics of such gears. Figure 3-21 shows the dynamic responses in terms of planet displacement for three different contact ratio scenarios. In the first case, both sun-planet and ring-planet pairs have

contact ratios that are very close to 1.0; whereas, in the second case, sun-planet and ring-planet pairs have contact ratios close to 2.0. Both contact ratios for the third case are equal to 1.52.

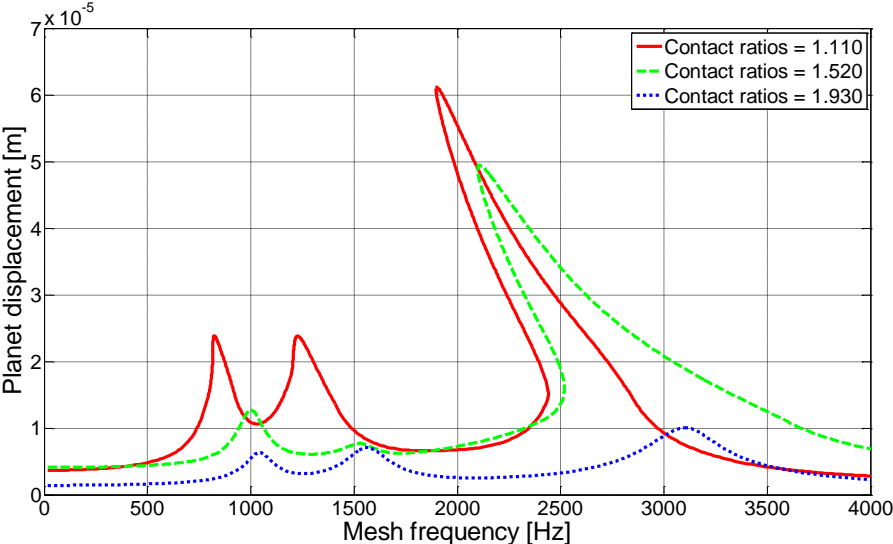


Figure 3-21 Dynamic ring-planet elastic forces (rms) for different contact ratios of sun-planet gears

Figure 3-21 shows that contact ratios close to 1.0 have also disadvantages in terms of dynamic characteristics; whereas, one can obtain very quiet gears when the contact ratios are close to 2.0. There is not much difference between vibration levels of the case with contact ratios close to 1.0 and the case with contact ratio around 1.5. The different resonance frequencies due to the different average mesh stiffness values are also apparent in Figure 3-21.

3.3 Summary and Conclusion

Effects of different mesh-phasing configurations and fundamental parameters of PGTs are investigated within this chapter. Important findings come forward as the outcome of the related studies.

Mesh phasing is one of the most important tools to tune the vibration characteristics of the PGTs. Mesh phasing characteristics of the PGTs define which modes can be excited within the operational speed range. In-phase modes are excited by in-phase harmonics of excitation whereas sequentially-phased modes are excited by sequentially-phased harmonics only.

In-phase modes are dynamically more dominant than their sequentially-phased counterparts. Therefore, for wide operational speed ranges, it is best to avoid such a configuration for a PGT design. Although sequentially-phased modes are less violent, there can still be a need for reduction of the dynamic response for these modes.

Backlash is one of the major sources of nonlinearity for PGTs with spur gears. Depending on the amount of backlash and the external force, double-sided contact may occur in addition to the loss of contact phenomenon. At a constant torque level, having a sufficient amount of backlash removes the possibility of double-sided contact, which causes higher dynamic forces when compared with dynamic forces in loss of contact condition.

Damping is usually a parameter which cannot be precisely designed for gear trains. An increased damping results in reduction of dynamic response and nonlinear effects.

Contact ratio is one of the key design parameters not only for PGTs but all geared systems. For low contact ratio spur PGTs, having a contact ratio closer to 2 greatly reduces the dynamic response levels. The contact ratio value for a sun-planet gear also affects the dynamics of the ring-planet pairs and vice versa.

The following suggestions can be made when the dynamic response of a PGT is required to be tuned and/or reduced:

- The first step is going to be to adjust mesh phasing of the respective PGT according to the operational speed ranges. Avoid excitation of in-phase modes by the first few harmonics of mesh stiffness function.
- Design PGT in such a way that the contact ratios between both sun-planet and ring-planet pairs are close to 2.
- If the damping of a PGT is not high enough to avoid nonlinear dynamic response and if it is not possible to provide any additional damping to the system, make sure that the amount of backlash is sufficient to avoid double-sided contact condition.

Here, it should be repeated that the above guideline is valid for the cases where TPM is not considered. Other design limitations may also result in deviations from the suggested plan. TPM is also an effective means for the reduction of dynamic response in geared systems. The effect of TPM in spur gear pairs are investigated in Chapter 5; whereas, Chapter 6 is dedicated to the effects and characteristics of TPMs in PGT dynamics.

CHAPTER 4

EFFECTS of RING GEAR ELASTICITY on PGT DYNAMICS

4.1 Introduction

It is common practice in rotorcraft industry to use PGTs with thin rims. Thin-rimmed PGTs have advantages not only in terms of weight but also load sharing. In terms of load sharing, the effect of using a thin-rimmed ring gear is shown to be similar to using a “floating” sun gear [35], i.e. a sun gear that is mounted such that the sun gear is compliant in translational directions. Floating sun gear configurations are known for their ability to compensate the assembly errors. Increased compliance of thinner ring gears similarly allow to compensate for the manufacturing errors induced in the design of PGTs, which have a negative effect on load sharing characteristics.

In this chapter, the focus is on the investigation of the effects of thin-rimmed ring gears on torsional dynamics of PGTs. In-plane translational motions are not considered. The effects of the rim thickness and mounting configuration of the ring gear on the mesh stiffness of ring-planet pairs are analytically modeled. Afterwards, direct relationships between the mentioned parameters and dynamic responses of PGTs are analyzed in frequency domain using HBM. Solutions of the nonlinear algebraic equations are obtained by using Newton’s method with arc-length continuation.

4.2 Analytical modeling of ring gear elasticity

When the effect of rim stiffness is taken into account, one can formulate the mesh stiffness between the ring and the planets as follows:

$$\frac{1}{K_{mesh,elastic}} = \frac{1}{K_{mesh,rigid}} + \frac{1}{K_{rim}} \quad (4.1)$$

Here the system is modeled as two springs in series; the mesh stiffness between ring and planet gear teeth is denoted as $K_{mesh,rigid}$ whereas the elasticity of the rim region of the ring gear is denoted as K_{rim} .

Calculation of $K_{mesh,rigid}$ is performed using WindowsLDP, which is a contact mechanics tool specialized in spur and helical gears, similar to previous studies.

For the calculation of the stiffness term of the elastic rim structure, the analytical formulas provided in the study of Gasmi et al. [58] are used. Authors utilized Timoshenko curved beam theory combined with virtual work principles to attain closed-form formulas for deformation of extensible and shear-deformable curved beams.

Schematics for the uniformly deformed curved beam model can be found in Figure 4-1. Note that no distributed loading is considered, since the ring gear of a PGT is of interest, and the rim in this case is expected to be loaded only by gear mesh action between the ring gear and the planets, which can be modeled as a number of concentrated loads.

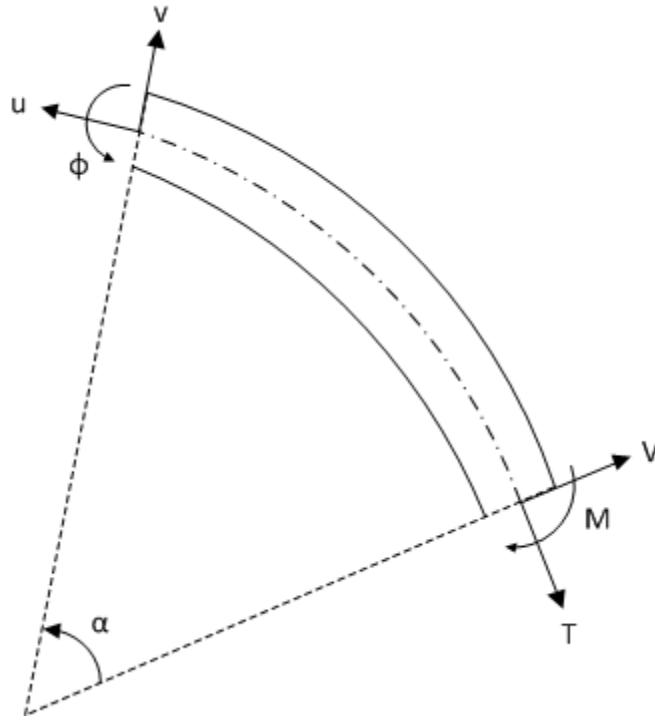


Figure 4-1 Uniformly deformed curved beam

Ring gear is modeled as $(n+m)$ uniformly deformed curved beams. At the end of each uniformly deformed curved beam, either a boundary condition or an external forcing is present. Here n is the number of points where boundary conditions (supports) are defined and m is the number of points on which external forces/moments are applied. The schematics for the ring gear model can be found in Figure 4-2.

Equations of motion for the uniformly deformed curved beam can be defined as follows

$$v(\alpha) = -C_2 - C_3 \cos \alpha + C_4 \sin \alpha - C_5 (\alpha \cos \alpha + P_1 \sin \alpha) + C_6 (\alpha \sin \alpha - P_1 \cos \alpha), \quad (4.2)$$

$$u(\alpha) = C_1 + C_2 \alpha + C_3 \sin \alpha + C_4 \cos \alpha + C_5 \alpha \sin \alpha + C_6 \alpha \cos \alpha, \quad (4.3)$$

$$\varphi(\alpha) = C_1 \frac{1}{R} + C_2 \frac{\alpha}{R} + C_5 P_2 \cos\alpha - C_6 P_2 \sin\alpha, \quad (4.4)$$

$$T(\alpha) = \frac{P_3}{R} (C_5 \sin\alpha + C_6 \cos\alpha), \quad (4.5)$$

$$V(\alpha) = \frac{P_3}{R} (-C_5 \cos\alpha + C_6 \sin\alpha), \quad (4.6)$$

$$M(\alpha) = C_2 \frac{EI}{R} - P_3 (C_5 \sin\alpha + C_6 \cos\alpha), \quad (4.7)$$

where

$$P_1 = \frac{R^2 GA EA + E I EA - E I GA}{R^2 GA EA + E I EA + E I GA}, \quad P_2 = \frac{2 R GA EA}{R^2 GA EA + E I EA + E I GA}, \quad (4.8)$$

$$P_3 = \frac{2 E I GA EA}{R^2 GA EA + E I EA + E I GA}.$$

Details of the derivation of the these equations can be found in [58].

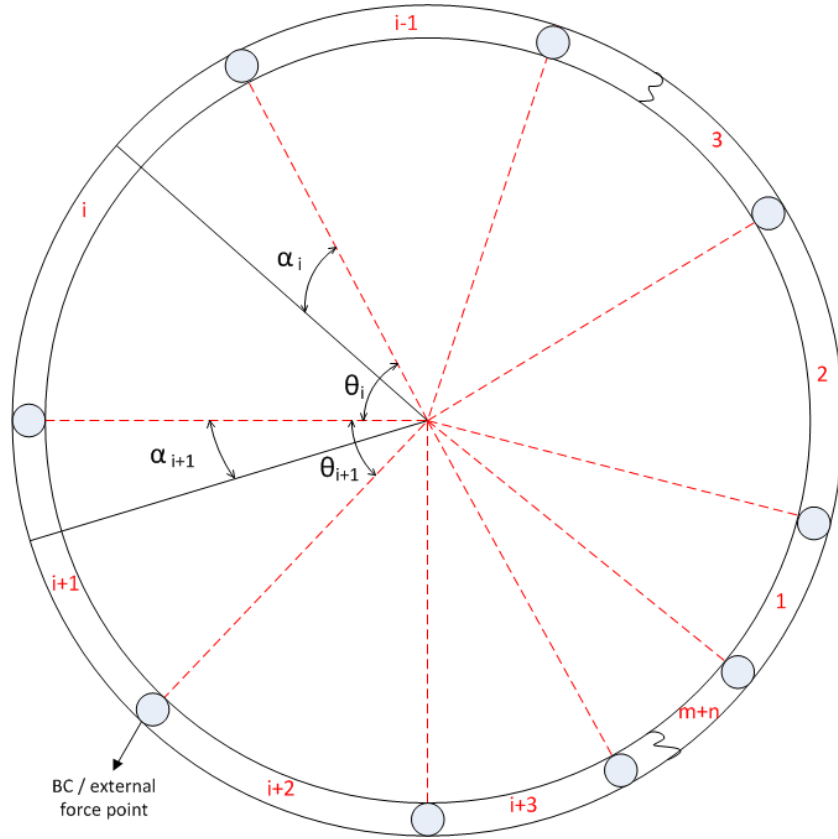


Figure 4-2 Ring gear model as a combination of uniformly deformed curved beams

The unknowns C_1 to C_6 can be found using the boundary conditions. Boundary conditions for “fixed” supports are given as follows

$$u(\alpha_i) = 0, u(\alpha_{i+1}) = 0, v(\alpha_i) = 0, \quad (4.9)$$

$$v(\alpha_{i+1}) = 0, \varphi(\alpha_i) = \varphi(\alpha_{i+1}), M(\alpha_i) = M(\alpha_{i+1}).$$

For the support points, when Eq. 4.9 is inserted in to Eqs. 4.2 - 4.7, the equations of motion are obtained

$$C_1^i + C_2^i \alpha_i + C_3^i \sin \alpha_i + C_4^i \cos \alpha_i + C_5^i \alpha_i \sin \alpha_i + C_6^i \alpha_i \cos \alpha_i = 0, \quad (4.10)$$

$$C_1^{i+1} + C_4^{i+1} = 0, \quad (4.11)$$

$$\begin{aligned} C_2^i + C_3^i \cos \alpha_i - C_4^i \sin \alpha_i + C_5^i (\alpha_i \cos \alpha_i + P_1 \sin \alpha_i) - C_6^i (\alpha_i \sin \alpha_i - P_1 \cos \alpha_i) \\ - C_2^{i+1} - C_3^{i+1} - C_6^{i+1} P_1 = 0 \end{aligned}, \quad (4.12)$$

$$C_5^i \cos \alpha_i - C_6^i \sin \alpha_i - C_5^{i+1} = 0, \quad (4.13)$$

$$\frac{1}{R} C_1^i + \frac{1}{R} C_2^i \alpha_i + C_5^i P_2 \cos \alpha_i - C_6^i P_2 \sin \alpha_i - \frac{1}{R} C_1^{i+1} - C_5^{i+1} P_2 = 0, \quad (4.14)$$

$$C_2^i \frac{EI}{R^2} - C_5^i P_3 \sin \alpha_i - C_6^i P_3 \cos \alpha_i - C_2^{i+1} \frac{EI}{R^2} + C_6^{i+1} P_3 = 0. \quad (4.15)$$

For the connection point between the segments of the ring gear, if an external force and moment are applied, the compatibility equations for the respective point can be defined as

$$u(\alpha_i) = u(\alpha_{i+1}), \quad v(\alpha_i) = v(\alpha_{i+1}), \quad \varphi(\alpha_i) = \varphi(\alpha_{i+1}), \quad (4.16)$$

$$M(\alpha_{i+1}) - M(\alpha_i) = M_0, \quad V(\alpha_{i+1}) - V(\alpha_i) = F_r, \quad T(\alpha_i) - T(\alpha_{i+1}) = F_t.$$

Substituting Eq. 4.16 into Eqs. 4.10 - 4.15, the following equations are obtained

$$-C_1^i - C_2^i \alpha_i - C_3^i \sin \alpha_i - C_4^i \cos \alpha_i - C_5^i \alpha_i \sin \alpha_i - C_6^i \alpha_i \cos \alpha_i + C_1^{i+1} + C_4^{i+1} = 0, \quad (4.17)$$

$$\begin{aligned} C_2^i + C_3^i \cos \alpha_i - C_4^i \sin \alpha_i + C_5^i (\alpha_i \cos \alpha_i + P_1 \sin \alpha_i) - C_6^i (\alpha_i \sin \alpha_i - P_1 \cos \alpha_i) \\ - C_2^{i+1} - C_3^{i+1} - C_6^{i+1} P_1 = 0 \end{aligned}, \quad (4.18)$$

$$-\frac{1}{R} C_1^i - \frac{1}{R} C_2^i \alpha_i - C_5^i P_2 \cos \alpha_i + C_6^i P_2 \sin \alpha_i + \frac{1}{R} C_1^{i+1} + C_5^{i+1} P_2 = 0, \quad (4.19)$$

$$-C_2^i \frac{EI}{R^2} + C_5^i P_3 \sin \alpha_i + C_6^i P_3 \cos \alpha_i - C_2^{i+1} \frac{EI}{R^2} + C_6^{i+1} P_3 = M_0, \quad (4.20)$$

$$\frac{P_3}{R} (C_5^i \cos \alpha_i - C_6^i \sin \alpha_i - C_5^{i+1}) = F_r, \quad (4.21)$$

$$\frac{P_3}{R} (C_5^i \sin \alpha_i + C_6^i \cos \alpha_i - C_6^{i+1}) = F_t. \quad (4.22)$$

Figure 4-3 shows a schematic of the decomposition of the gear forces and displacements on to the rim structure.

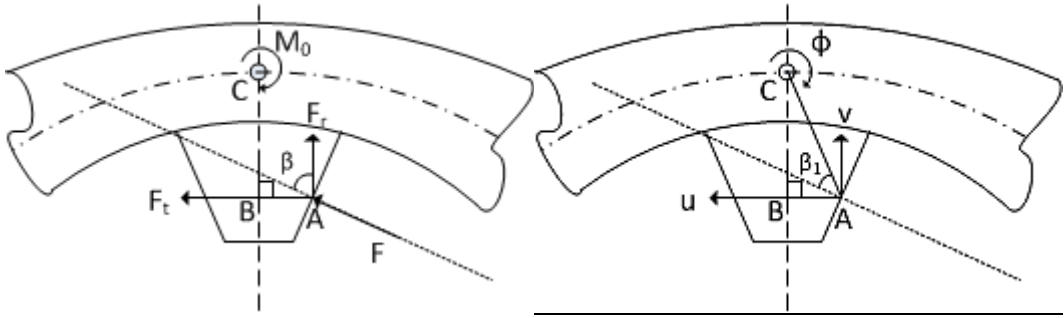


Figure 4-3 Mesh displacements and mesh forces imposed on the rim structure

$$F_t = F \sin \beta, \quad F_r = F \cos \beta, \quad M_0 = F_t |CB| - F_r |AB|. \quad (4.23)$$

External forces acting on the curved beam segments are the radial and tangential components of the gear mesh forces, F_r and F_t , respectively, and the moment created by these forces at the centroid of the uniformly deformed curved beam, M_0 .

The displacement along the line of action which is defined by the pressure angle of the gears is given by

$$d_{LoA} = v \cos \beta + u \sin \beta + \phi |CA| \sin \beta_1. \quad (4.24)$$

Therefore the stiffness of the rim is calculated as

$$K_{rim} = \frac{F}{d_{LoA}}. \quad (4.25)$$

The validity of the analytical modeling of the rim of the ring gears using uniformly deformed beams is verified by comparing the results of the model with FE results. Parameters of an example ring model considered for this study are given in Table 4-1.

Table 4-1 Parameters for analytical rim model validation study

Radius from centroid of the ring [mm]	115
Width of the ring [mm]	10
Thickness of the ring [mm]	10
Elastic modulus [GPa]	206
Tangential force [N]	4762
Radial force [N]	1856

Figure 4-4 shows the FE model and the boundary conditions and force application points. FE model is created in Msc Patran and it consists of 1D elements with CBEAM formulation. The boundary conditions and the external forces represent an example case of a 3-planet PGT, which is fixed at 3 points. The tangential and radial components of forces are present due to the respective gear mesh forces, where the pressure angle is 21.3° between ring gear and mating planets. The tangential component represents the forcing along the tangential direction of the pitch circle of

the ring gear, whereas radial component is perpendicular to the tangential direction of the pitch circle of the ring gear. A mesh force of 5111N results in the force components provided in Table 4-1. The force application points and boundary condition points are selected such that they represent an arbitrarily random case, where the spacing of each force between the respective adjacent boundary conditions is different. The boundary conditions are located at $\theta=0^\circ$, $\theta=90^\circ$ and $\theta=240^\circ$, while the gear mesh forces are applied at $\theta=60^\circ$, $\theta=180^\circ$ and $\theta=300^\circ$.

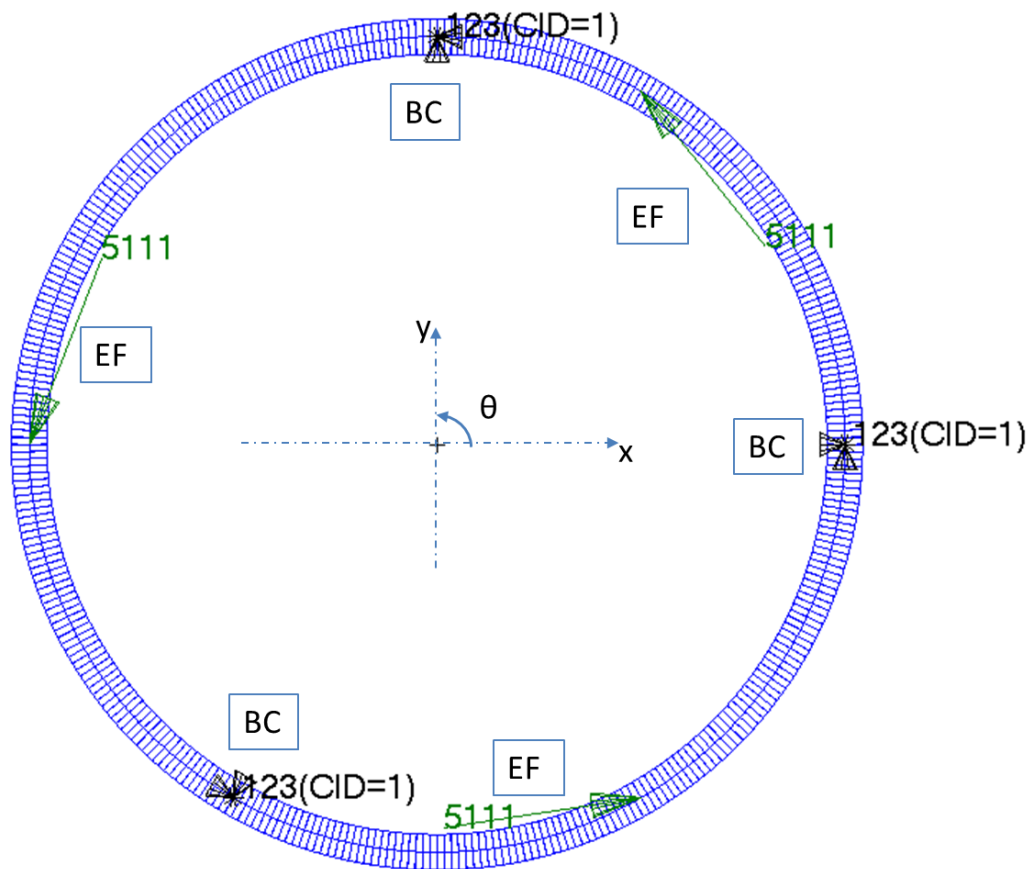


Figure 4-4 1D FE model with applied forces and boundary conditions

Figure 4-5 shows the comparison of radial displacement results between the analytical model and FE model which verify the analytical model used, and hence

the calculation method for rim stiffness. Therefore, the analytical method is used for the calculation of rim stiffness in order to investigate the effects of rim stiffness on PGT dynamics.

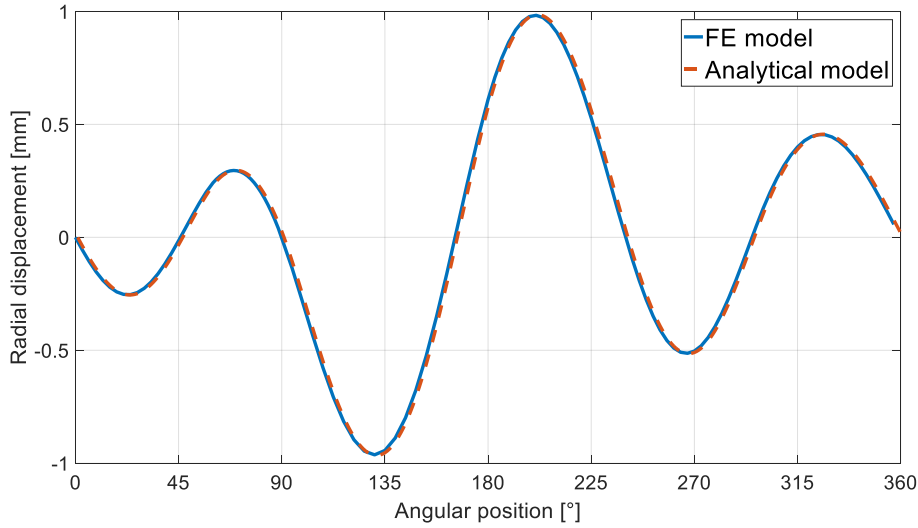


Figure 4-5 Comparison of radial displacement results between analytical model and FE model

Effects of rim stiffness on PGTs are investigated considering two parameters, i.e. rim thickness and the number of constraints. A non-dimensional parameter for the rim thickness can be defined as

$$T = \frac{2(R_{out} - R_{root})}{R_{out} + R_{root}}. \quad (4.26)$$

Here R_{out} is the outer radius of the ring gear where as R_{root} is the radius of the tooth root circle of the ring gear. The variation of mesh stiffness with respect to dimensionless rim thickness parameter, T, is analyzed for the parameter set given in

Table 4-2. Different rim thickness parameters are obtained by changing the rim thickness only, i.e. root diameter of the ring is kept as constant. In order to observe the effect of rim thickness on the overall mesh stiffness, $K_{mesh,elastic}$, an example case with 6 equally-spaced constraints is considered. $K_{mesh,rigid}$ is assumed to be constant in these analyses.

Table 4-2 Parameters of ring gear for mesh stiffness variation study

Pressure angle [°]	21.3
Tooth thickness [mm]	6.784
Root diameter of ring [mm]	320
Facewidth [mm]	30
Number of constraints	6
Number of planets	3
E [GPa]	206
ν	0.3
$K_{mesh,rigid}$ [N/mm]	6.35e5

Figure 4-6 gives the ring-planet mesh stiffness variation between the fixed constraints for a planet gear traveling between two constraints for the parameter set provided in Table 4-2.

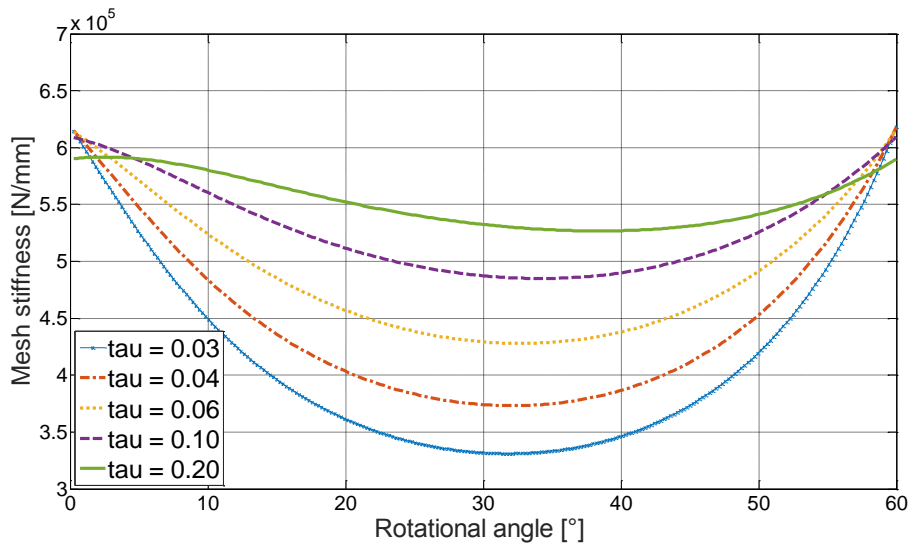


Figure 4-6 Variation of mesh stiffness between constraints for different rim thickness parameters

It is observed that a thinner rim results in more variation of the mesh stiffness as the planet goes from one support to the other. However as the rim gets thicker, the change in the mesh stiffness becomes very small; hence, above certain rim thickness value the deviation due to rim size can be neglected.

Another important parameter is the number of constraints, which dictates the periodicity of mesh stiffness variation. As the number of constraints increases, the period of mesh stiffness variation increases; however, the amplitude of this variation is expected to be smaller.

Figure 4-7 shows an example case for the parameter set given in Table 4-2, where rim thickness parameter is kept constant.

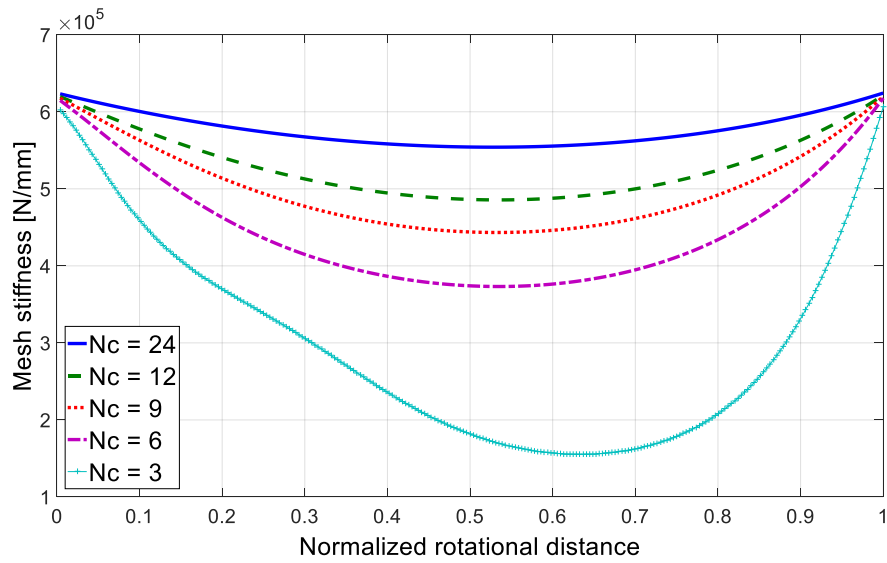


Figure 4-7 Effect of number of constraints (N_c) for the mesh stiffness of the ring planet pair, $T = 0.04$

For the dynamic analyses, instead of an average value, a time-varying $K_{mesh,rigid}$ is combined with the analytically calculated K_{rim} , according to Eq. 4.1. Figure 4-8 shows a typical mesh stiffness function for a PGT with an elastic ring. This plot is obtained for a case where the number of planets is 4 and there are 12 constraints around the ring gear. The higher mesh harmonics are combined with the lower frequency content of variation due to ring elasticity. The periodicity of this lower frequency content of variation is dependent on the number of constraints on the ring gear.

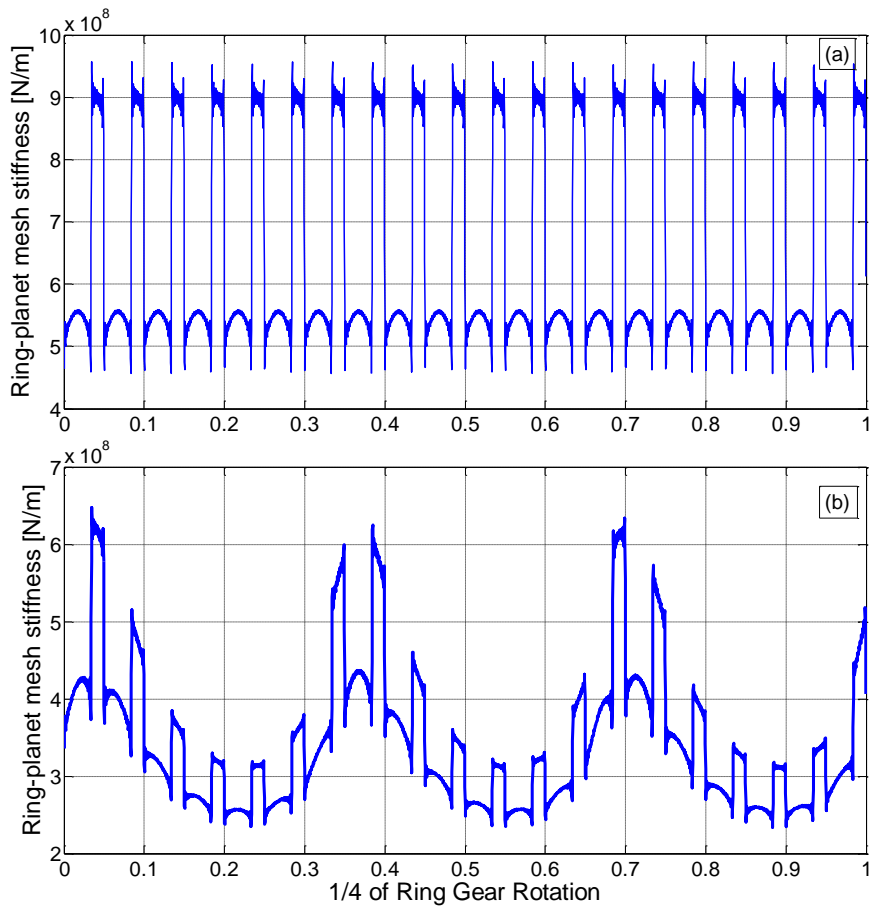


Figure 4-8 Ring-planet mesh stiffness for a PGT with 4 planets and 12 constraints around ring gear, a) Rigid ring gear, b) Elastic ring gear

4.3 Effects of ring gear elasticity parameters on PGT dynamic response

As a first step, before investigating the effects of the related ring gear elasticity parameters on the PGT dynamic response, a comparison study is performed on an example PGT (Table 4-3). The dynamic responses are compared for 2 different variations of the example PGT. In the first one, the ring gear is modeled as rigid; whereas, in the second one, it is modeled as flexible.

Table 4-3 PGT used in elastic rim dynamic response simulations

	Sun	Planet	Ring
Number of planets	3		
Number of teeth	36	21	81
Module [mm]	4		
Pressure angle [deg]	21.3		
Effective outside diameter [mm]	146	91	320
Root diameter [mm]	135	76	333
Facewidth [mm]	30		
Transverse tooth thickness [mm]	5.3	6.8	5.3
Diameter at measured tooth thickness	144	84	324
Torque applied [Nm]	1800	-	-
Young's modulus [GPa]	206.8		
Number of constraints (for elastic ring gear)	9		
T (for elastic ring gear)	0.058		

In order to show the resonant frequency characteristics, the comparisons are to be made with a linear model. Figure 4-9 shows the response plot of PGT with elastic rim in terms of sun-planet displacement for the compliant rim model. For this case study, overall mesh stiffness, $K_{mesh,elastic}$, is represented by 6 harmonics. Use of two harmonics is evaluated to be sufficient for the representation of rim elasticity contribution to the variation of mesh stiffness, K_{rim} , since this variation resembles to a sine wave; whereas, tooth mesh stiffness, $K_{mesh,rigid}$, is represented by four

harmonics, since the higher tooth mesh stiffness harmonics have much lower amplitudes when compared with the first 4 harmonics.

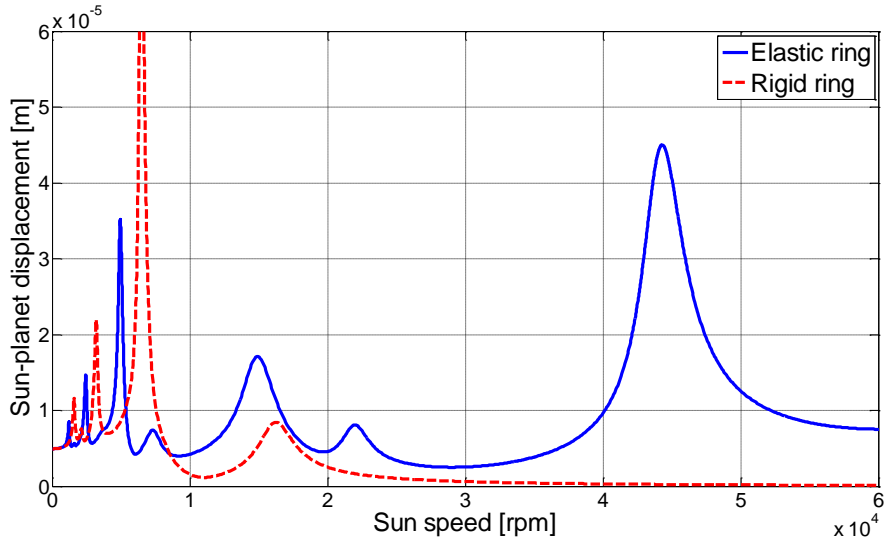


Figure 4-9 Sun-planet displacement (rms) comparison for elastic vs. rigid ring gear

The reduced mean ring-planet mesh stiffness resulted in lower natural frequencies for the PGT with elastic ring gear compared to the rigid ring gear. Moreover, for the elastic ring gear case, the additional harmonic content due to the rim elasticity is also able to excite the first in-phase natural mode of the system at higher speeds, as the frequency of the stiffness excitation due to rim elasticity is much lower than frequency of the tooth stiffness variation. In Figure 4-9, the peaks observed at sun speed of 43000 rpm and 21500 rpm correspond to the excitation of the first in-phase mode of the example PGT by the first and the second harmonics of the rim stiffness variation, respectively.

The effects of the ring thickness parameter on dynamic response of PGTs are going to be investigated next. A comparison study is performed for 4 different cases in terms of rim thickness, including the rigid ring gear case. The example PGT given in Table 4-3 is going to be used for this purpose. The number of constraints of ring

gear for these analyses is arbitrarily kept constant at 9. Figure 4-10 and Figure 4-11 show the sun gear displacement and planet displacement, respectively, for different rim thickness values.

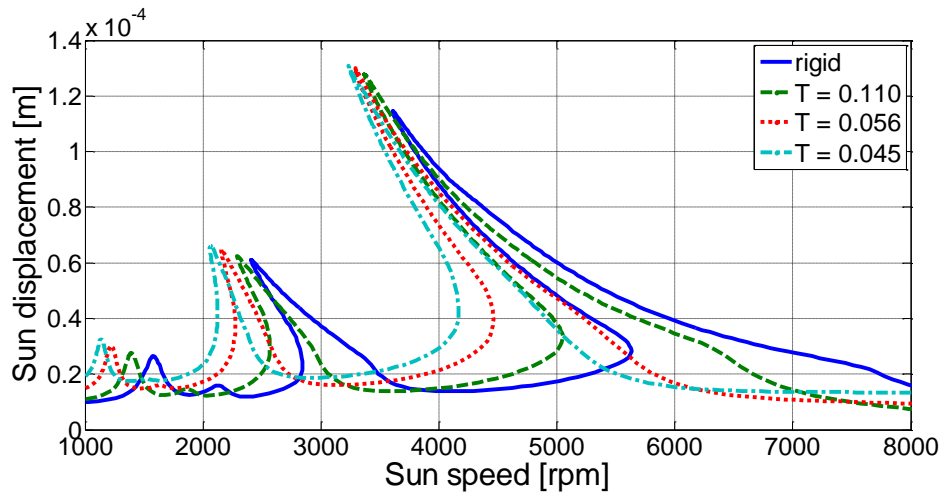


Figure 4-10 Sun displacement (rms) for different values of rim thickness values (T)

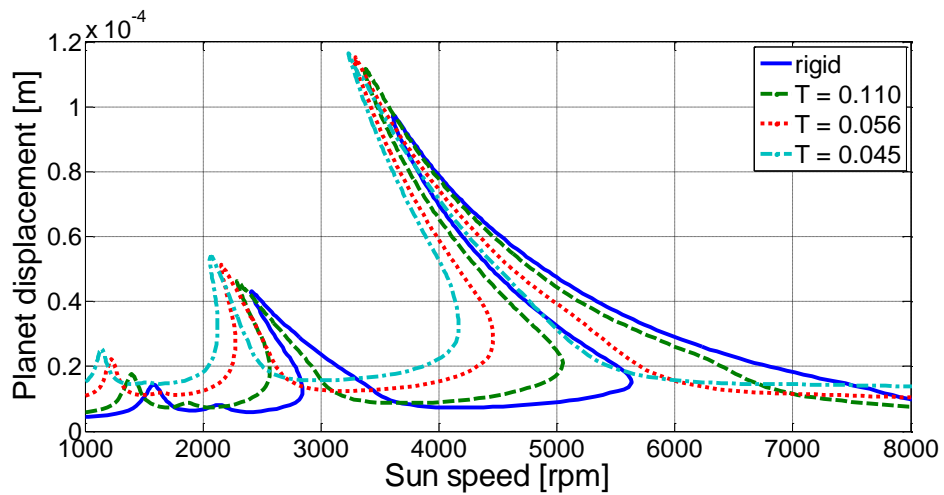


Figure 4-11 Planet displacement (rms) for different values of rim thickness values (T)

The decrease in mean mesh stiffness between ring and planet gears resulted in a slight increase in terms of planet response and sun displacement response. Moreover, natural frequencies also decrease for the PGT configurations with thinner rims. Figure 4-12 shows the dynamic sun-planet elastic force as a function of sun speed in the 1000-9000 rpm interval.

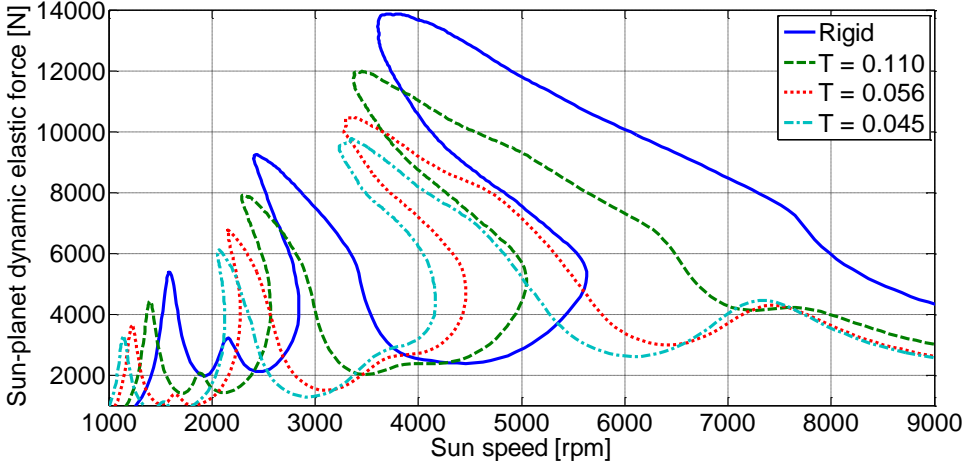


Figure 4-12 Sun-planet dynamic elastic force (rms) for different rim thickness values (T) between 1000-9000 rpm

The first in-phase mode of the PGT is excited by the gear mesh excitation and its harmonics. For this mode, it is observed that the dynamic elastic forces of the sun-planet meshes decrease as the torsional rigidity of the ring gear decreases. However Figure 4-13 shows that this characteristic observed for the first in-phase mode cannot be generalized for all natural modes of the PGTs.

Figure 4-13 shows the dynamic sun-planet elastic force plot for 12000-20000 rpm interval. It is observed that as the torsional compliance of the rim increases, the dynamic elastic forces for the sun-planet mesh increase. The common peak observed for all rim thickness configurations in this speed interval corresponds to the second

in-phase mode of the PGT. Therefore depending on the operational speed, compliant ring gears may provide reduction or increase in dynamic mesh forces.

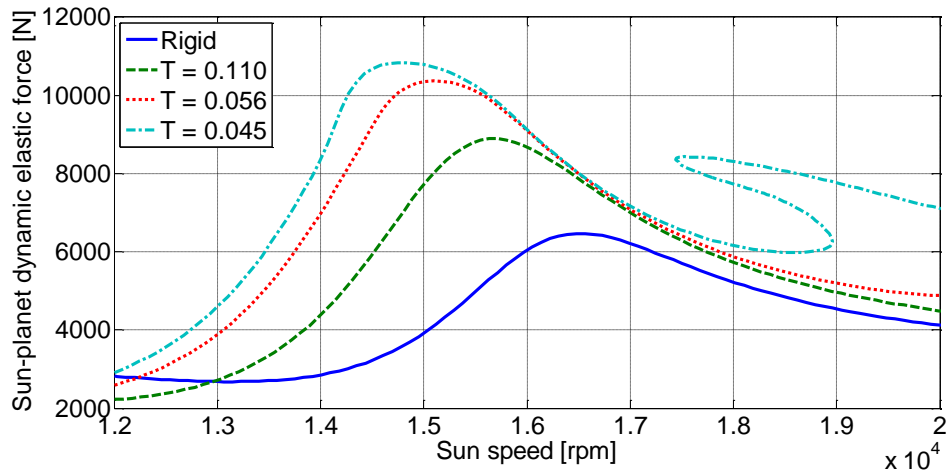


Figure 4-13 Sun-planet dynamic elastic forces (rms) for different rim thickness values (T) between 12000-20000 rpm

Figure 4-14 shows the ring-planet dynamic elastic forces for the speed interval of 1000-20000 rpm. The effect of second in-phase mode is negligible for ring-planet dynamic mesh forces, and the ring-planet dynamic elastic forces decrease with increasing compliance for the first in-phase mode.

In Figure 4-13 and Figure 4-14, for the example PGT configuration with $T = 0.045$, a nonlinear increase in dynamic mesh forces are observed around a sun speed of 18000. These peaks correspond to the excitation of the first in-phase mode by the second harmonic of the rim stiffness contribution to the ring-planet mesh stiffness. As the rim thickness decreases, the contribution of rim stiffness to the overall mesh stiffness becomes dominant and the variation in rim stiffness is able to excite the first in-phase mode of the PGT.

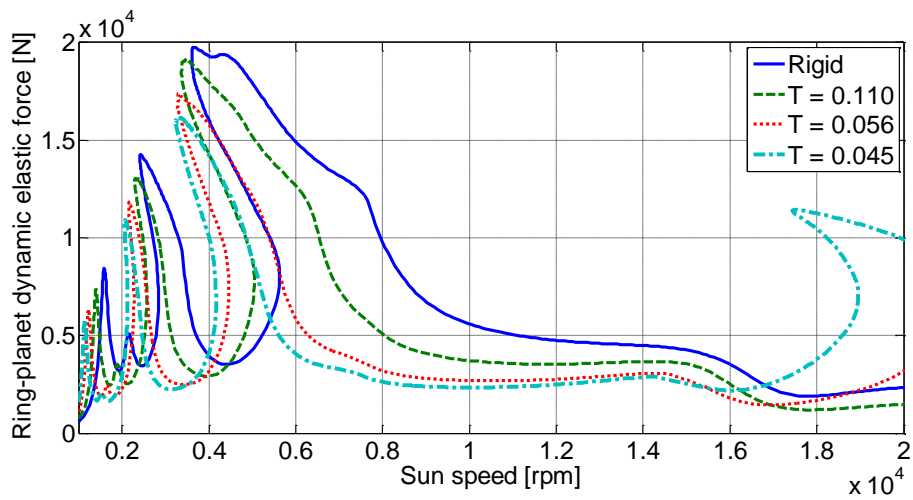


Figure 4-14 Ring-planet dynamic elastic forces (rms) for different rim thickness values (T) between 1000-20000 rpm

Next the effects of the number of ring gear constraints are investigated in detail. Figure 4-15 shows the sun displacement for different number of constraints for the example PGT given in Table 4-3. For this study, rim thickness parameter, T , is kept constant at 0.056.

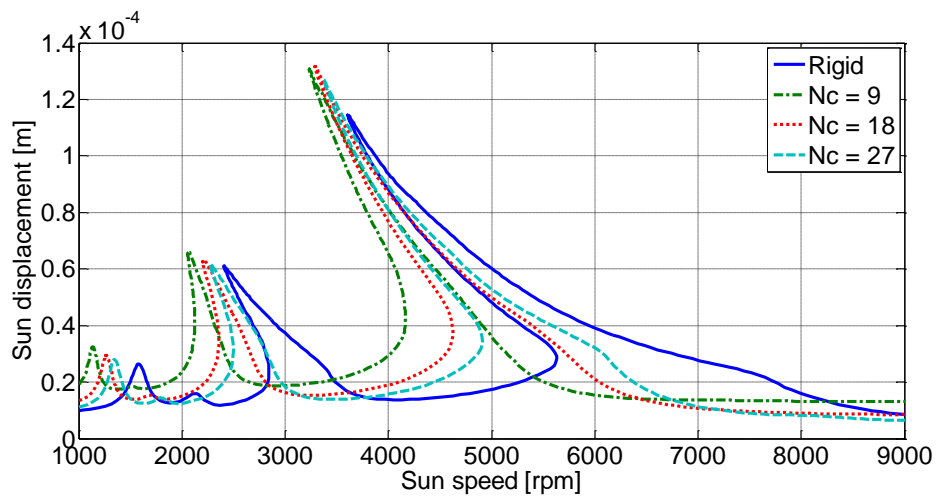


Figure 4-15 Sun displacement (rms) for different number of constraints (N_c)

Similar to the ring thickness effect, increasing the number of constraints result in stiffer ring-planet meshes; thus the natural frequencies increase and the response in terms of displacement decreases. Figure 4-16 and Figure 4-17 show response in terms of elastic sun-planet forces for different speed intervals.

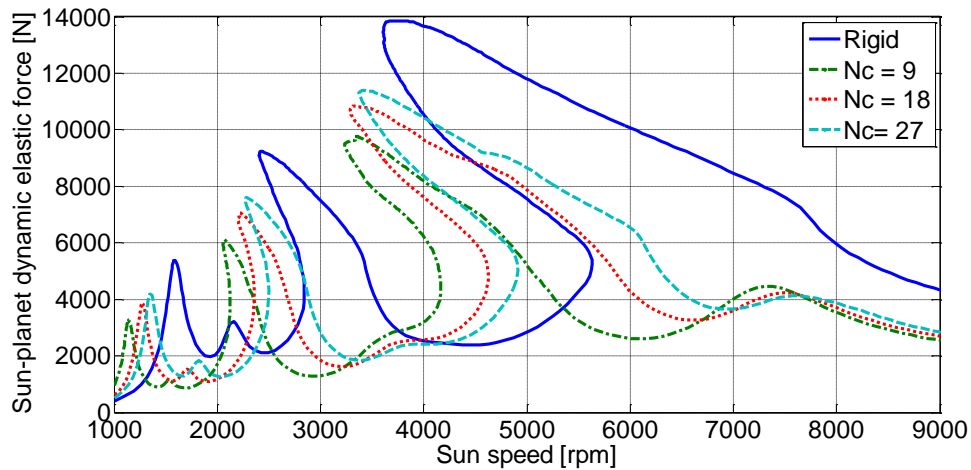


Figure 4-16 Sun-planet dynamic elastic force (rms) for different number of constraints (N_c), 1000-9000 rpm

As the compliance of ring-planet meshes increase due to the decrease in the number of constraints, sun-planet mesh forces decrease; similar to the behavior observed for the variation of the rim thickness of the PGT.

Figure 4-17 shows how the lower frequency (when compared with the mesh harmonics) excitations of the rim stiffness contribution to the ring-planet mesh stiffness can directly affect the PGT response. For the example PGT configuration with $N_c = 9$, both the first and the second harmonics of the ring-planet mesh stiffness variation due to the rim elasticity are able to excite the first in-phase mode of the related PGT configuration, at around 22000 rpm and 18000rpm, respectively. As the number of constraints increase, these mentioned excitations occur at lower speed values. For $N_c = 18$, only the first harmonic of rim elasticity contribution to

the ring-planet mesh stiffness excites the first in-phase mode at around 17000 rpm. As the number of constraints increase, the compliance of the ring gear decreases, therefore rim-based excitations become weaker. For $N_c = 27$, both the first in-phase mode (at around 15000 rpm) and the second in-phase mode (at around 47000 rpm) are excited by the first rim stiffness harmonic excitation, however the response levels are not as high as those observed for lower number of constraints.

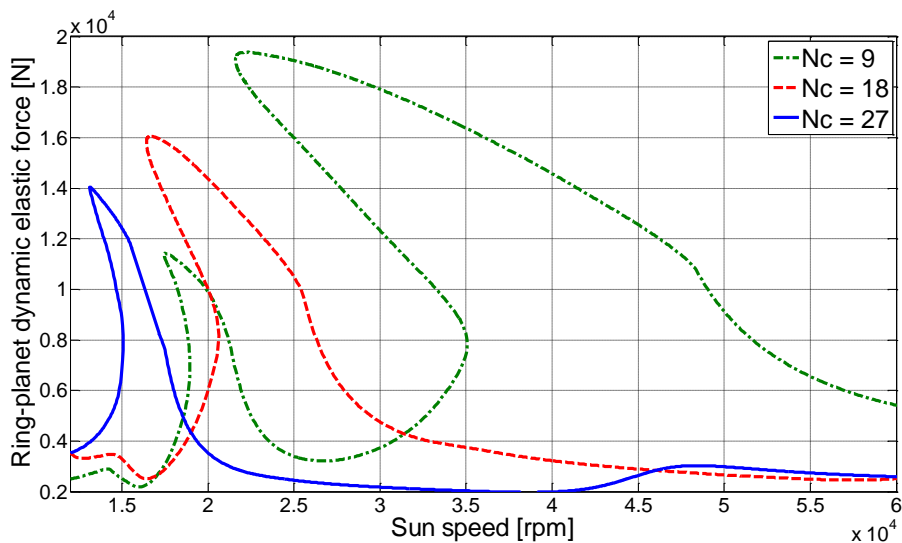


Figure 4-17 Ring-planet dynamic elastic force (rms) for different number of constraints, 12000-60000 rpm

4.4 Summary and Conclusion

Effects of the torsional elasticity of the ring gear on PGT dynamics is investigated in this chapter. The rim section of the ring gear is modeled using analytical curved beam theory to include the rim elasticity effect on the mesh stiffness of ring-planet pairs. The analytical model is also verified by a conventional FE tool and hence, it is used in later studies as a fast and effective way of including the rim stiffness effects on ring-planet mesh stiffness.

In the PGTs where ring gear is fixed, the ring gears are usually connected to a housing member by using bolts or studs. The compliance of the rim gear mainly depends on the number of these mentioned constraints and the rim thickness.

After a brief overview of the effects of the mentioned parameters on the ring-planet mesh stiffness, direct effects of these parameters on PGT dynamics are investigated in detail. Besides the obvious effect of decreasing natural frequencies with increasing compliance of ring gears, some other interesting outcomes are observed.

The displacement response increases slightly with increasing compliance of the ring gears. However, for the sun-planet dynamic force response, the opposite is observed for the first in-phase mode of the example PGT under consideration. As the rim thickness decreases, the sun-planet mesh forces also decrease. On the contrary, for the speed intervals in which the second in-phase mode is excited, this is not the case as the dynamic forces are higher for the PGT configurations with more compliant ring gears than their counterparts with stiffer ring gears.

The number of constraints on a PGT with a fixed ring gear not only changes the elasticity of the ring gear but also dictates the periodicity of the lower frequency content of the mesh stiffness excitation due to the rim effects. As the number of constraints increase, this low frequency content approaches to the higher frequency content of the mesh harmonics in frequency-wise. However due to the increasing stiffness because of the increased number of constraints, the amplitude of these mentioned harmonics may be low such that their effects are negligible on the dynamic response of PGTs. These outcomes are observed on the dynamic response studies for the example PGT with different number of constraints.

Although results of the performed analyses signal for the aforementioned outcomes, it is still hard to reach general conclusions regarding how exactly rim stiffness affects the dynamic characteristics of PGTs, mostly because of the interactions of rim stiffness effects with different characteristics of the PGTs. However the distinct dynamic features that come along with ring gear compliance, which show themselves in the results of the performed analyses, indicate the necessity to include the rim elasticity effects for dynamic modeling of PGTs with compliant ring gears.

CHAPTER 5

EFFECTS OF TOOTH PROFILE MODIFICATIONS IN SPUR GEAR

DYNAMICS

5.1 Introduction

Tooth profile modifications (TPMs) are known to be effective means of reducing the dynamic response of spur gears. Before dealing with different aspects of TPMs in PGTs, firstly the effects of TPMs on spur gear dynamics are investigated. These investigations also aim to address topics that are rarely found in the literature, if any.

In spur gears, TPMs are used in order to avoid the corner contact between mating gear teeth and to diminish the adverse dynamic effects by reducing the dynamic factors which can simply be defined as the ratio of the dynamic mesh loads over static mesh loads.

Linear and parabolic modifications are the most common type of TPMs. Figure 5-1 shows diagrams of the mentioned profile modification types on respective examples. In these examples, modifications are applied both at the tip and the root sections of one of the mating gears.

Firstly, an optimization study is performed target being the reduction of dynamic transmission error (DTE) for a given operational range, where the operating torque and speed ranges are defined. For this purpose, two different models, i.e. a single degree of freedom (SDOF) lumped gear dynamics model and a multi-degree of freedom (MDOF) lumped model of a gear pair which is combined with shaft and bearing dynamics are employed. The differences between the optimization results

obtained through loaded static transmission error (LSTE) minimization and DTE minimization using different models are presented based on example spur gear pairs.

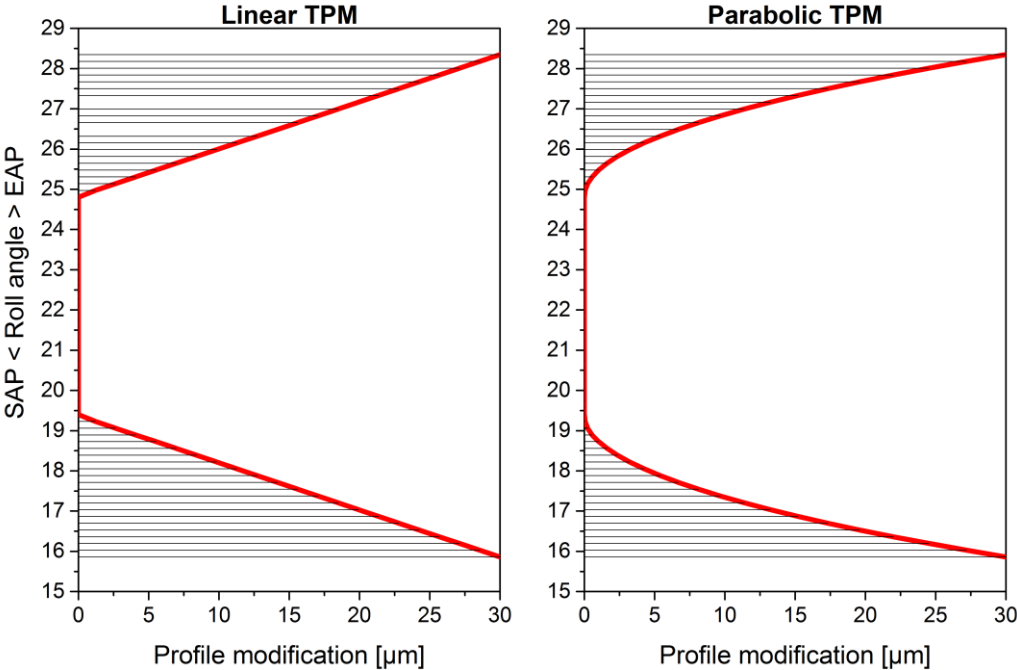


Figure 5-1 Linear and parabolic profile modifications

The second part of the study provided in this chapter deals with the direct effects of TPMs on tooth bending fatigue lives of spur gears. A gear tooth profile optimization study is performed where the target is defined as the maximization of tooth bending fatigue life for a selected operational range. In this optimization, torque and speed ranges are defined along with their corresponding durations. For this purpose, a nonlinear lumped gear dynamics model is combined with the S/N curve of the gear material in order to estimate tooth bending fatigue life of the spur gear pair. The differences between the predicted lives of the optimally modified and unmodified gear pairs are presented based on example spur gear pairs. The proposed tooth bending fatigue life estimation is compared with the standard AGMA procedure.

5.2 Optimum profile modifications for the minimization of dynamic transmission error

There exists a variety of spur gear dynamics models in the literature, which can be categorized under many different groups. A comprehensive review of gear dynamics models can be found in the study of Özgüven and Houser [59], and more recently it is given by Wang et al. [60].

In the current study, first, the model proposed by Özgüven and Houser in 1988 [61] is used in optimization. This model is based on a validated approximation, which uses LSTE rather than static transmission itself, as an excitation to a SDOF model with an average constant mesh stiffness. The equation of motion of a gear pair is given in terms of dynamic transmission error, x , as:

$$m_e \ddot{x}(t) + 2\zeta \sqrt{m_e k_{ave}} \dot{x}(t) + k_{ave} x(t) = k_{ave} x_s(t) \quad (5.1)$$

Here m_e is the equivalent mass of the gear pair, ζ is the viscous damping ratio, k_{ave} is the average mesh stiffness and x_s is the loaded static transmission error. It should be noted that even though an average (constant) mesh stiffness is used, the excitation effect of variable mesh stiffness is included into the model indirectly through LSTE. It was concluded that the displacement excitation effect of time varying mesh stiffness is more important than the effect of it in natural frequency of the system. This model was shown to be a very effective one by using experimental results for gear pairs that have no profile modification. However, the accuracy of the model is not shown for gear pairs with profile modification, especially for gears with optimum tooth profile for a given load, where the resulting LSTE variation (hence the dynamic excitation) is at very low levels.

The following equation represents the differential equation of a SDOF model of a gear pair, in which time-varying mesh stiffness is used without any approximation:

$$m_e \ddot{x}(t) + c \dot{x}(t) + k(t)x(t) = F - m_e \ddot{e}(t) \quad (5.2)$$

In this model, c is the viscous damping coefficient, $k(t)$ is the time-dependent mesh stiffness, F is the constant gear mesh force and $e(t)$ is the static transmission error due to gear errors and profile modifications (also called non-loaded transmission error) (NLTE). In 2007, it has been shown by Tamminana et al. [18] that this model yields accurate results for gear pairs with profile modification, comparing theoretical DTE values with experimental data.

Although Eq. 5.2 yields accurate results without making an approximation for the time-varying mesh stiffness, the model proposed by Özgüven and Houser is preferred in several applications as it can be easily implemented to MDOF models of gears and gear-shaft-bearing systems, providing solutions in frequency domain. However, it is found necessary to study the accuracy of this model when it is used for gears with tooth modification where LSTE is minimized.

For this purpose, dynamic analysis of the gear system described in Table 5-1 is carried out using both of the models described above. The gear pair, which is composed of identical gears, has tooth modification such that LSTE variation is reduced to a very low level for a given torque value at which the dynamic analysis is performed. Thus, when the first model is used, as the internal excitation due to mesh stiffness variation is represented by LSTE, the level of excitation on the system becomes very low. Comparison of the dynamic analysis results obtained for such a case with those of the variable mesh stiffness model will reveal the accuracy of the constant mesh stiffness model when used for gears with optimum tooth profile modification.

Table 5-1 Properties of gear pair used for comparison of both models

Number of teeth	25
Module [mm]	4
Equivalent mass [kg]	0.23
Base diameter [mm]	93.97
Face width [mm]	15
Torque applied [Nm]	107.9
Peak-to-peak LSTE (non-modified) [μm]	5.1
Peak-to-peak LSTE (modified) [μm]	0.6

Comparison is made for two damping ratio values, namely $\zeta = 0.1$ and $\zeta = 0.05$. Figure 5-2 shows the comparisons of DTEs by using both models for the specified damping values. Peak-to-peak DTE (PPDTE) values are plotted against normalized

frequency, which is defined as $\sqrt{\frac{k_{ave}}{m_e}}$.

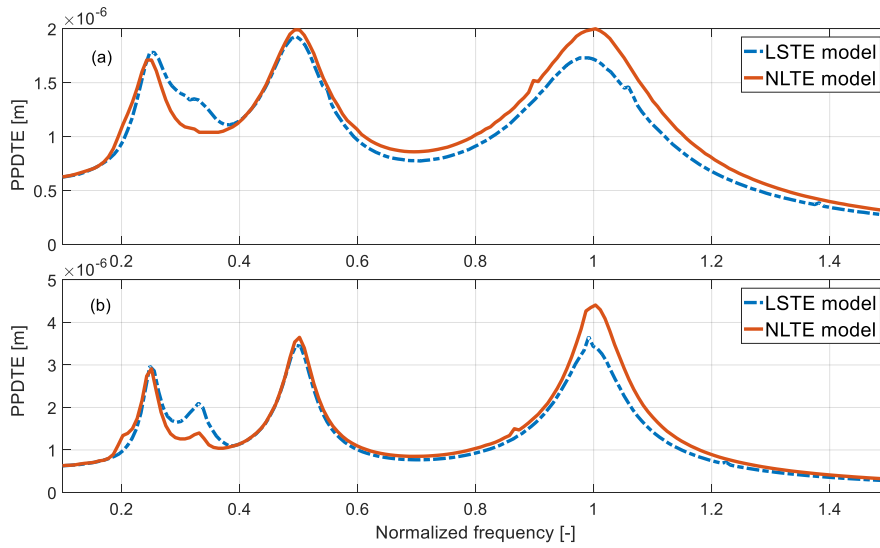


Figure 5-2 Model comparison for a) $\zeta=0.1$ and b) $\zeta=0.05$

Although some minor discrepancies are observed between the results obtained by two models, recalling that these differences are observed only at a very extreme case where LSTE variation is minimum. It is concluded that results match well enough to safely continue with the constant mesh stiffness model in optimization studies, which makes it possible to use a MDOF model for the dynamic analysis of a gear-shaft-bearing system in frequency domain.

Along with the SDOF model, a MDOF gear dynamics model which is based on the approximation proposed by Özgüven and Houser [61] is used while performing optimization studies. The model takes into account the shaft and bearing dynamics, onto which the gear pair is mounted. This model is a linear version of the model developed by Maliha et al. [62]. Nonlinear effects due to backlash are not included in the model.

For the finite element modeling of the shafts, the axial motions are assumed to be negligible; hence, each node in the finite element model of the shaft will have five

degrees of freedom (DOFs), i.e. 2 translational and 3 rotational DOFs. The flexible bearings are modeled in terms of radial stiffness and damping elements.

The gear pair is modeled by two disks, representing the inertia of the gears, which are connected to each other by a linear spring and a damper that represents the gear mesh. The system is excited by the displacement excitation represented by the LSTE. Further details of the model can be found in the study of Maliha et al. [62].

In both SDOF and MDOF models, the profile modification is represented by Fourier series with 5-harmonics which are found to be sufficient. The average mesh stiffness and the harmonics of LSTE, which are the necessary input parameters, are supplied to the dynamic model by using the computer code STEP (Spur Gear Transmission Error Program) developed at the Ohio State University. A MATLAB code is developed in order to perform the dynamic analysis and optimizations required in this study.

Next, the differences between the responses, in terms of PPDTE, obtained by using SDOF and MDOF models are presented for two different configurations. In the first configuration, the gear pair is mounted on relatively short (hence more rigid in transverse direction) shafts; whereas, for the second configuration, the same gears are mounted on longer shafts. The second configuration is shown in Figure 5-3.

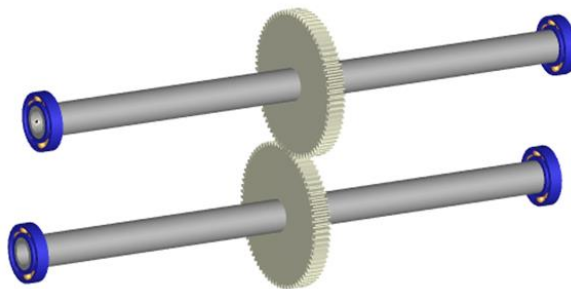


Figure 5-3 Second MDOF model configuration

Details of the gear-shaft- bearing systems under consideration are given in Table 5-2. It should be noted that all other properties except lengths of the shafts used in both configurations are identical and the bearings used at the ends of the shafts have the same stiffness and damping properties.

Table 5-2 Characteristics of the dynamic system

Gears	
Number of teeth	75
Module	3.2 mm
Equivalent mass	2.47 kg
Base diameter	232 mm
Face width	30 mm
Shafts	
Outer radius	55 mm
Inner radius	40 mm
Density	7800 kg/m ³
Elastic Modulus	206 GPa
Length of short shafts	0.1 m
Length of long shafts	1 m
Bearings	
Stiffness	1x10 ¹² N/m
Damping coefficient	1x10 ⁵ Ns/m

In the first example, gears are placed in the middle of the shafts that are 0.1 m long. The response of the system (DTE) for an arbitrary torque and profile modification in a wide speed range is shown in Figure 5-4. Note that w_{norm} is the normalized shaft speed where the normalization is with respect to the natural frequency of the

SDOF model. Investigating the figure, it can be clearly seen that responses of the SDOF model and the MDOF model are very close to each other due to the rigidity of the shafts considered. Therefore, it is expected that optimization studies carried out by using either of the models (SDOF or MDOF models), for this particular case, will lead to similar results.

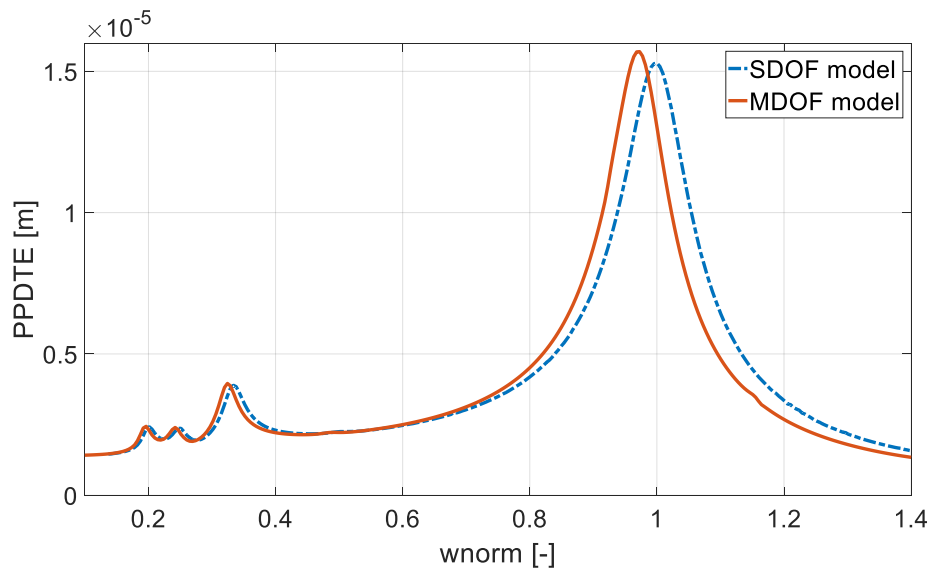


Figure 5-4 Response of MDOF and SDOF models for “short shafts” case

In the second case, gears are placed in the middle of 1 m long shafts. Figure 5-5 shows that, in this case, the shaft flexibility affects the total response of the gear pair considerably, and therefore SDOF and MDOF models yield considerably different results, as expected.

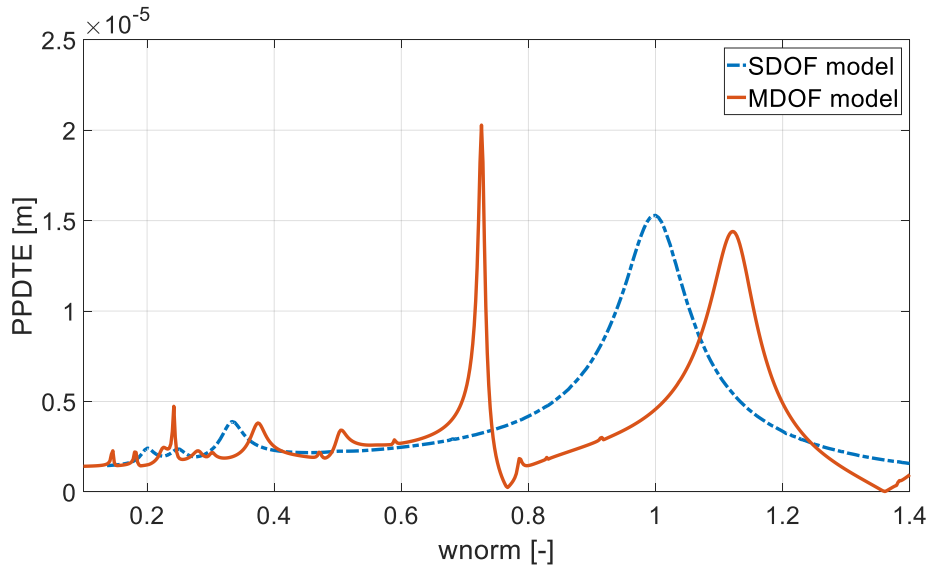


Figure 5-5 Response of MDOF and SDOF models for “long shafts” case

Figure 5-5 reveals that the coupled transverse-rotational modes along with the multi-harmonic LSTE input make the dynamic response more complex compared to the case of short shafts. In case those modes fall in the operating speed range, optimization using a SDOF or a MDOF dynamic model can make a significant difference. Note that this figure corresponds to an arbitrary torque and profile modification case, i.e. one may even find more differences between the results obtained with SDOF and MDOF models depending on the configuration and the relative values of system parameters.

Then, optimization is carried out by using both of the dynamic models, and optimum values obtained are compared. Optimum profiles obtained by using DTE optimization are also compared with those calculated by using LSTE optimization. The objective of the optimization is set as the minimization of the maximum amount of peak-to-peak transmission error. The reason for such an objective function is to decrease the maximum value of the dynamic force at the gear mesh, which has the most dominant effect on the fatigue life of a gear pair. The only parameter to be

optimized is selected as the amount of the linear tip relief. The starting positions of the modifications, which are applied to both gears, are fixed at the highest point of single tooth contact.

Since a single-parameter optimization study is carried out, a brute-force optimization technique is applied because of the respectively lower computational cost. For the whole set of possible profile modifications, a solution is performed at each point in the given parameter domain which is characterized by certain speed and torque ranges. The maximum of PPDTE value is thereafter extracted from the obtained responses for the respective profile modification and compared with the others. The profile modification which leads to the minimum of the maximum PPDTE is labeled as the optimum profile modification. Note that when LSTE optimization is made, only a single torque range is considered and the objective function is taken as the minimization of the maximum peak to peak LSTE.

Since the responses of SDOF and MDOF models differ significantly from each other for longer shaft case, in the rest of this study, optimization is performed for only the long shafts configuration.

Some example cases are presented in order to show the differences between the optimization results obtained from different models. The details of the example cases can be found in Table 5-3. Note that in all cases, the design torque is taken as 1000 Nm.

Table 5-3 Details of the example cases

Case 1	
Torque range	50-100% of design torque
Speed range	2200-2400 rpm
Initial modification	3 μm
Modification increment	5 μm
Case 2	
Torque range	0-50% of design torque
Speed range	1600-1800 rpm
Initial modification	0 μm
Modification increment	5 μm
Case 3	
Torque range	20-40% of design torque
Speed range	1600-1800 rpm
Initial modification	2 μm
Modification increment	2 μm
Case 4	
Torque range	80-100% of design torque
Speed range	1000-1200 rpm
Initial modification	10 μm
Modification increment	2 μm
Case 5	
Torque range	0-20% of design torque
Speed range	600-800 rpm
Initial modification	0 μm
Modification increment	2 μm

For the first two cases, where optimization in a wide torque range is considered, the comparisons are made between the optimization results obtained through the static, SDOF-dynamic and MDOF-dynamic models. The results (normalized with respect to the minimum of the maximum PPDTE obtained) for these cases are presented in Figure 5-6.

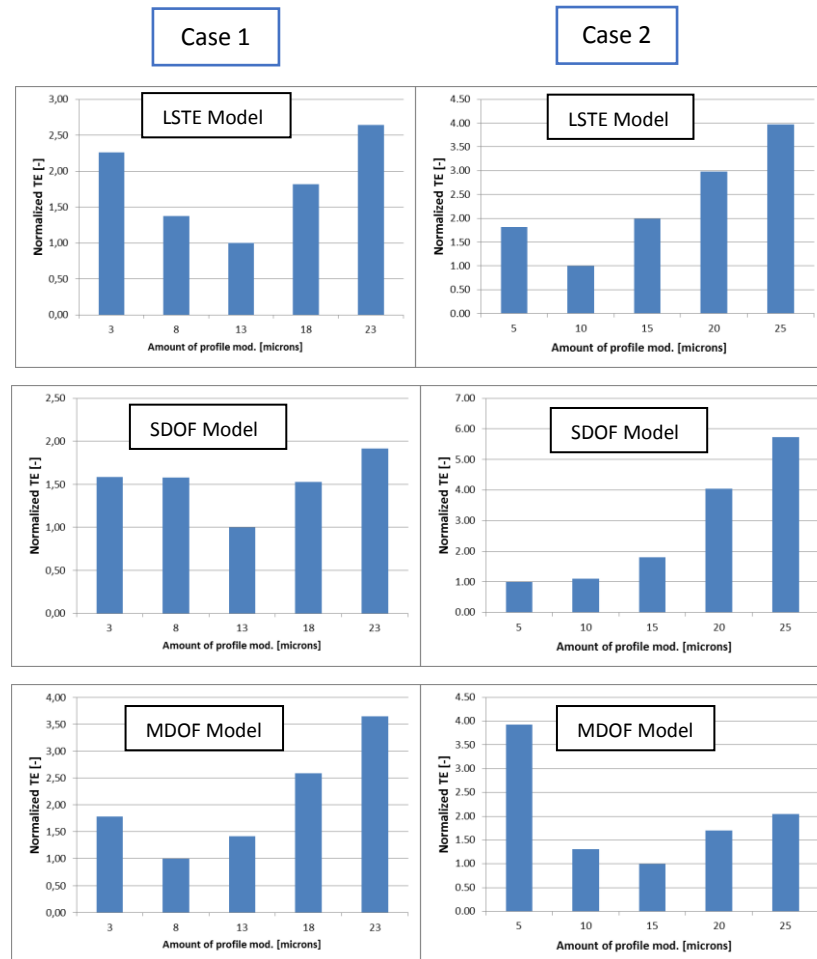


Figure 5-6 Sample optimization results for Case 1 and Case 2

It is observed from the results obtained that, for Case 1, while the SDOF model proposes the 3rd modification (i.e. 13 μm) as the optimum one, which is also proposed by the LSTE model, the MDOF model suggests that the minimum DTE is obtained when the second modification (i.e. 8 μm) is applied to the gear teeth. In

Case 2, the difference between the optimum profile modifications proposed by the SDOF model (5 μm) and MDOF model (15 μm) is as large as 10 μm . The differences between LSTE based optimization and DTE based optimization are also clearly observable for Case 2, which are in agreement with the findings of the study of Faggioni et.al. [50].

In Case 3-Case 5, torque ranges considered in the optimization are limited to 20% of the design torque. The increment of profile modification is kept as low as 2 μm , in order to observe if discrepancies still exist between the results of different models even under such minor modification differences. For these cases, only the comparison of the optimization results between SDOF and MDOF models are considered and the results are given in Figure 5-7.

In this case study, the torque range considered is smaller compared to that of the previous case study; hence, the optimum profile modifications obtained from the SDOF and MDOF models are slightly different from each other. The comparison of the results obtained by using SDOF and MDOF models for the same gear system indicates that those differences can be more important under the influence of operational conditions. Case 3 can be used to explain the differences. MDOF model suggests that, considering wear on the gears, the first modification (2 μm) can be preferred instead of the second modification (4 μm), which is the optimum one, since DTE increases significantly if due to tooth wear profile modification reaches to 6 μm . However, if SDOF model is used, the 3rd modification (6 μm), which is the optimum one, can be used, since the increase, as well as the rate of increase in DTE is small even wear occurs.

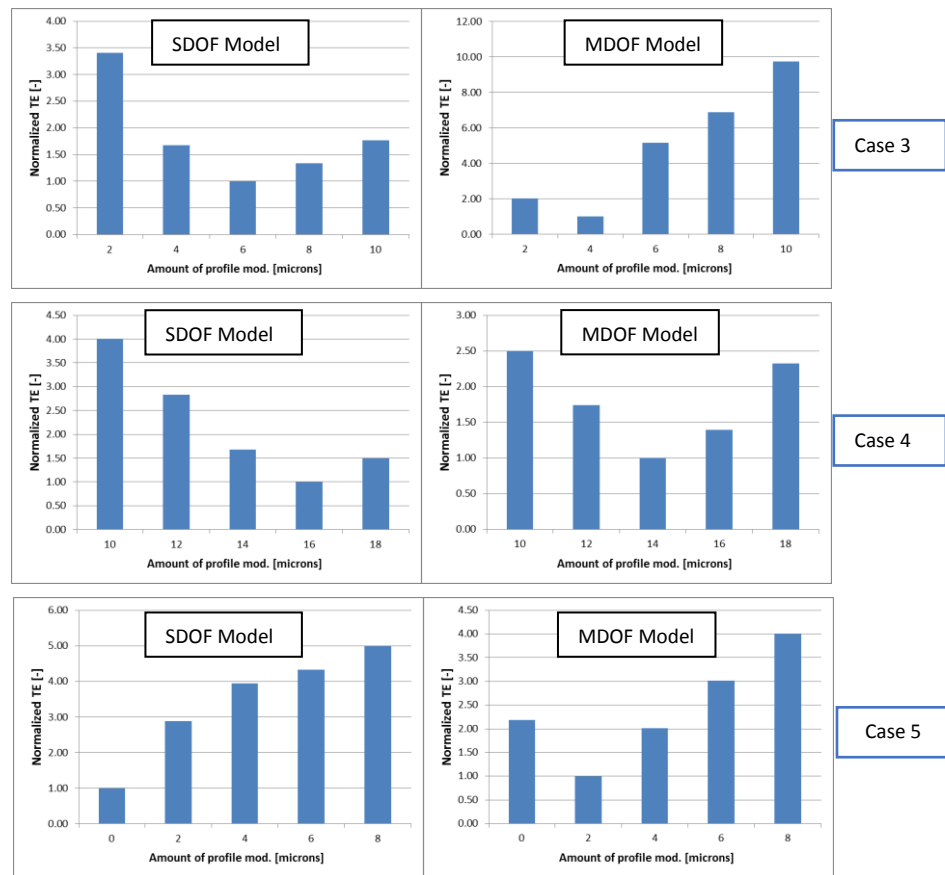


Figure 5-7 Sample optimization results for Case 3, Case 4 and Case 5

5.3 Optimization of Tooth Bending Fatigue Characteristics using TPMs

In this section, a tooth bending fatigue life estimation procedure which is based on gear dynamics will be presented. A single-degree of freedom model is preferred in this study for its simplicity, although such a model will be insufficient for the cases where the compliances of the other elements of the drive system cannot be neglected. The procedure will be explained in detail with an example spur gear pair which is made of high strength alloy steel 42CrMo6. A tooth profile optimization study will be performed in which the aim is to achieve the maximum tooth bending life for the example gear pair, taking the operational spectrum into account. Tooth

root stress cycles will be calculated based on a SDoF nonlinear gear dynamics model using rainflow counting method. Those stress values will be input to the fatigue model which is based on the S/N curve of the gear pair material.

The LSTE-based dynamic model will be used to obtain dynamic root stresses, resulting from dynamic mesh forces. The equation for dynamic mesh force (in case of no tooth separation) is given in [61] as follows:

$$W(t) = W_0 + k_{ave} (x(t) - x_s(t)) + 2\zeta \sqrt{m_e k_{ave}} \dot{x}(t) \quad (5.3)$$

Here W_0 is the static load. Along with the LSTE and average mesh stiffness input, the moment arm (with respect to root of the gears) information is also gathered from STEP, enabling to obtain stress numbers, which are simply the multiplication of mesh forces with the respective moment arms. The real stress values are obtained through a correlation of stress numbers with the static stress results obtained through WindowsLDP of OSU, which is capable of employing finite element formulation for the calculation of root stresses. With this approach, it is aimed to achieve as realistic a stress calculation as possible.

The dynamic root stress data is then directed to the rainflow counting algorithm, in order to extract stress cycle information, which, along with the rpm and duration of the operating condition data, is used in life estimation analysis.

Gears in most applications are subject to relatively low stress levels, so that in comparison to crack propagation period, most of the fatigue life is spent in the crack initiation phase. Therefore, the stress-life (S-N) approach can be considered as an appropriate method of predicting bending fatigue life of gears.

Although in a traditional S-N curve, it is assumed that below a certain level of stress (endurance limit), no fatigue damage occurs, existence of such a limit is widely questioned for most of the engineering materials, including the steels used in gearing industry. For this reason, a two-slope S-N curve [63] is used to capture the damage in regions both above and below the fatigue limit separately.

Following equations can be used for stress values above and below the fatigue limit respectively:

$$\begin{aligned}
 N_i &= N_{FL} \left(\frac{\Delta\sigma}{\Delta\sigma_{FL}} \right)^{\frac{1}{b}}, & \Delta\sigma > \Delta\sigma_{FL} \\
 N_i &= N_{FL} \left(\frac{\Delta\sigma}{\Delta\sigma_{FL}} \right)^{\frac{2}{b+1}}, & \Delta\sigma < \Delta\sigma_{FL}
 \end{aligned}
 \tag{5.4}$$

In these equations, N_{FL} stands for the number of cycles at the endurance limit $\Delta\sigma_{FL}$, $\Delta\sigma$ is the applied stress level and b is the slope of the S-N curve in the region where the stresses are above the endurance limit, in log-log scale. These are the general S-N curve equations which can be employed to many engineering materials, including steel, with the constants varying for each different material. In this study, 42CrMo6 is selected as the gear material and the required parameters are taken from [64]. Table 5-4 shows these parameters.

Table 5-4 S-N Curve Properties for 42CrMo6

Material	$\Delta\sigma_{FL}$	N_{FL}	b
42CrMo6	550	3e6	-0.0816

Rainflow ranges have been widely used for estimating fatigue damage from variable amplitude loading. Rainflow cycle counting method is based on the analogy of raindrops falling on a pagoda roof and running down the edges of the roof. As per the SAE and the ASTM standards, the three-point cycle counting rule uses three consecutive points in a load-time history to determine whether a cycle is formed. Details of rainflow counting algorithm used in this study can be found in [65].

For this study, the stress-time history data is run through a three-point rainflow cycle counting algorithm and stress cycles are extracted. Respective damage for the operating duty cycle under consideration is then calculated using the material S/N curve by implementation of Miner's rule for damage accumulation.

The procedure proposed in this study for estimating the tooth bending fatigue life for a spur gear pair is a combination of the previously mentioned gear dynamics model and the fatigue model. This procedure is shown in Figure 5-8.

The procedure is explained below in detail for a sample spur gear pair with a defined duty cycle. The tooth bending fatigue life is going to be estimated for the following gear pair (Table 5-5). The gear pair under consideration consists of 2 identical spur gears. Tooth profiles are unmodified. The damping ratio is taken as 0.05 since it is used in many gear dynamics modeling studies including [61].

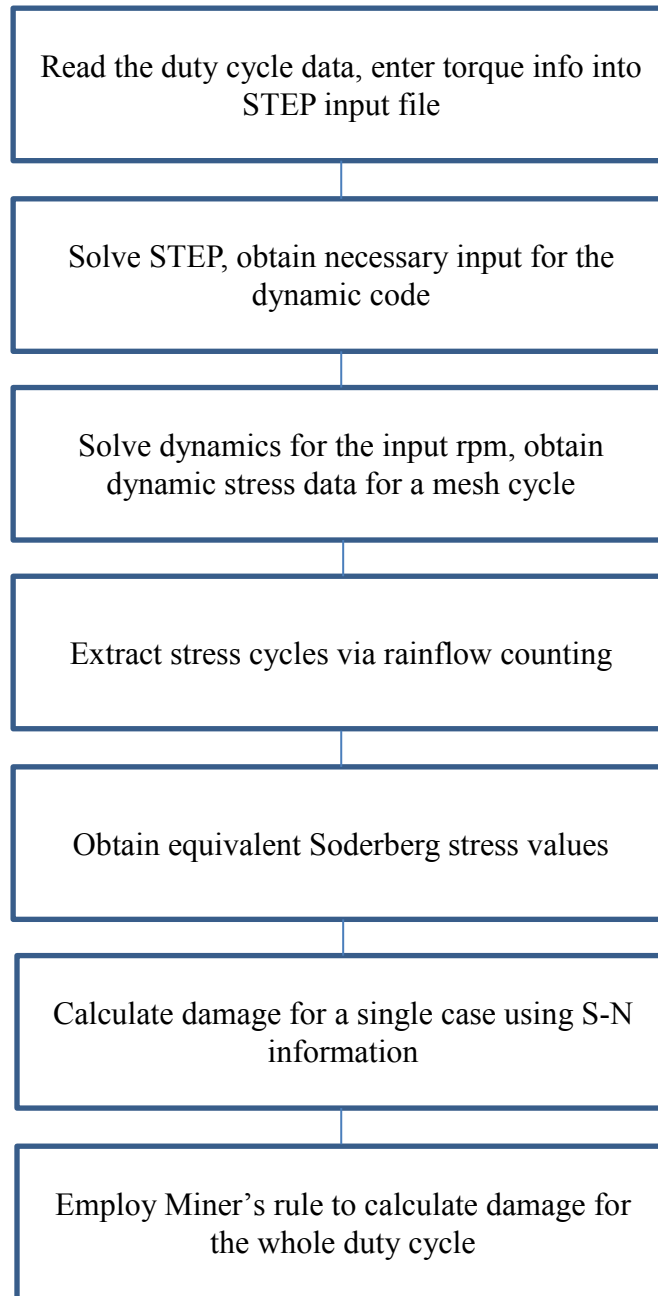


Figure 5-8 Procedure for gear tooth bending life estimation

Table 5-5 Example spur gear pair

Number of teeth	50
Module	3 mm
Equivalent mass	0.7824 kg
Base diameter	140.95 mm
Tip diameter	153.74 mm
Center distance	150 mm
Damping ratio	0.05

When the operating speeds are near the natural frequency of the gear pair system, or correspond to those levels at which the system can be excited by the higher harmonics of the excitation due to the LSTE, the dynamic effects can become dominant and hence a dynamic response analysis becomes a necessity. The tooth bending life of this spur gear pair is going to be estimated for the given duty cycle (Table 5-6). Note that the duty-cycle given in Table 5-6 may as well be interpreted as a portion of a total duty cycle which only contains the critical intervals regarding the fatigue life.

Table 5-6 Duty cycle under consideration

Case	Torque [Nm]	Speed [rpm]	Duration [hours]
1	550	1160	400
2	600	1240	40
3	730	940	80
4	600	1140	200
5	600	1850	20

The steady state normal tooth bending stress results for the different cases of the duty cycle are shown in Figure 5-9. The assumption of a uniaxial stress state is reasonable because of the geometry and the loading characteristic of a spur gear. The static case when a torque of 600Nm is applied is also given for comparison as Case 0.

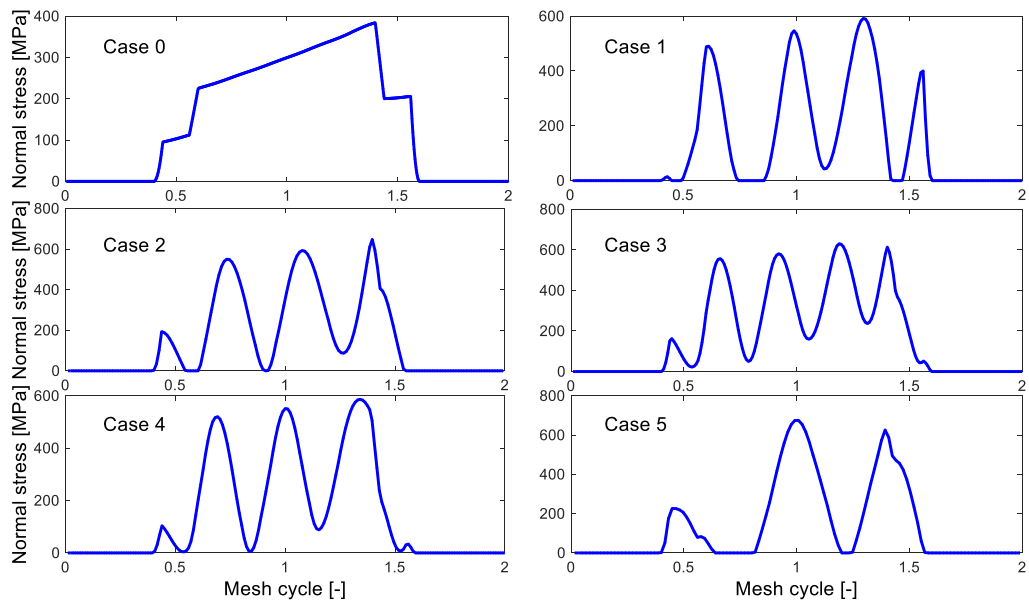


Figure 5-9 Tooth root normal stress results

As expected, the dynamic stress results show a more complex behavior than that of the static case. Not only the peak stress levels go higher, but also the number of stress cycles which can be effective in damaging of the teeth increases. One can also observe the loss of contact phenomenon in Case 1 and Case 5, where the root stress levels drop to 0. The stress cycles are extracted with the Rainflow counting method. Table 5-7 shows the stress cycles for Case 3. Note that here the minor cycles (i.e. cycles with very low stress ranges) are not shown.

Table 5-7 Rainflow stress cycles for Case 3

No. of cycles	From [MPa]	To [MPa]	Range [MPa]	Mean [MPa]	Equivalent Soderberg Stress [MPa]
1	237	613	376	425	359
1	556	50	506	303	383
1	580	160	420	370	359
1	629	0	629	314.5	486

The last column in Table 5-7 shows the equivalent Soderberg stress values. The following operation is used in order to compensate for the tensile mean stress effects on high-cycle fatigue strength. Note that other stress correction methods can also be employed at this step.

$$S_{ar} = \frac{S_a}{1 - \frac{S_m}{S_y}} \quad (5.5)$$

In this equation S_{ar} is the fully-reversed stress amplitude, S_a is the stress amplitude, S_m is the mean stress level and S_y is the yield strength of the material. The Soderberg stress values are entered into the S/N curve equation along with the rpm and duration information in order to check if the gear pair can survive in the projected lifetime. Table 5-8 shows the damages related to the respective cases.

Table 5-8 Fatigue live summary for the gear pair

Case	Cycles	Cycles to fail	Damage [%]
1	2.78e7	5.00e8	5.5
2	2.98e6	1.94e7	15.4
3	4.51e6	5.52e7	8.2
4	1.37e7	6.66e8	2.1
5	2.22e6	3.96e6	56.1
Total	-	-	87.3

Although a direct comparison with the fatigue calculation concept in AGMA standard is not possible, it is safe to say that AGMA does not consider the mentioned effect of secondary stress cycles due to dynamic effects. AGMA considers the cyclic nature of loading in the factor Y_N , stress cycle factor for bending strength [66]. However calculation of this factor does not take into account the possibility of having more than one stress cycle during a single mesh cycle, as the formula for the number of stress cycles (N) is given as:

$$N = 60Lnq \quad (5.6)$$

Here L is life in hours, n is rpm and q is number of contacts per revolution. AGMA gives several S/N charts for finding Y_N , which is used in calculating an allowable bending stress number.

AGMA also employs a dynamic factor, K_v , in order to account for the dynamic loading. Studies [67] have shown that deviations from optimal profile modifications often exceed the AGMA recommendations of dynamic factor for gears with non-optimal modification. With this information, one can modify the dynamic factor to be used by using a gear-dynamics model. However even this updated factor may not

be enough to cover all the dynamic effects in a fatigue calculation. Consider the case shown in Figure 5-10 obtained at 620 Nm torque at 1155 rpm:

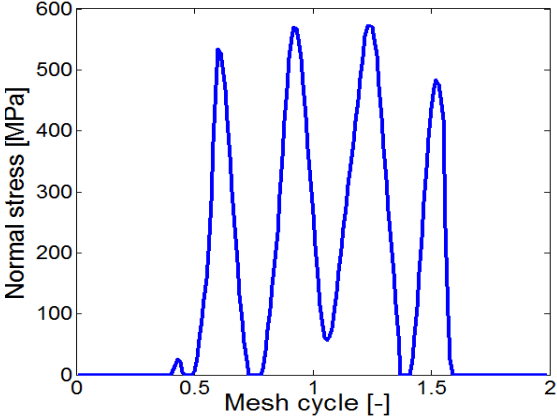


Figure 5-10 Stress cycle information for the sample case

Note that the gear pair is the same gear pair that was investigated in the previous section. Table 5-9 gives the expected fatigue damage information for this case, using the S/N curve for 42CrMo6. The number of cycles to fail is highlighted for the peak stress and for the total stress time history.

Table 5-9 Cycles to fail for the respective stress cycles

Stress cycle	Equivalent Soderberg Stress [MPa]	# of cycles to fail
1	331	4.61e11
2	382	1.59e10
3	396	6.80e9
4	422	1.52e9
Total mesh cycle		1.15e9

It can be clearly observed from Table 5-9 that the omission of stress cycles with smaller ranges (secondary stress cycles) can lead to a miscalculation regarding the lifetime of the gear pair. One should also consider that there may be even cases which are more critical in terms of fatigue damage estimations than the case shown in this example. The fatigue properties of the material and the severity of the loading usually determine the level of the effect of the secondary stress cycles.

Although in most applications gear designers can end up with safe designs by using the conventional dynamic factor and stress cycle factor approach, it should be kept in mind that for some specific speed and torque levels, the secondary stress cycles can also affect the tooth bending life of the gear pair.

Tooth profile modifications are known to be very effective in reducing the vibration and noise in spur gears, since, when properly applied, they reduce the dynamic excitation to the geared system, in terms of loaded static transmission error (LSTE). This mentioned reduction of the dynamic loading of the system also means an improvement in both bending and contact fatigue lives.

There have been many studies, both theoretical and experimental, showing the improvement in dynamic load factors after the employment of proper profile modifications [67,68].

In this study an optimization scheme which, instead of obtaining minimum dynamic load factors, is directly targeted at obtaining the maximum tooth bending fatigue life for a spur gear pair is suggested. Studies [50] have shown that DTE minimization based optimization work can lead to better results than those based on LSTE minimization, so a similar approach is followed here regarding the tooth bending fatigue lives. A comparison with LSTE optimization is not in the scope of this work.

A 4-parameter optimization model is used here, the variables being amount of tip modification and the start of the modification both for the pinion and the gear. A brute-force optimization technique is employed. The gear pair used in the optimization model is the same as the one used throughout Section 6.3. The optimization scheme can be applied on different duty cycles; here an example is given for the duty cycle in Table 5-6.

Table 5-10 shows the results of the optimization study for various arbitrary profile modification scenarios, including the optimum one for tooth bending fatigue life. Note that a case with a life estimation which is worse than the no profile modification case is also shown.

Table 5-10 Damage summaries obtained for different parameter configurations

Profile Modification (PM)	Pinion PM Amount [μm]	Pinion PM Start [°RA]	Gear PM Amount [μm]	Gear PM Start [°RA]	Damage [%]
No PM	-	-	-	-	87.3
1	25	24.6	25	24.3	42.7
2	28	24	25	24.6	1.0
3	31	24.6	28	24	14.8
4	31	24.6	31	24	4.6
5	28	24.6	31	24.6	271.7
Best PM	28	24	31	24	0.0012

As can be observed from Table 5-10, when combined with the nature of the fatigue characteristics for the steel, an optimum profile modification can easily guarantee the safe operation of a spur gear pair throughout its lifecycle, when tooth bending fatigue is the only concern. Another important outcome of this study is that, a bad selection for the profile modification can endanger the gear pair, making a premature

failure possible such that even an unmodified gear pair behaves better, considering tooth bending fatigue. Small variations in the optimization parameters tend to change the fatigue characteristics very dramatically, which underlines the importance of selection of the objective function as maximization of fatigue life, instead of the minimization of LSTE.

The steady state stress cycle information for the duty cycle given in Table 5-6 is shown in Figure 5-11 for the optimum tooth profile modification case.

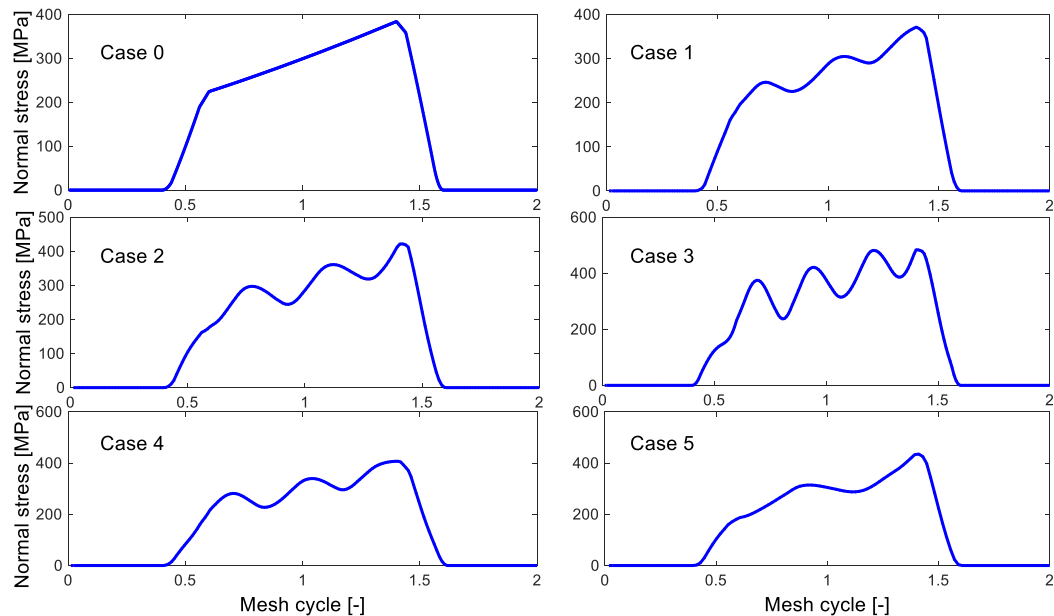


Figure 5-11 Tooth root normal stress time histories for the optimal TPM configuration

With the application of the optimal profile modification, not only the stress-based dynamic factors reduce, but also the secondary stress cycles decrease to such levels that they can be neglected in bending fatigue life calculations. Therefore in terms of improving the tooth bending fatigue life, the effect of a good tooth profile modification is not limited to reduction of the maximum stress at the root region.

5.4 Summary and Conclusion

For the studies performed within the scope of this section, initially, tooth profile modification optimization is performed using 3 different models. The first model is based on the minimization of LSTE variation. In the second and third models, profile modification optimization is achieved through minimization of DTE variation. The second model considers only the spur gear pair dynamics, whereas the third one, which is a MDOF model, takes also the effects of shaft and bearing dynamics into account. The differences between the optimization results obtained by using the mentioned models are studied.

For the second and third models, which consider the dynamics of the respective systems, gear pair dynamics is modeled based on a previous study by Özgüven and Houser [61]. The mentioned model employs the approximation of using an average value for gear mesh stiffness and includes the excitation effect of mesh stiffness variation through a displacement excitation function in the form of LSTE. This model is preferred in this study, since it can be easily implemented to a MDOF model, providing solutions in frequency domain. In order to verify the accuracy of the model for the cases where optimum profile modifications are used and therefore very small LSTE variations are observed, first a comparison is made between DTEs obtained through this model and an exact gear dynamics model, which employs time-variant mesh stiffness. The comparison revealed that the invariant mesh stiffness approximation can also be used in the dynamic analysis of gear pairs where LSTE excitation is at very low levels.

Before proceeding with optimization, possible different outcomes of using SDOF and MDOF models are investigated on two different cases. The first case with shorter shafts represents a relatively rigid configuration of a gear-shaft-bearing

system, whereas the second case is an example of a significantly more compliant system. The results obtained through both models turned out to be very similar for the first case. However, for the second system under consideration, the responses obtained with SDOF and MDOF models are found to be considerably different from each other, as expected. It is shown that when combined with multi-harmonic excitation, the complex dynamic nature of compliant systems resulting from coupled transverse-rotational modes observed in operational speed ranges makes MDOF models more suitable to be used in optimization studies.

In optimization studies, differences are observed between the best profile modifications suggested by LSTE-based model and those obtained by using optimization models based on DTE minimization. This observation is in line with the findings of Faggioni et al. [50]. Therefore, the main emphasis is placed on the comparison of the optimization results obtained from SDOF and MDOF dynamic models in this study. Important differences are observed between the optimum profile modifications obtained by SDOF and MDOF dynamic models for gears on compliant shafts. It is therefore concluded that the optimum tooth profiles obtained by considering only the dynamics of a gear pair may not represent the best tooth profile modification when these gears are on flexible shafts and/or bearings. It is also shown that when parameters such as quality of manufacturing and wear of the gears are of concern, such differences can be even more important. Therefore, it can be said that for compliant systems, neglecting the shaft and bearing dynamics and employing SDOF gear dynamics models may lead to incorrect decisions for determination of the optimum profile modification.

Here it should be noted that for the study of TPMs in spur gears, only the amount of tip relief is taken as a parameter to be optimized. However, when more parameters such as shape of the profile modification (linear, parabolic) and the starting position (in terms of roll angles) of profile modifications are included in the optimization

study, the differences between the results obtained from SDOF-based and MDOF-based optimization models may be even more significant.

In the second part of the TPM studies on spur gears, a procedure to estimate the tooth bending fatigue lives of spur gear pairs is explained. Gear dynamics model is incorporated into the life estimation model in order to get more accurate stress cycles at the actual operating scenarios. This procedure is then employed in a 4-parameter profile modification optimization study where the target is to obtain maximum tooth bending fatigue life for an example spur gear pair with a pre-defined duty cycle.

Gear pair dynamics is modeled based on a previous study by Özgüven and Houser [61]. The mentioned model employs the approximation of using an average value for gear mesh stiffness and includes the effect of mesh stiffness variation through a displacement excitation in the form of LSTE.

The relatively low bending stress levels expected at the root region of spur gears make it appropriate to apply HCF theory for fatigue life estimation. A 2-slope S-N curve is used here in order not to neglect the stresses below the fatigue limit. Soderberg equation is used to take into account the effects of mean tensile stresses. For calculating the accumulation of the damage during a duty cycle, Miner's rule is preferred. It should be noted here that different theories also exist in the literature as alternatives to both the Soderberg equation and the Miner's rule.

The dynamic stress plots show that depending on the operation speed, it is possible to observe that secondary stress cycles are also critical in terms of damaging of the gears when tooth bending fatigue is considered. A 3-point rainflow counting algorithm is employed for detecting the stress cycles during a single gear mesh period.

When a safety analysis is performed for a gear pair, the common approach is to apply certain factors in order to compensate for the dynamic nature of loading and stress cycles. The calculations can further be improved by the replacement of dynamic factors stated in gearing standards (AGMA, ISO, DIN) by more accurate ones based on a dynamic analysis. However the effect of secondary stress cycles can still be neglected with such an approach, misleading to overestimated bending fatigue lives. A more accurate life estimation is possible using the procedure explained in this study.

A proper tip modification design is sought for both of the mating gears by optimizing the modification parameters, i.e. start and magnitude of the tip reliefs. When the overall solution domain is investigated, the sensitivity of the fatigue life estimations turns out to be quite high. With a properly optimized tip relief, it is possible to eliminate the adverse dynamic effects, hence obtain life estimations which practically guarantee a safe operation throughout the whole life cycle of the gear pair. On the other hand, an improper profile modification (even with slightly different parameters) could lead to a premature failure of the gear pair. The stress plots for the best profile modification scenario are also investigated using the example gear pair. It is observed that not only the dynamic stress factors reduce but also the secondary stress cycles disappear.

CHAPTER 6

TOOTH PROFILE MODIFICATIONS FOR IDEAL DYNAMIC

RESPONSE OF PGTS

6.1 Introduction

In this section, profile modification concept in PGTs is addressed. Both linear and parabolic modifications are considered. A purely-torsional mathematical model which is a variant of Ozguven's "Loaded Static Transmission Error (LSTE)" concept for parallel-axis gears [61] is proposed. A comparison of the proposed model is made using the Transmission3D software, which uses a combined analytical contact mechanics - FE approach for geared systems. The profile modifications for PGTs are then investigated on the proposed model, using harmonic balance method (HBM) with arc-length continuation. In a first step the effectivity of TPMs in reducing the dynamic mesh forces are investigated using linear and parabolic TPMs. The sensitivity of dynamic characteristics of a PTG to the design parameters of TPM is also analyzed. Ideal TPMs in terms of reducing PGT vibration are examined for speed intervals where different normal modes dominate the dynamic behavior. Finally the relationship between loaded static transmission error and dynamic mesh displacement is addressed.

6.2 Nonlinear time-variant mathematical model using LSTE

A purely torsional mathematical model is used for all the profile modification studies performed. It is a time-varying stiffness model which also includes backlash

nonlinearity. Eqs. 2.1 - 2.10 provide the equations of motion for the mathematical model used in TPM studies for PGTs.

The distinction of the proposed model lies in how the time-varying stiffness term is calculated. In their study related to correlating dynamic transmission error values to dynamic forces, Tamminana et al. [69] proposed a time-varying nonlinear dynamic model for spur gears where they estimate the time-dependent stiffness parameter as a function of LSTE and an error term. Results of this study show excellent correlation on profile-modified spur gears with both experimental and FE results. This approach can also be used to estimate the mesh stiffness functions of a PGT with profile modifications. Utilizing this method, mesh stiffness variations can be represented as follows,

$$k_{si}(t) = \frac{T_s}{r_s n_p} \cdot \frac{1}{[LSTE_{si}(t) - e_{si}(t)]} \quad (6.1)$$

$$k_{ri}(t) = \frac{T_r}{r_r n_p} \cdot \frac{1}{[LSTE_{ri}(t) - e_{ri}(t)]} \quad (6.2)$$

where profile modifications are included in $e_{si}(t)$ and $e_{ri}(t)$. This method combines the advantages of both LSTE-excitation based models and time-varying stiffness models. By calculating the LSTE term only, since applied TPM is already known, it is possible to include a time-varying stiffness parameter in the related mathematical model with relative ease. This also helps to avoid the disadvantages of constant-stiffness dynamic models, such as accuracy problems especially for nonlinear response and response due to higher harmonics [6].

Firstly, it is required to validate the mathematical model proposed for PGT systems, before using it to study the effects of profile modifications. Although the proposed approach for mesh stiffness approximation has been shown to be accurate for spur

gears, it is still necessary to perform a validation study for the complete model proposed for PGTs, as the use of this mesh stiffness approximation has not been employed before in a planetary gear dynamics model. For this purpose, combined FE-contact mechanics software Transmission3D and its solver Calyx, are used. This software is preferred due to its computational efficiency in solving the non-linear contact problem. In conventional FE tools, this problem requires a very fine mesh of finite elements for an accurate solution. This results in infeasible amount of computation times, especially for dynamic simulations where steady-state analyses are sought. However, Calyx approaches the non-linear contact problem with analytic means [70] and combines the analytical solution of the contact region with FE solution of the rest of the model under consideration. Calyx is widely used as a validation tool in gear dynamics studies where analytic models are employed [18,55,71].

An example PGT is studied for forced response comparisons of proposed analytical model with 3D FE model (Table 6-1). Here torque input is from the sun gear and output member is carrier, whereas the ring gear is fixed. In this case study, a relatively thick ring gear is considered in order to avoid any dynamic effects due to rim elasticity [72]. Profile modifications are applied on the tip and the root regions of the respective gears. The modifications start from HPSTC for tip and from LPSTC for root modifications. The carrier is modeled as a very large inertia compared to other members of PGT, which is the case for PGTs that are commonly employed in main rotor drive systems of helicopters. In most of the helicopters, main rotor shaft, which is connected to the main rotor system, acts as the carrier of the planetary reduction stage. All bearings are modeled as very rigid stiffness elements for a valid comparison with the purely torsional analytical model.

Table 6-1 Example planetary gear set used in analytical model validation

	Sun	Planet	Ring
Number of planets		3	
Number of teeth	36	21	78
Module [mm]		4	
Pressure angle [deg]		21.3	
Effective outside diameter [mm]	150	91	330
Root diameter [mm]	135	76	321
Facewidth [mm]		30	
Transverse tooth thickness [mm]	5.3	6.8	5.3
Diameter at measured tooth thickness	144	84	312
Torque applied [Nm]	1800	-	-
Mesh damping coefficients [Ns/m]	158		164
Profile modification at tip and root [um]	15	0	15.5
Young's modulus [GPa]		206.8	

Figure 6-1 shows the FE model of the PGT under consideration. The FE mesh is kept as coarse as possible for computational speed. Final mesh configuration is obtained by running successive trial simulations with different mesh resolutions which guarantees the accuracy of the solution while keeping the solution time at a minimum.

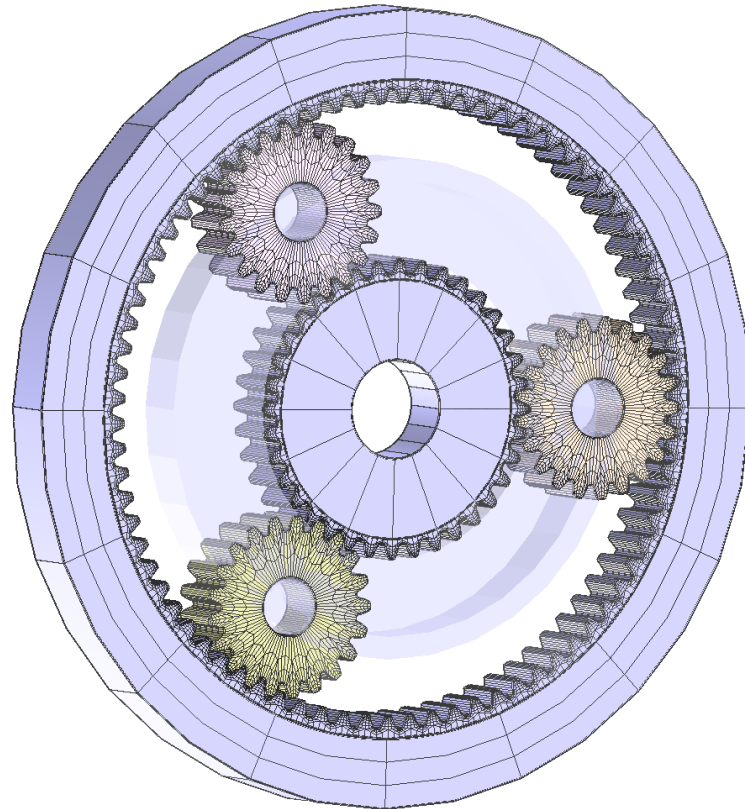


Figure 6-1 A view of the FE model for the example planetary gear train used in validation study

The damping is modeled in Transmission3D as Rayleigh damping, and the corresponding Rayleigh damping coefficients for all gear bodies (sun, planets and ring) are $\alpha = 479 \text{ s}^{-1}$ and $\beta = 1.4\text{e-}7 \text{ s}$. The mesh damping coefficients provided in Table 6-1 are used in time-integration solution of the proposed lumped-parameter model, which represent similar damping characteristics to Transmission3D model. At each speed point, time step is adjusted to represent a mesh cycle by 64 points. Around 3000 time-steps is required in order to reach to the stable solution region.

The analytical model is run in Matlab using ode45 time-integration method which uses Runge-Kutta-Fehlberg method. Time-dependent mesh stiffness parameters

required for analytical model are obtained through Transmission3D, using LSTE data from single-pair solutions of sun-planet and ring-planet meshes.

A speed range which covers third, fourth and fifth superharmonics of the first natural frequency, is selected for this comparison study. Such a speed sweep through a number of harmonics of an initial natural frequency is again a common case for helicopter PGTs during the start-up and slow-down phases of operation. The first natural frequency for such systems is usually much above the operational speed level, which is more or less constant during the flight for most of the helicopters.

A comparison of forced-response results of both models, in terms of rms sun displacement, can be seen in Figure 6-2. Similar to the findings of Tamminana et al. [69] for spur gears, response obtained through the analytical model agrees well with FE solutions.

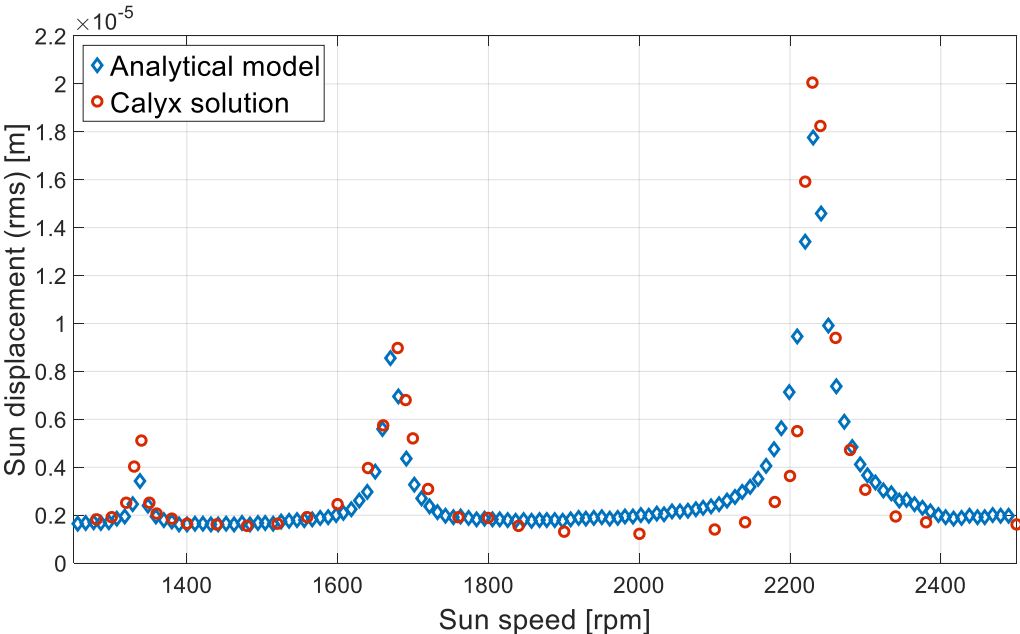


Figure 6-2 Comparison of the frequency response for analytical and FE models

The time histories of sun displacement obtained at 1680 rpm and 2230 rpm are also shown in Figure 6-3. These results also support that developed method agrees well with the commercial Transmission 3D software.

The results of this validation study show that the proposed mathematical model, which requires significantly less computational effort, is appropriate for performing detailed parametric studies regarding TPMs in planetary gear systems. Therefore, using only LSTE data, which contains both the geometric error terms and the static transmission error due to static deflection of the respective gear pairs, it is possible to obtain an accurate estimation of dynamic response of PGTs with TPMs.

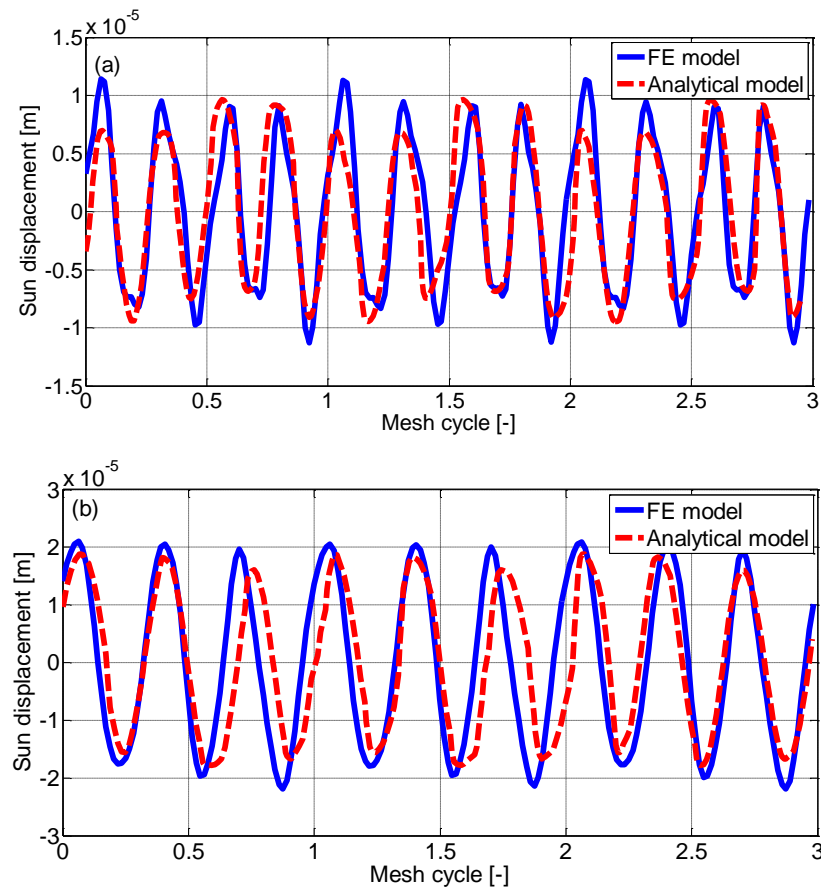


Figure 6-3 Time histories for sun displacement at a) 1680rpm and b) 2230 rpm

Eqs. 2.25 - 2.36, obtained through HBM, are solved using Newton's method with arc-length continuation. Proper TPMs are expected to diminish the vibration levels and eliminate any possible nonlinear effects, but nevertheless arc length continuation is able to show multiple solutions for the speed ranges where nonlinear effects are still dominant.

In order to validate HBM solutions, a comparison study is performed between the numerical integration results and HBM solution, for an example gear set with TPMs. The parameters for this example gear set are given in Table 6-2.

Table 6-2 Example planetary gear set used in HBM vs. time integration comparison

	Sun	Planet	Ring
Number of planets		4	
Number of teeth	38	22	82
Module [mm]		4	
Pressure angle [deg]		21.3	
Effective outside diameter [mm]	158	95	323
Root diameter [mm]	142	80	336
Facewidth [mm]		30	
Transverse tooth thickness [mm]	5.3	6.8	5.3
Diameter at measured tooth thickness	152	88	328
Inertia/r² [kg]	2.42	0.82	10
Torque applied [Nm]	2400	-	-
Profile modification at tip and root [um]	6	6	0
Young's modulus [GPa]		206.8	

In this PGT, the ring gear is fixed and the carrier is modeled as a large inertia. In order to check the validity of the solution with TPMs, gears with different TPMs are considered. In HBM, 6 harmonic terms are used for the representation of the time-dependent parameters. Response comparison in terms of rms sun displacement is given in Figure 6-4.

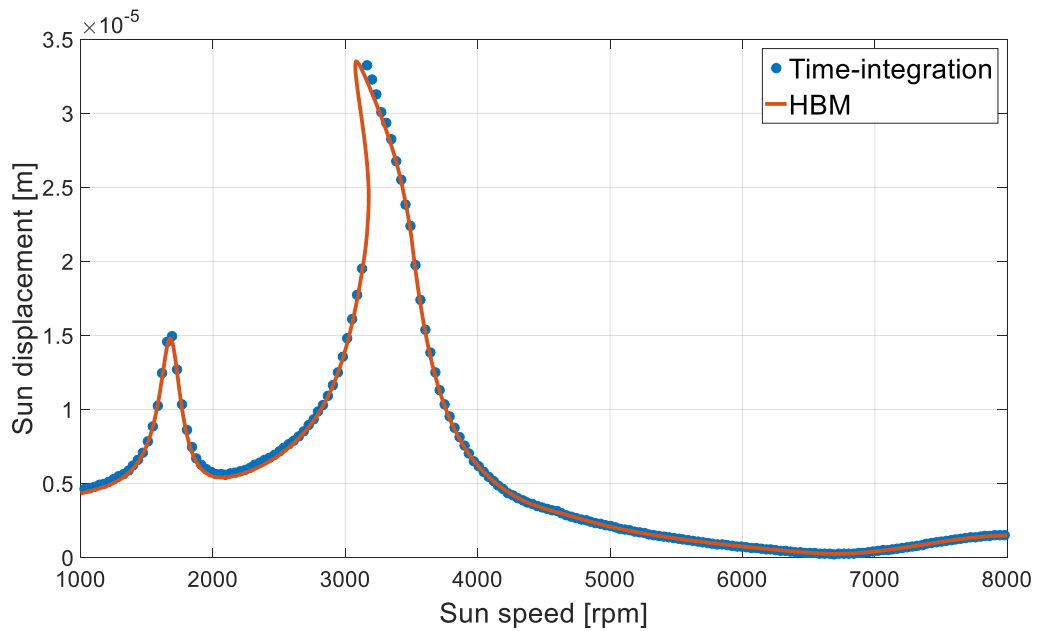


Figure 6-4 Comparison of HBM and time integration response

It is apparent in Figure 6-4 that HBM method agrees well with direct time integration and it is successful in obtaining the steady state response of the PGT under consideration. Therefore, HBM is used in the rest of the study for determining the steady-state response.

6.3 Parametric studies

The dynamic effects of TPMs are extensively studied by running dynamic simulations on the aforementioned PGT dynamics model. The LSTE data is

collected from WindowsLDP software for each simulation, without any approximations (such as a rectangular modeling of LSTE). The PGT configuration outlined in Table 6-2 is used for this study as the basic configuration. For sun-planet gear pairs, the modifications are applied on the tip and root regions of the sun gear teeth. For ring-planet pairs, the modifications are applied on the tip and root regions of the teeth of planet gears. Linear modifications start from HPSTC and LPSTC for tip and root, respectively for both sun-planet and ring-planet pairs. Parabolic modifications start 0.5° prior to HPSTC and LPSTC points for sun-planet pairs and 1.0° prior to HPSTC and LPSTC points for ring-planet pairs (i.e. modifications start just before HPSTC and LPSTC points, slightly in double-contact region). These locations are selected since they result in the least possible variation in LSTE, when a proper amount of modification is applied. Note that the “proper” amount of the respective modification to obtain minimum variation of LSTE is dependent on the level of the applied torque. In all TPM configurations throughout the parametric study, the amount of the applied profile modification is kept the same both for the tip and root regions of the respective gears.

Figure 6-5 shows the ratio of the maximum sun-planet dynamic mesh force to static mesh force for various amounts of TPMs. The simulations are run between sun speed of 1000-6000 rpm for the example gear train considered. It is already known that proper TPMs are able to reduce the dynamic response. However, Figure 6-5 also reveals some other important characteristics of TPMs which can be translated into design guidelines.

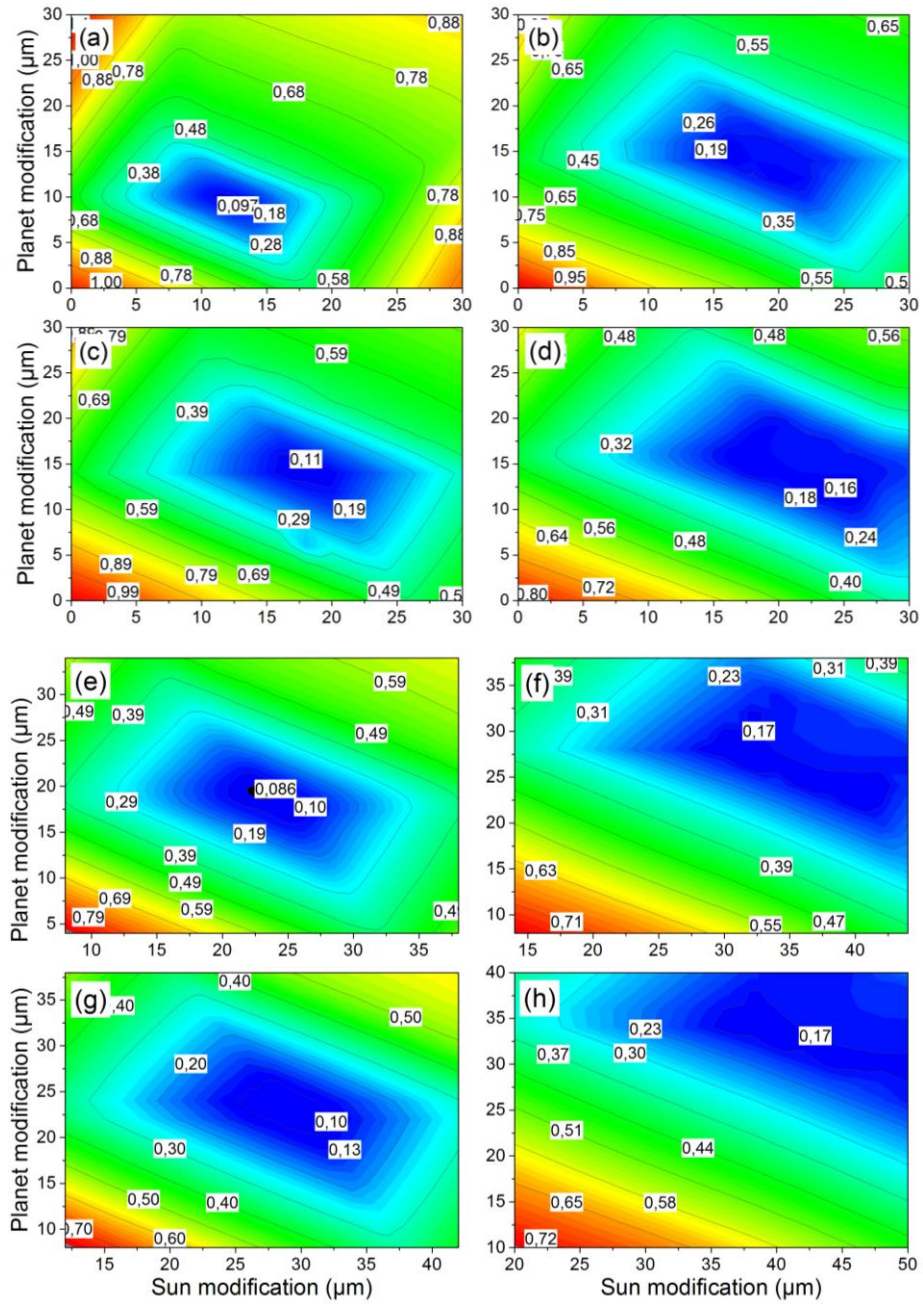


Figure 6-5 Maximum dynamic to static sun-planet mesh force ratios for a) Torque=1600Nm, linear TPM, b) Torque=1600Nm, parabolic TPM, c) Torque=2400Nm, linear TPM, d) Torque=2400Nm, parabolic TPM, e) Torque=3200Nm, linear TPM, f) Torque=3200Nm, parabolic TPM, g) Torque=4000Nm, linear TPM, h) Torque=4000Nm, parabolic TPM.

In order to obtain an ideal response in terms of dynamic mesh forces, depending on the speed range, one should apply TPM on both sun-planet and ring-planet meshes. In all of the simulations, an ideal dynamic force response is obtained via a proper combination of sun-planet and ring-planet modifications, since the sun-planet and ring-planet mesh forces are coupled with each other.

At all load levels, a minimum of the maximum dynamic forces is achieved by applying linear TPMs rather than parabolic ones. However, depending on the criticality of the application, the differences between the minimum values obtained by linear TPMs and parabolic TPMs can be considered to be negligible.

Figure 6-5 also shows that parabolic TPMs are less sensitive to the variation in the amount of TPM. In most of the applications the order of magnitudes for TPMs is in micron-level. Therefore such findings regarding the sensitivity of TPM design parameters are especially important when the manufacturing tolerances and tooth wear are considered. It is also worth noting that as the torque level decreases, the sensitivity of the dynamic forces to the amount of TPM increases.

Figure 6-6 provides the ratios of the maximum dynamic mesh force to static mesh force as functions of sun and planet TPMs, for sun-planet and ring-planet meshes, at two different torque levels. Parabolic TPMs are applied at 1600Nm, whereas linear TPMs are applied at 4000Nm.

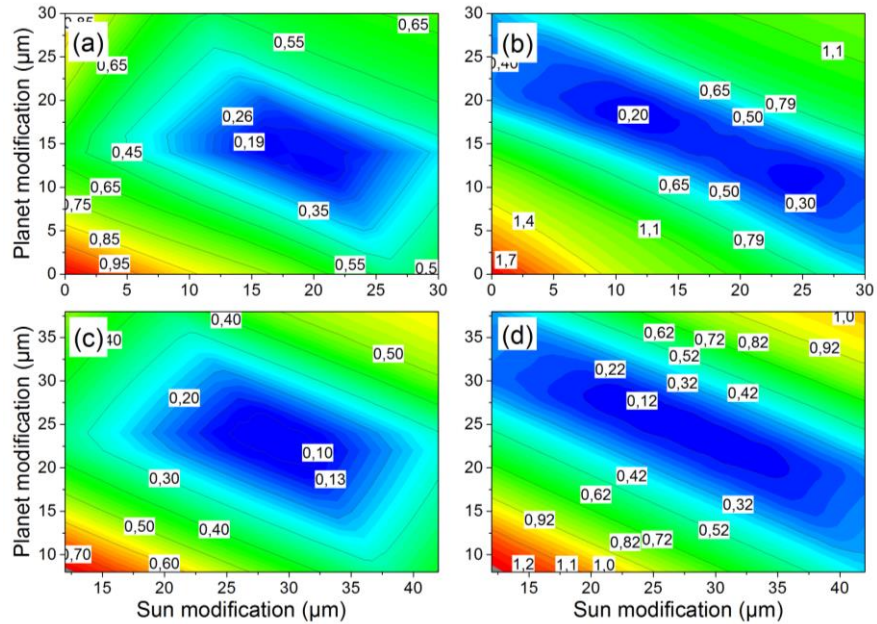


Figure 6-6 Maximum dynamic to static mesh force ratio for a) Torque=1600Nm, parabolic TPM, sun-planet, b) Torque=1600Nm, parabolic TPM, ring-planet, c) Torque=4000Nm, linear TPM, sun-planet, d) Torque=4000Nm, linear TPM, ring-planet

Although sun-planet and ring-planet meshes do not necessarily give the least dynamic forces at the same TPM configuration, it is safe to say that they behave very similarly. It is also evident from Figure 6-6 that the sensitivities of mesh forces to amount of TPM are different for sun-planet and ring-planet meshes.

Effectivity of a TPM design is strongly dependent on the level of loading. It is investigated next how an ideal TPM designed for a specific torque level behaves under different torque levels. Firstly, TPMs which minimize the maximum rms displacement responses for both sun-planet and ring-planet meshes in the speed range of 1000 to 6000rpm are calculated for torque levels in the range 1600-4800Nm, with 800Nm intervals. Then simulations are performed for these TPMs at other torque levels in the defined range. Figure 6-7 shows rms sun-planet (Z_{sp}) and

rms ring-planet (Z_{rp}) displacements obtained as a result of this set of simulations, in a normalized form. The normalized values are obtained by dividing Z_{sp} and Z_{rp} by the respective minimum values $Z_{sp,\min}$ and $Z_{rp,\min}$. Note that 4800Nm is considered as an upper limit in terms of loading, since the tooth bending and contact stresses beyond this level are found to be critical in terms of gear life calculations. Therefore it is defined as the maximum design load, and hence any increased torque level is unrealistic for this particular study.

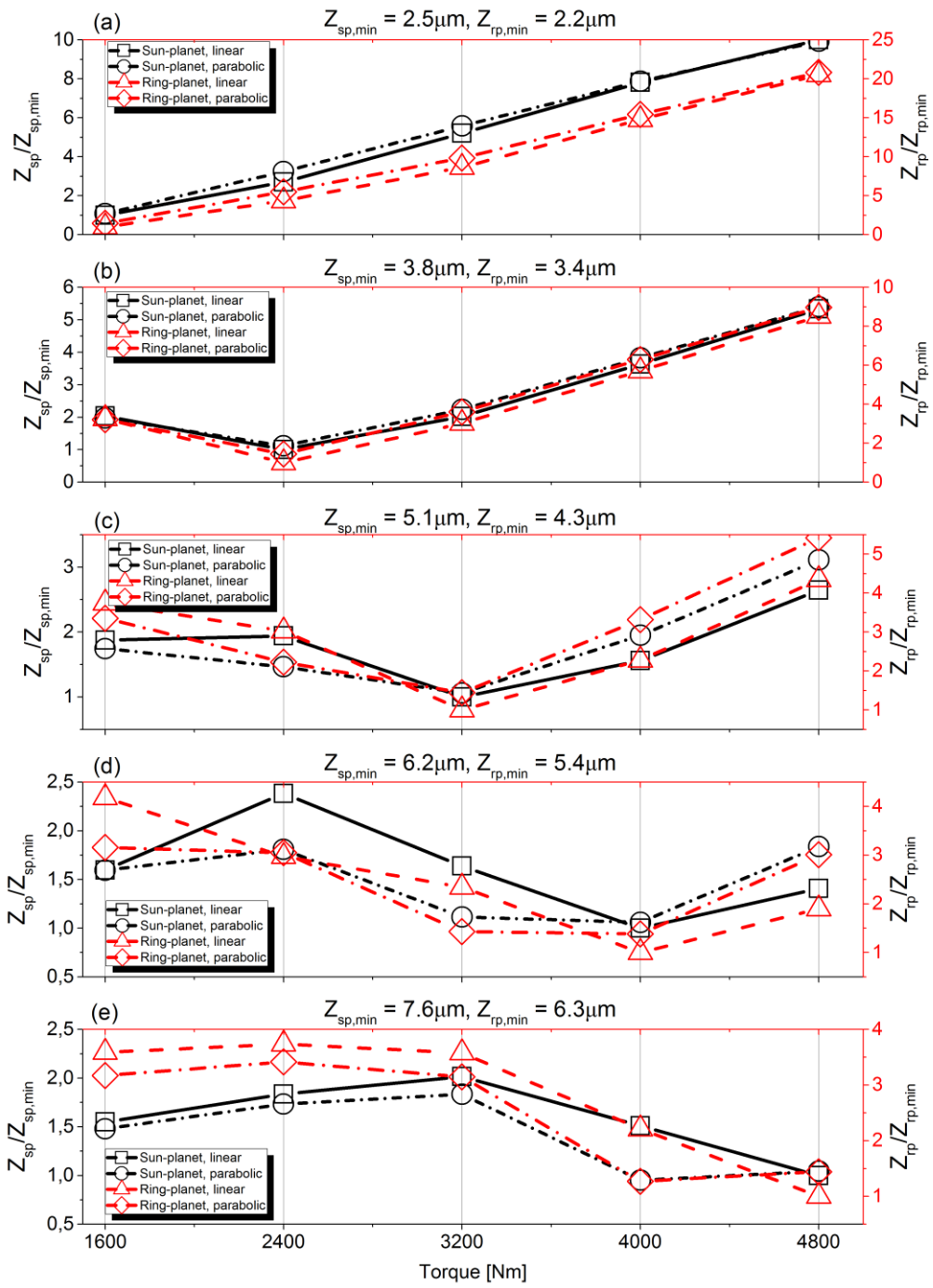


Figure 6-7 Maximum dynamic displacement response for ideal TPMs for a) Torque=1600Nm, b) Torque=2400Nm, c) Torque=3200Nm, d) Torque=4000Nm, e) Torque=4800Nm

Although not shown here, in the torque range under consideration, all of the ideal TPMs resulted in dynamic response which is less than the cases with no TPMs. However, it is also apparent that ideal TPMs for lower torque values (e.g. for 1600Nm) mean a loss of potential for higher torque levels in terms of reducing the dynamic response. With the ideal linear TPM for 1600Nm, obtained sun-planet response at 4800Nm is 25 μ m. However, with the application of optimum TPM for 4800Nm, this value is found to be as low as 7.5 μ m. A similar conclusion can also be reached for the opposite case. If one chooses to apply a linear TPM optimized for 4800Nm, at 1600Nm, the sun-planet displacement response is 10 times the response achieved by using the optimum TPM at that load level (22.5 μ m vs 2.5 μ m).

When lower torque values are considered, optimum parabolic TPMs for a specific torque level result in better dynamic response than their linear counterparts. As an example, ideal parabolic TPMs designed for 4000Nm also resulted in respectively comparable response levels for 3200Nm.

The above conclusions can be useful when an optimization study is performed to determine the optimum TPM for a specified operational spectrum consisting of different load and speed levels and their contributions to the total operational life.

PGTs have distinct torsional natural modes that can only be excited by certain mesh phasing configurations. Kahraman [11] defined these torsional modes as “in-phase” and “sequentially-phased” modes in his study in which he also analytically formulated the natural frequencies associated with these modes. The first and the second “in-phase” modes can only be excited by in-phase excitations; whereas, “sequentially-phased” modes can be excited by sequentially-phased excitations. More information regarding this phenomenon and the rules of mesh phasing in PGTs are available in the literature [32,55,73]. The mode shapes associated with these modes are also different for each natural mode. For in-phase modes, all planets have

identical rotations, while the relative movements between sun-planets and ring-planets may change from one mode to the other. In sequentially-phased modes, the sun and ring gears do not move, whereas the sum of the displacement vectors for planets sum up to 0. These differences in mode shapes are also expected to affect the ideal TPM configurations, which lead to most favorable dynamic behavior of PGTs in terms of vibration and dynamic forces.

Table 6-3 lists the approximate undamped natural frequencies for the example PGT, calculated by the analytical formulation proposed by Kahraman [11] which is based on mean mesh stiffness values for the unmodified teeth. For dynamic simulations with TPM, these values are subject to minor changes due to the effect of TPM on mesh stiffness.

Table 6-3 Natural modes of the example PGT with no TPM

Natural frequency [sun rpm]	Associated mode
6920	First in-phase mode
13940	Sequentially phased modes
16264	Second in-phase mode

Figure 6-8 shows results of three different simulations for the conditions where the applied loading is the same (sun torque of 2400Nm) but the speed ranges differ from each other (2500-6000rpm, 6000-10000rpm and 12000-16000rpm, respectively). In the first speed range, the second harmonic of the first in-phase mode is excited. The excitation of the second harmonic of the second in-phase mode is expected in the second speed range. In the third speed range, the effects of TPM on the sequentially phased mode are investigated. Figure 6-8 shows the outcome of the simulations in terms of the rms sun-planet and ring-planet mesh displacements, for different amounts of linear TPMs.

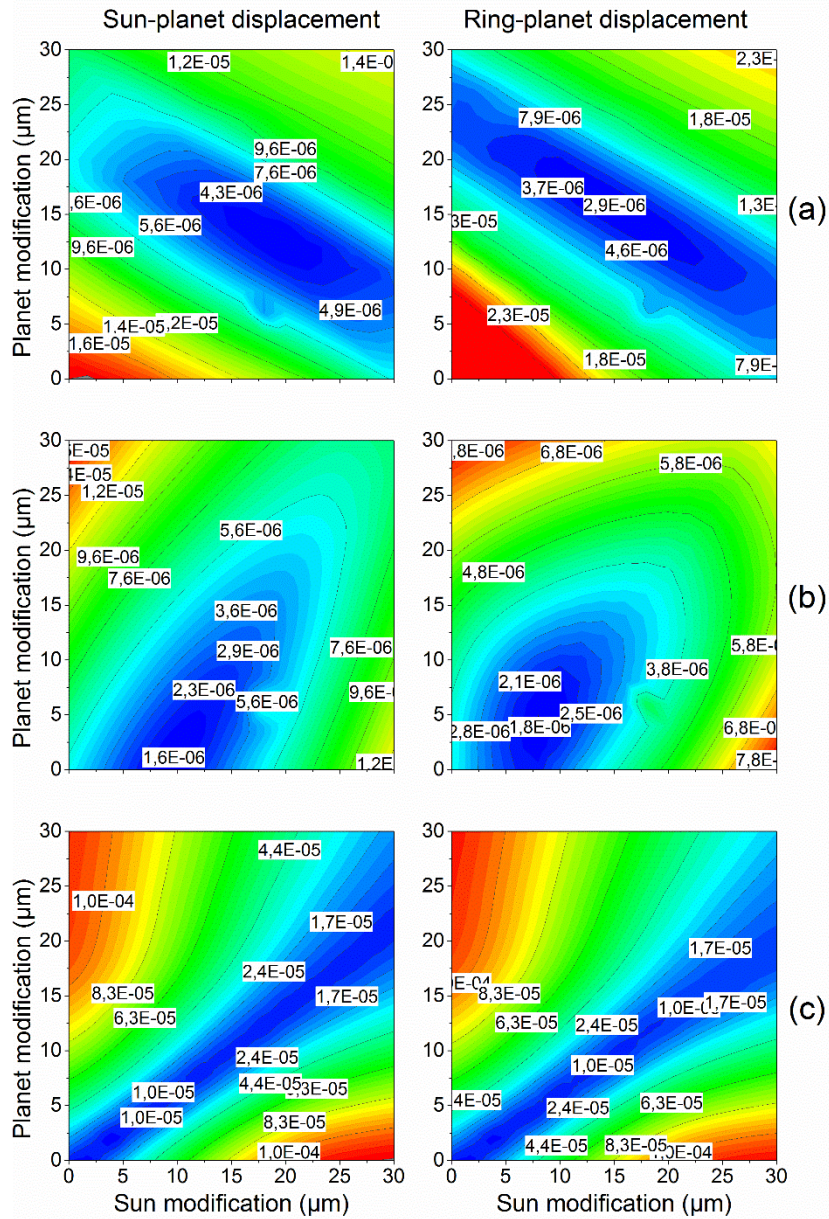


Figure 6-8 Effect of TPMs on rms sun-planet and ring-planet mesh displacements for a) 2500-6000 sun rpm, b) 6000-10000 sun rpm, c) 12000-16000 sun rpm

Outputs of these simulations reveal some important features regarding the design of TPMs for PGTs. Optimum TPMs in terms of minimum rms sun-planet and ring-planet displacement responses differ for each speed interval under consideration for

this case study. For the sequentially-phased mode, TPMs do not seem to improve the dynamic response significantly, as the cases with no TPMs also provide very low vibration levels. Moreover, when the responses for two different in-phase modes are compared, the regions of TPM configurations which would lead to the maximum reduction of dynamic response are also different. For the example PGT, optimum TPMs for the interval of 6000-10000 sun rpm leads to an inadequate reduction of both sun-planet and ring-planet vibration in 2500-6000 sun rpm interval. Therefore designers should also account for the speed intervals during operation in their choice for TPMs for PGTs. This mentioned dependence on speed lies in the phenomenon of different excitation modes that are expected to occur due to the parameters of PGT design. Since a TPM cannot provide an ideal solution for all excitation modes, one can also consider optimizing the number of gear teeth such that only a certain mode is expected within a defined speed range. Therefore, a combination of appropriate mesh phasing configuration along with proper TPMs can lead to the most ideal solutions for PGT systems in order to reduce vibrations.

It is a common practice for gear designers to apply TPMs solely based on the applied load searching for TPMs that result in a minimum variation of LSTE. However for PGTs, as it is shown in this study, the dynamic mesh displacement depends significantly on the unique features of PGTs. Bahk and Parker [51] also found in their study that the TPMs which give minimum LSTEs do not necessarily result in minimum dynamic mesh displacement. Therefore, even if applying TPMs which result in minimum LSTE variation can be helpful in some operational speed ranges, it is clear that it may not work at maximum efficiency for every speed interval. Consequently, as a first step, speed intervals in which LSTE approach work and the ones in which a minimum variation in LSTE does not result in a minimum variation in dynamic mesh displacement are identified. Since different dynamic modes of the system are excited depending on the speed intervals, the relationship between

dynamic modes and effectivity of TPMs based on minimization of LSTE variation are studied next.

Table 6-4 gives the TPMs for which a minimum LSTE is obtained for the load range of 1600Nm – 4800Nm sun torque:

Table 6-4 TPMs leading to minimum LSTE for sun-planet and ring-planet meshes

Sun torque [Nm]	Sun TPM amount [μm]	Planet TPM amount [μm]
1600	12	9
2400	18	15
3200	22	18
4000	28	22
4800	33	25

Figure 6-5 and plot a) in Figure 6-8, when evaluated together with the information in Table 6-4, show that when TPMs which minimize LSTE variation are applied, the dynamic response is also reduced to a great extent in terms of dynamic mesh displacements and dynamic mesh forces, respectively. These plots are obtained for the sun speed interval between 1000- 6000 rpm and 2500-6000rpm, respectively. It is already mentioned that in these speed ranges dynamic response is dominated by the harmonics of the first in-phase mode. Hence for the dynamic behavior characterized by this mode, minimizing LSTE variation is also helpful for an ideal reduction of the vibration. However, as indicated previously, while discussing the effect of different modes on the response of PGTs with TPMs, optimum TPMs are different for the other cases where vibration is dictated by the harmonics of “sequentially-phased” or second “in-phase” modes. Therefore, optimum TPMs for these speed ranges are also different from the optimum TPMs obtained for the minimization of LSTE variation.

6.4 Summary and conclusion

In this chapter, the effects of linear and parabolic TPMs on the dynamic behavior of PGTs are investigated in detail. Linear and parabolic TPMs are most commonly used types of profile modifications, which are employed in order to improve the dynamic characteristics of gear systems, including PGTs.

A purely-torsional mathematical model is employed for the simulations of an example PGT with various configurations of TPMs. Time-varying mesh stiffness functions for the proposed non-linear, time-varying model are calculated based on the LSTE values. A similar approach was used in the study of Tamminana et al. [69] for spur gears which showed very good correlation with both experimental and FE results. In order to check validity of this model for planetary gears, dynamic response results of the theoretical model are compared for an example PGT, with those that are obtained through Transmission3D, which is a combined FE-contact mechanics tool that is widely used in the field. The outcome of the comparisons built confidence in going forward with investigation of dynamic characteristics of PGTs with TPMs, using the proposed model.

The solution for the proposed analytical model is performed using harmonic balance method with arc length continuation. Multiple solutions may exist at the resonance regions due to the backlash nonlinearity. The ability of arc-length continuation scheme to find multiple solution points in non-linear response regions, without the necessity for performing forward and backward sweeps through desired speed ranges, makes this technique ideal for such a parametric study. The computational speed advantage over time-integration makes this solution method suitable for performing parametric studies. This solution method is also verified by comparing HBM and time-integration solutions on an example PGT.

Numerous dynamic simulations focusing different aspects of the effects of TPMs on PGTs are performed using the proposed method on an example gear set. The LSTE values required for the solution of the analytical model are obtained through the gear contact mechanics tool WindowsLDP of OSU, for each load-TPM configuration. LSTE data, by definition, contains the static deflection of the respective gear pairs as well as various deviations from the conjugate profile, including those due to profile modifications. Therefore, using the proposed method, it is possible to obtain an accurate calculation of dynamic response of PGTs with TPMs, by utilizing LSTE information only to estimate the mesh stiffness between respective gear pairs. Simulations are run for specified torque levels covering different speed intervals. Contour plots of dynamic response are presented to show the maximum dynamic response under different amounts of TPMs for the specific speed intervals under consideration.

When applied properly, the ability of TPMs in reducing the dynamic forces are shown clearly for both linear and parabolic TPMs. It is also demonstrated that since the mesh forces between sun-planet and ring-planet meshes are coupled, a combination of TPMs for both sun-planet and ring-planet meshes are necessary in order to benefit from an ideal reduction of dynamic mesh forces. Sensitivity of the dynamic mesh forces to the amount of TPMs is also an important subject due to the machining tolerances and wear. Parabolic modifications are observed to offer a wider range of efficiently reduced dynamic response compared to their linear counterparts. Moreover, when ideal TPMs for different load levels are considered, parabolic TPMs are also observed to perform better than linear TPMs at load levels that are lower than the design torque for that particular TPM.

PGTs have specific modal characteristics. Different natural modes dictate not only the dynamic characteristics of PGTs but also the design of ideal TPMs for vibration reduction. Ideal TPM configuration in terms of improving the dynamic characteristics of PGT changes for different speed intervals due to excitation of

harmonics of different natural modes. In the example case study performed, it is found that for “sequentially-phased” mode, the ideal dynamic behavior is obtained when no TPM is applied. Such conclusions can lead to design solutions where the dynamic characteristics of a PGT can be optimized using a combination of proper mesh phasing and TPMs.

This dependence of the ideal TPM configuration on the natural modes also answers the question whether the minimization of LSTE variation for sun-planet and ring-planet meshes certainly means a satisfactory improvement in dynamic behavior of PGTs. For the example PGT, TPMs designed for minimization of variation of LSTE lead to an efficient improvement of the dynamics for the speed intervals in which the harmonics of the first in-phase mode are excited. However this is not the case for the speed ranges in which various harmonics of the “sequentially-phased” and “second in-phase” modes are excited. Therefore for reduction of vibration in PGTs, a TPM configuration which results in minimizing LSTE variation for both sun-planet and ring-planet meshes may not be considered as the ultimate remedy.

The above findings can be translated into design practices for TPMs on PGTs. The load levels and speed intervals expected for the operation are very important in selecting the ideal TPM for improvement of PGT dynamics. In addition, other aspects of design such as manufacturing tolerances and wear on gears may play major roles in selecting an ideal TPM configuration which can be taken into consideration in the mathematical model proposed, since such effects are included into the analysis through LSTE calculated by WindowsLDP.

CHAPTER 7

DYNAMIC CHARACTERIZATION OF DOUBLE-RELIEF PROFILE

MODIFICATIONS IN PLANETARY GEAR SYSTEMS

7.1 Introduction

High contact ratio (HCR) spur gears are defined as gear pairs that have a contact ratio between 2.0 and 3.0. Due to the increased contact ratio, expected load capacity is higher than their low contact ratio (LCR) counterparts, since the load is shared among 2 or 3 gear teeth instead of 1 or 2. Tooth geometry-wise, in order to end up with HCR gears, addendum of the gears are generally kept higher than that of LCR gears. Furthermore, a finer module is preferred for HCR gear pairs. However, such modifications in geometry may result in gear teeth which can be more vulnerable to bending, when compared with the tooth geometry of LCR gears.

In order to neutralize this disadvantage of HCR gears, a further improvement of the dynamic condition is possible through a proper application of tooth profile modifications (TPMs). In addition to the conventional linear and parabolic TPM designs, Yildirim et al. [74] proposed double-relief type profile modifications, which are claimed to combine the advantages of short-relief and long-relief types of TPM designs. In a joint work with Leonardo Helicopters (formerly known as Agusta Westland), Yildirim et al. [75] also presented some experimental evidence for better dynamic characteristics of double-relief TPM design when compared with conventional linear TPM design on a parallel-axis gearbox. They showed a reduction of noise level between 7 to 11 dBA for the respective gearbox, in addition to a highly-reduced housing vibration.

Although experimental results are promising, there is still a need for dynamic characterization of double-relief TPMs through mathematical modeling of gear dynamics. In this study, dynamic characteristics of double-relief modifications are investigated for planetary gear systems. A mathematical model of the planetary gear system which uses an average (constant) mesh stiffness for the respective sun-planet and ring-planet gear pairs, but includes mesh stiffness variation through LSTE is employed for this purpose. Dynamic excitation, modeled using LSTE information between the respective gear meshes includes mesh stiffness variation, as well as the effects of gear errors and profile modifications. Multi-term Harmonic Balance Method (HBM) with arc length continuation scheme is used for the solution of the mathematical model.

Using the mathematical model, dynamic response of an example PGT is obtained at different torque levels for two cases: with a conventional linear TPM and with double-relief TPM. Comparisons are made between the calculated dynamic responses, and the advantages of double-relief TPM over linear TPM are discussed.

7.2 Double-relief TPMs

Profile modification can be defined as an intended removal of material from the tip and/or root regions of the gear tooth profile. TPMs are usually employed on the spur gear pairs in order to improve their dynamic characteristics. This is also true for the PGTs comprised of spur gears.

Aside from the improvement in dynamic characteristics, designers employ profile modifications also to avoid a possible corner contact of gear teeth, even at maximum design loads. When this is desired, then one can determine the amount of profile modification based on the expected deformation of the gear teeth under the maximum load. The location for the start of the modification is then a critical

parameter which would define the characteristics of the profile modification. Both for LCR and HCR gears, TPMs can be classified based on the initial point of modification. A detailed explanation of this topic along with the advantages and disadvantages of different relief types are given in reference [45].

For HCR gears, one can classify the conventional linear profile modifications as “short-relief” and “long-relief” depending on the starting position of the TPM. For “long-relief”, TPM is extended into the double-contact region. This approach results in two nearly-smooth LSTE curves, one being at the maximum design load and the other is at some intermediate load. However one major set-back for this type of TPMs is that at maximum design load, a single tooth pair shares more than half of the load, as a result of the modification in double-contact region. For “short-relief”, modification starts at the highest point of triple-contact region. Therefore at maximum load, a single tooth pair does not carry more than half of the load, which makes “short-relief” more favorable in practice when compared with “long-relief”. However for this case, it is possible to have only one nearly-smooth LSTE curve, which occurs at maximum design load. This characteristic of LSTE results in poor dynamic characteristics at lower torque levels.

In order to combine the advantages of the above mentioned two types of TPMs, Yildirim *et al.* proposed a new relief type, which is named as “double-relief” such that TPM is applied in 2 steps, with different slopes at double-contact and triple-contact regions [74]. Thus, the maximum static load carried by a single tooth pair is reduced compared with a similar long-relief modification. On the other side, LSTE variation is still minimum at 2 load levels, unlike the minimum LSTE variation value obtained at a single load level for short-relief modifications.

Figure 7-1 shows the combined tooth profile plot for an example gear pair with double-relief TPM.

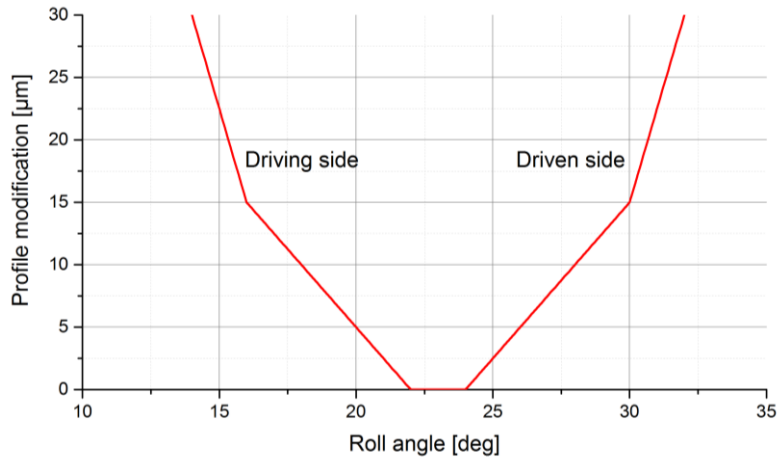


Figure 7-1 Combined tooth profile plot for a gear pair with double-relief TPM

7.3 Mathematical Model and Solution Method

The employed mathematical model in this study is a nonlinear time invariant model. Average mesh stiffness is assumed both for the sun-planet and ring-planet gear pairs. The excitation effect of mesh stiffness variation is modeled by using LSTE between the respective gear meshes. This modeling approach was first proposed by Ozguven and Houser for spur gear pairs in 1988 [61]. Recent studies show that this model yields accurate results for also the cases where TPMs are applied [76]. This model has been frequently used in the literature for dynamic modeling of PGTs. References [8,9] can be given as examples of planetary gear dynamics studies where such a model is applied.

The equations of motion with the above listed conditions can be written as follows

$$M_s \ddot{x}_s(t) + c_{sp} \sum_{i=1}^{n_p} \dot{z}_{si}(t) + \sum_{i=1}^{n_p} g_{si}(t) + k_s x_s(t) = k_{sp} \sum_{i=1}^{n_p} e_{si}(t), \quad (7.1)$$

$$M_r \ddot{x}_r(t) + c_{rp} \sum_{i=1}^{n_p} \dot{z}_{ri}(t) + \sum_{i=1}^{n_p} g_{ri}(t) + k_r x_r(t) = k_{rp} \sum_{i=1}^{n_p} e_{ri}(t) \quad (7.2)$$

$$M_c \ddot{x}_c(t) - c_{sp} \sum_{i=1}^{n_p} \dot{z}_{si}(t) - c_{rp} \sum_{i=1}^{n_p} \dot{z}_{ri}(t) - \sum_{i=1}^{n_p} g_{si}(t) - \sum_{i=1}^{n_p} g_{ri}(t) + k_c x_c(t) = -k_{rp} \sum_{i=1}^{n_p} e_{ri}(t) - k_{sp} \sum_{i=1}^{n_p} e_{si}(t), \quad (7.3)$$

$$M_i \ddot{x}_i(t) + c_{sp} \dot{z}_{si}(t) - c_{rp} \dot{z}_{ri}(t) + g_{si}(t) - g_{ri}(t) = k_{sp} e_{si}(t) - k_{rp} e_{ri}(t), \quad (i=1, 2, \dots, n_p) \quad (7.4)$$

where

$$M_s = \frac{I_s}{r_s^2}, \quad M_r = \frac{I_r}{r_r^2}, \quad M_c = \frac{I_c}{r_c^2} + n_p m_i. \quad (7.5)$$

Note that k_{sp} and k_{rp} are the average mesh stiffness parameters for the sun-planet and ring-planet gear pairs, respectively. $e_{si}(t)$ is the LSTE between the sun and the i^{th} planet. Similarly, $e_{ri}(t)$ is the LSTE between ring and the i^{th} planet. The definitions of the symbols and abbreviations, which are not given here, can be found in Nomenclature. Nonlinear forcing due to the backlash between the sun-planet ($g_{si}(t)$) and ring-planet ($g_{ri}(t)$) pairs are given as follows:

$$g_{si}(t) = \begin{cases} k_{sp} [z_{si}(t) - b] & \text{for } z_{si}(t) > b \\ 0 & \text{for } -b \leq z_{si}(t) \leq b \\ k_{sp} [z_{si}(t) + b] & \text{for } z_{si}(t) < -b \end{cases}, \quad (7.6)$$

and

$$g_{ri}(t) = \begin{cases} k_{rp} [z_{ri}(t) - b] & \text{for } z_{ri}(t) > b \\ 0 & \text{for } -b \leq z_{ri}(t) \leq b \\ k_{rp} [z_{ri}(t) + b] & \text{for } z_{ri}(t) < -b \end{cases}. \quad (7.7)$$

Sun-planet mesh displacement function ($z_{si}(t)$) and ring-planet mesh displacement function ($z_{ri}(t)$) can be expressed as

$$z_{si}(t) = x_s(t) + x_i(t) - x_c(t), \quad (7.8)$$

$$z_{ri}(t) = x_r(t) - x_i(t) - x_c(t). \quad (7.9)$$

Using multi-term HBM, nonlinear differential equations of motion given by Eqs. 7.1 -7.4 can be converted into a set of nonlinear algebraic equations. The periodic excitation in terms of LSTE for both sun-planet and ring-planet meshes, respectively, can be expressed in Fourier series (using a total number of N harmonics) as

$$e_{si}(t) = E_{si,1} + \sum_{n=1}^N \left(E_{si,2n} \cos(n\omega t) + E_{si,2n+1} \sin(n\omega t) \right), \quad (7.10)$$

$$e_{ri}(t) = E_{ri,1} + \sum_{n=1}^N \left(E_{ri,2n} \cos(n\omega t) + E_{ri,2n+1} \sin(n\omega t) \right). \quad (7.11)$$

Phase relationships are considered in formulating the excitation in terms of LSTE, based on a reference mesh, both for sun-planet and ring-planet meshes. The phasing equations for LSTE functions can be expressed as follows for sun-planet mesh:

$$E_{si,2n} = E_{s1,2n} \cos(nZ_s \Phi_i), \quad (7.12)$$

$$E_{si,2n+1} = E_{s1,2n+1} \sin(nZ_s \Phi_i). \quad (7.13)$$

For ring-planet mesh:

$$E_{ri,2n} = E_{r1,2n} \cos(nZ_r \Phi_i + n\varphi_{sr}), \quad (7.14)$$

$$E_{ri,2n+1} = E_{r1,2n+1} \sin(nZ_r \Phi_i + n\varphi_{sr}). \quad (7.15)$$

Here Z_s and Z_r denote the number of teeth for sun and ring gears, respectively. Φ_i is the angular position of the i^{th} planet (i.e. for an equally spaced 4-planet system, planets are positioned at $0, \pi/2, \pi$ and $3\pi/2$, respectively). φ_{sr} is the phase difference between sun-planet and ring-planet meshes.

The assumed solution to Eqs. 7.1 – 7.4 can be expressed in Fourier series form as follows

$$x_a(t) = X_{a,1} + \sum_{n=1}^N (X_{a,2n} \cos(n\omega t) + X_{a,2n+1} \sin(n\omega t)), \quad (7.16)$$

where $a = s, r, c, 1, 2, \dots, n_p$. The resulting nonlinear algebraic equations can be given as shown below.

For sun gear:

$$R_1^s = k_s X_{s,1} + \sum_{i=1}^{n_p} G_{si,1} - k_{sp} \sum_{i=1}^{n_p} E_{si,1} = 0, \quad (7.17)$$

$$R_{2n}^s = k_s X_{s,2n} - n\omega^2 M_s X_{s,2n} + 2n\omega c_{sp} \sum_{i=1}^{n_p} Z_{si,2n+1} + \sum_{i=1}^{n_p} G_{si,2n} - k_{sp} \sum_{i=1}^{n_p} E_{si,2n} = 0, \quad (7.18)$$

$$R_{2n+1}^s = k_s X_{s,2n+1} - n\omega^2 M_s X_{s,2n+1} - 2n\omega c_{sp} \sum_{i=1}^{n_p} Z_{si,2n} + \sum_{i=1}^{n_p} G_{si,2n+1} - k_{sp} \sum_{i=1}^{n_p} E_{si,2n+1} = 0 \quad (7.19)$$

For ring gear:

$$R_1^r = k_r X_{r,1} + \sum_{i=1}^{n_p} G_{ri,1} - k_{rp} \sum_{i=1}^{n_p} E_{ri,1} = 0, \quad (7.20)$$

$$R_{2n}^r = k_r X_{r,2n} - n\omega^2 M_r X_{r,2n} + 2n\omega c_{rp} \sum_{i=1}^{n_p} Z_{ri,2n+1} + \sum_{i=1}^{n_p} G_{ri,2n} - k_{rp} \sum_{i=1}^{n_p} E_{ri,2n} = 0, \quad (7.21)$$

$$R_{2n+1}^r = k_r X_{r,2n+1} - n\omega^2 M_r X_{r,2n+1} - 2n\omega c_{rp} \sum_{i=1}^{n_p} Z_{ri,2n} + \sum_{i=1}^{n_p} G_{ri,2n+1} - k_{rp} \sum_{i=1}^{n_p} E_{ri,2n+1} = 0 \quad (7.22)$$

For carrier:

$$R_1^c = k_c X_{c,1} - \sum_{i=1}^{n_p} G_{si,1} - \sum_{i=1}^{n_p} G_{ri,1} - k_{sp} \sum_{i=1}^{n_p} E_{si,1} - k_{rp} \sum_{i=1}^{n_p} E_{ri,1} = 0, \quad (7.23)$$

$$R_{2n}^c = k_c X_{c,2n} - n\omega^2 M_c X_{c,2n} - 2n\omega c_{sp} \sum_{i=1}^{n_p} Z_{si,2n+1} - 2n\omega c_{rp} \sum_{i=1}^{n_p} Z_{ri,2n+1} - \sum_{i=1}^{n_p} G_{si,2n} - \sum_{i=1}^{n_p} G_{ri,2n} - k_{sp} \sum_{i=1}^{n_p} E_{si,2n} - k_{rp} \sum_{i=1}^{n_p} E_{ri,2n} = 0 \quad (7.24)$$

$$R_{2n+1}^c = k_c X_{c,2n+1} - n\omega^2 M_c X_{c,2n+1} + 2n\omega c_{sp} \sum_{i=1}^{n_p} Z_{si,2n} + 2n\omega c_{rp} \sum_{i=1}^{n_p} Z_{ri,2n} - \sum_{i=1}^{n_p} G_{si,2n} - \sum_{i=1}^{n_p} G_{ri,2n+1} - k_{sp} \sum_{i=1}^{n_p} E_{si,2n+1} - k_{rp} \sum_{i=1}^{n_p} E_{ri,2n+1} = 0 \quad (7.25)$$

For planets:

$$R_1^i = G_{si,1} - G_{ri,1} - k_{sp} E_{si,1} + k_{rp} E_{ri,1} = 0, \quad (7.26)$$

$$R_{2n}^i = -n\omega^2 M_i X_{i,2n} + 2n\omega c_{sp} Z_{si,2n+1} - 2n\omega c_{rp} Z_{ri,2n+1} + G_{si,2n} - G_{ri,2n} - k_{sp} E_{si,2n} + k_{rp} E_{ri,2n} = 0 \quad (7.27)$$

$$\begin{aligned}
R_{2n+1}^i &= -n\omega^2 M_i X_{i,2n+1} - 2n\omega c_{sp} Z_{si,2n} + 2n\omega c_{rp} Z_{ri,2n} + G_{si,2n+1} - G_{ri,2n+1} \\
-k_{sp} E_{si,2n+1} + k_{rp} E_{ri,2n+1} &= 0
\end{aligned} \tag{7.28}$$

Therefore the nonlinear algebraic equation vector \mathbf{R} is formed as

$$\mathbf{R} = \left\{ \begin{array}{l} \left(R_{s,1}, \dots, R_{s,2N+1}, R_{r,1}, \dots, R_{r,2N+1}, R_{c,1}, \dots, R_{c,2N+1} \right)^T \\ \left(R_{1,1}, \dots, R_{1,2N+1}, R_{2,1}, \dots, R_{2,2N+1}, \dots, R_{n_p,1}, \dots, R_{n_p,2N+1} \right)^T \end{array} \right\}. \tag{7.29}$$

Solution of the nonlinear algebraic equation set is done by utilizing Newton's method with arc-length continuation. Details of the mentioned solution method can be found in [52,77,78].

7.4 Validation of Solutions Obtained by Multi-Term HBM

Solutions obtained by multi-term HBM are compared with solutions obtained by direct time-integration on an example PGT. For this PGT, sun gear is the input member, whereas ring gear is fixed.

Short-relief TPMs are applied at the tip of the working flanks for all gears. Modifications start from the lowest point of triple contact at the tip for the respective gear teeth.

In this study, LSTE is calculated as a function of gear mesh stiffness, no-load transmission error (due to TPMs) and the static mesh force. Mesh stiffness function is assumed to be in rectangular form such that the mesh stiffness at a particular point is equal to the number of teeth in contact times the respective mesh stiffness of a single tooth pair. For details of the calculation of LSTE using this approach, one can refer to [45].

6 harmonics are used in the Fourier series representation of LSTE functions between sun-planet and ring planet gear meshes, respectively, and also in the representation of the displacement vector.

Table 7-1 gives the parameters for the example PGT, on which short-relief TPM is applied.

Table 7-1 Parameters of example PGT

	SUN	PLANET	RING
Number of planets	4		
Number of teeth	32	24	80
Contact ratio	2.31		2.28
Mesh stiffness of single tooth pair [N/m]	2.2e8		2.5e8
Equivalent inertia, I/r_b^2 [kg]	1.2	0.624	12
Torque applied [Nm]	2400	-	-
Viscous damping coefficients [Ns/m]	1470		1380
Static mesh force [N]	5000		
Amount of modification in triple contact region [μm]	23		20

Figure 7-2 shows the comparison of the sun gear displacement (rms) obtained by using HBM and direct time integration. Time-integration solution is obtained by using ODE45 routine in Matlab. Results of the comparison study showed that HBM with 6 harmonics captures the steady state response of the PGT system under consideration accurately. Multiple solutions are obtained with HBM at several resonant frequencies which cannot be determined by direct time integration.

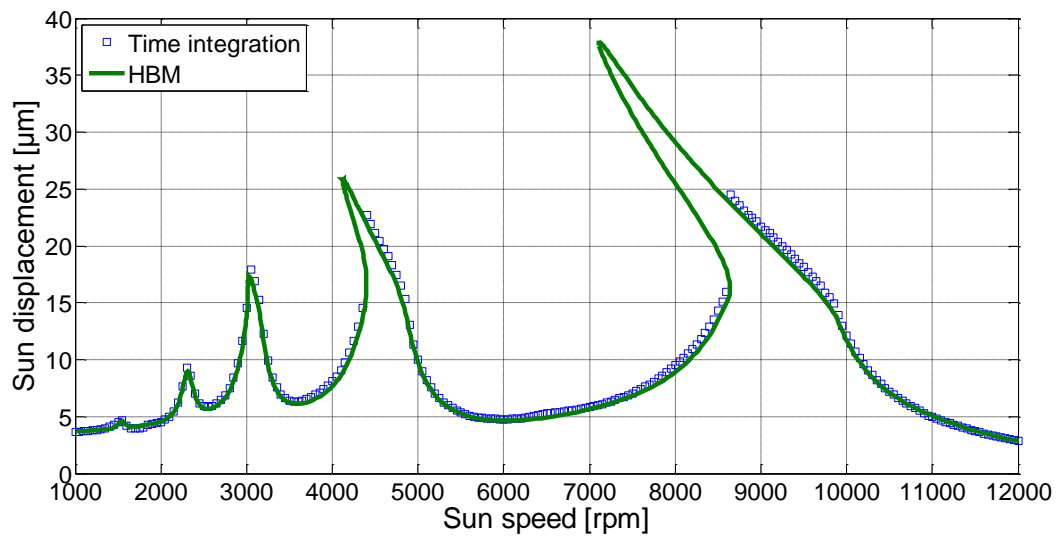


Figure 7-2 Comparison of sun gear displacement (rms) obtained by using TI and HBM

7.5 Comparison of Dynamic Response for HCR PGTs with Linear Relief and Double-Relief TPMs

The advantages of double-relief TPMs in terms of dynamic response over the conventional linear relief are investigated in this section. Comparisons will be made with a “short-relief” design, where the TPM is applied from the start of the triple-contact region at the tip of mating gears. The total amounts of modifications for both TPM types are adjusted such that they are just enough to avoid corner contact at the maximum load. TPM application scheme for the short-relief TPM is already provided in Section 7.4. For double-relief TPM, constant slope modification starts from the lowest point of double contact at the tip for the respective gear teeth, and at the lowest point of triple contact the slope of the modification changes. Figure 7-3 gives the LSTE data for both TPM schemes. The maximum static mesh force (design load) is given as 10kN. The curves are provided from “no-load” to design load in 10% intervals.

It is obvious from Figure 7-3 that, for double-relief TPM, LSTE variation is nearly non-existent at two load levels, one being at the design load (100%) and the other is around 30% of the design load,. However, for this type of TPM, since extend of the modification also includes double-contact region; one can end up with actual contact ratios less than 2.0 for lightly loaded cases. This also results in increased LSTE variation for the mentioned load levels.

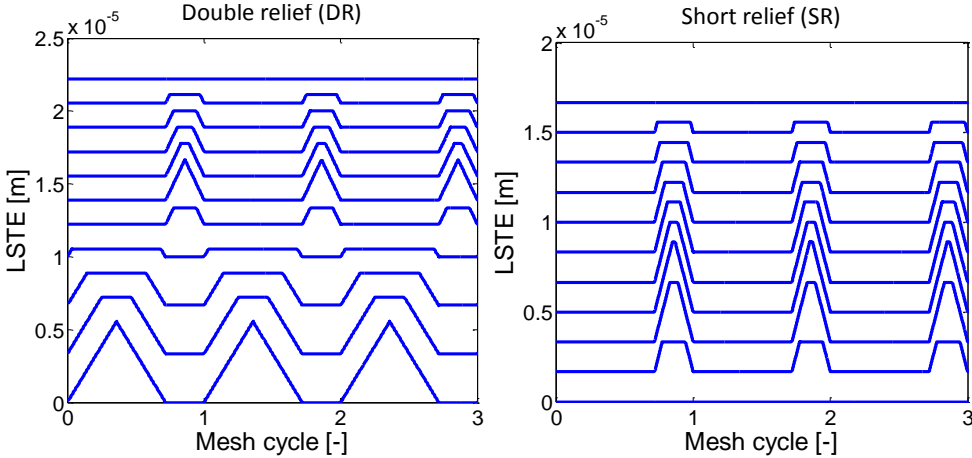


Figure 7-3 LSTE for double-relief (top) and linear TPMs (bottom). The load is increased from no-load (curves at the bottom of the plots) to maximum design load in 10% intervals.

The investigation is made in two steps. Firstly, the dynamic response in the interval of 50 to 100% of the design load is analyzed for both types of TPMs, in 10% increments. Figure 7-4 shows the dynamic response for both TPM types at each load level in this interval, in terms of rms of sun displacement.

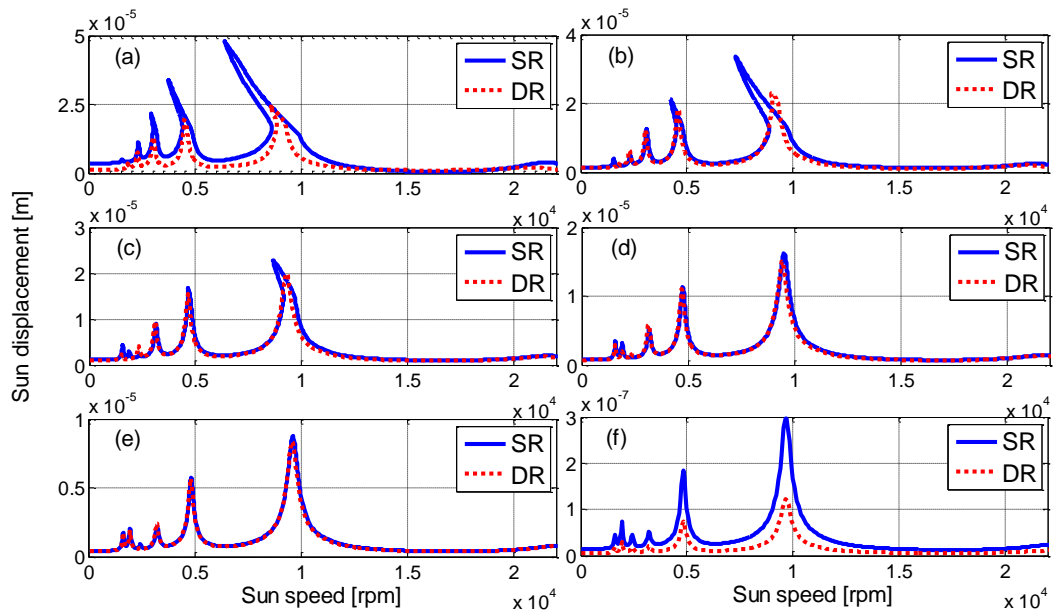


Figure 7-4 Sun gear displacement (rms) for a) 50%, b) 60%, c) 70%, d) 80%, e) 90% and f) 100% design load

Figure 7-5 shows rms of planet displacement for both TPM types at each load level in the interval of 50 to 100% of the design load.

Figure 7-4 and Figure 7-5 show that, considering the load levels away from the design load at which the respective TPMs are designed for, double-relief TPM shows better performance in terms of vibration. On the other hand, near the design load, the vibration levels are comparable.

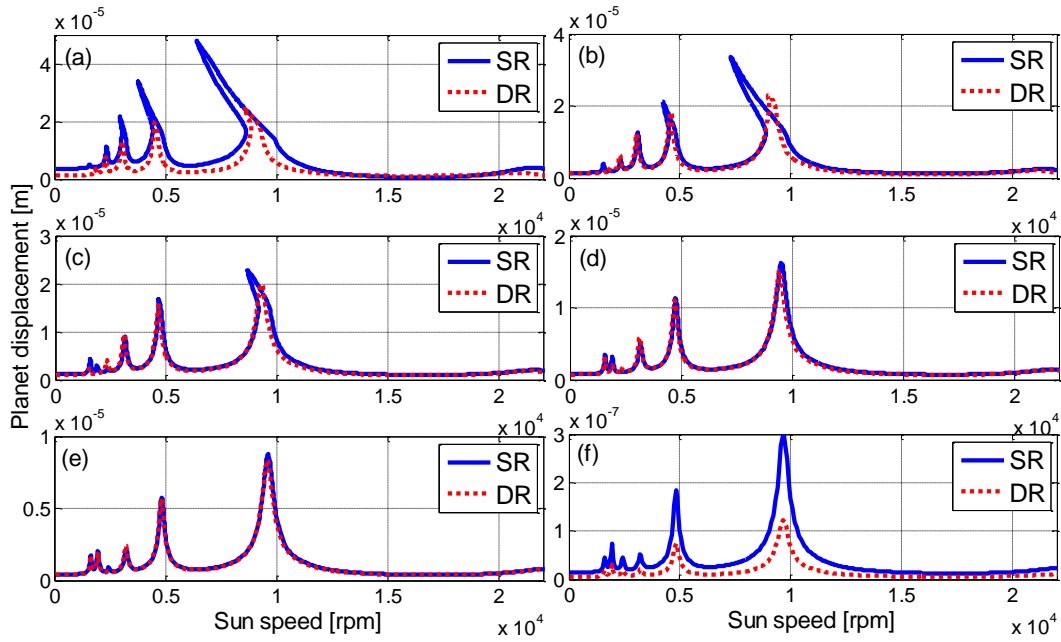


Figure 7-5 Planet gear displacement (rms) for a) 50%, b) 60%, c) 70%, d) 80%, e) 90% and f) 100% design load

Figure 7-6 shows the maximum dynamic sun-planet mesh force and ring-planet mesh force for different loads between 50-100% of the design load, in the whole speed range under consideration.

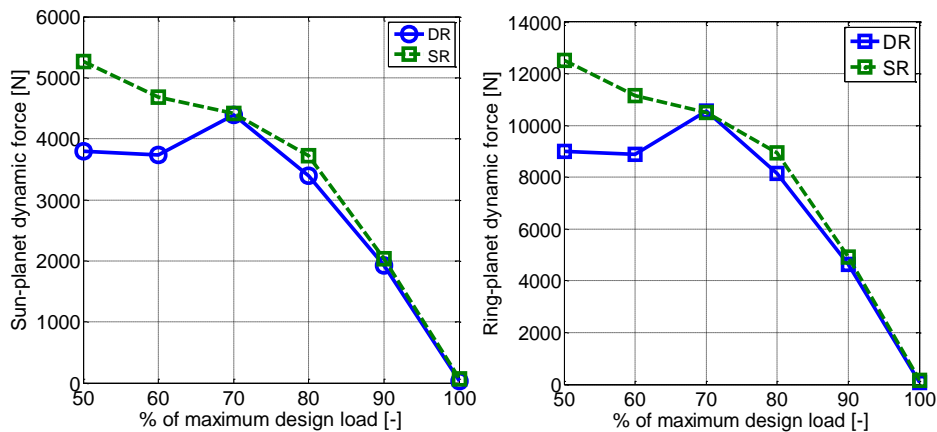


Figure 7-6 Maximum dynamic force for double-relief and short-relief cases in the interval of 50-100% of the design load

The results for the dynamic mesh forces are in line with those for the displacement results. It is worth considering here that, when one gets away from the design load to lower load levels, the dynamic forces can increase with a high rate. Since the combination of static and dynamic mesh forces are important for gear fatigue, such an increase in dynamic mesh forces can make an intermediate load level the most critical loading in terms of fatigue, other than the (static) design load.

For the short-relief TPM case, the total (dynamic + static) mesh load values are very close to each other in the range 50-80% of the design load. The maximum of total mesh load values (e.g. for ring-planet meshes which is around 17kN) is also observed in this range. The maximum value of the total mesh load for double-relief TPM case is comparable to that of the short-relief TPM case. However, for short-relief, the total mesh load makes a peak at 70% of the design load and decreases steadily away from the peak location. Therefore the highest levels of the total mesh load are not observed in a wide load range. When combined with the operational spectrum, which gives information about the load levels and time spent at these loads during the lifetime of the component, such information may show important advantages of double-relief modification, compared to short-relief type of TPMs.

In a second case study, the load levels between 20-50% of the design load are investigated. Figure 7-7 shows rms sun displacement for both TPM types at each load level in this interval. It is observed from the figure that except very lightly loaded cases (e.g. 20% design load), double-relief modification performs better than short-relief modification in terms of sun gear vibration. A similar characteristic is also valid for the planet gear vibration, although the related plots are not shown here.

For lightly loaded cases, contact ratio between mating gears is lower than 2.0 when double-relief modification is applied. For the PGT under consideration, this transition occurs at 32% percent of the maximum design load. The lower contact

ratio for the double-relief modification also shows itself in slightly lower natural frequencies than those of short-relief case. However, around this load level, since the LSTE variation is very little, dynamic performance of double-relief modification is still much better than that of the short-relief modification. However with decreasing load, LSTE variation grows and this leads to poorer dynamic characteristics for double-relief TPM in the example PGT.

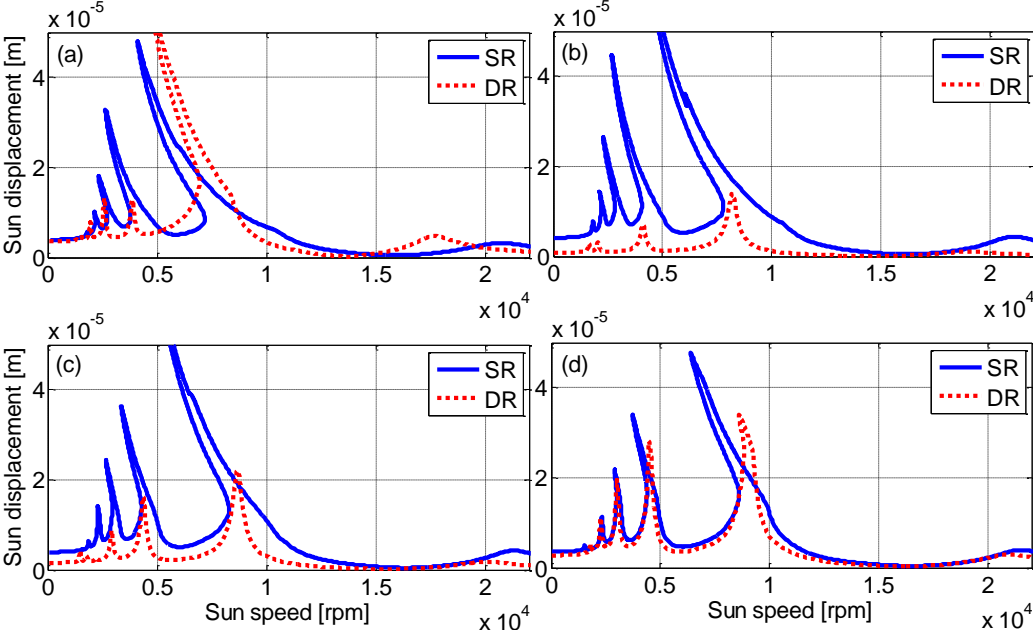


Figure 7-7 Sun gear displacement (rms) for a) 20%, b) 30%, c) 40%, d) 50% design load

Figure 7-8 shows the maximum dynamic sun-planet and ring-planet mesh forces in the range of 20-50% of the design load, in the whole speed range under consideration.

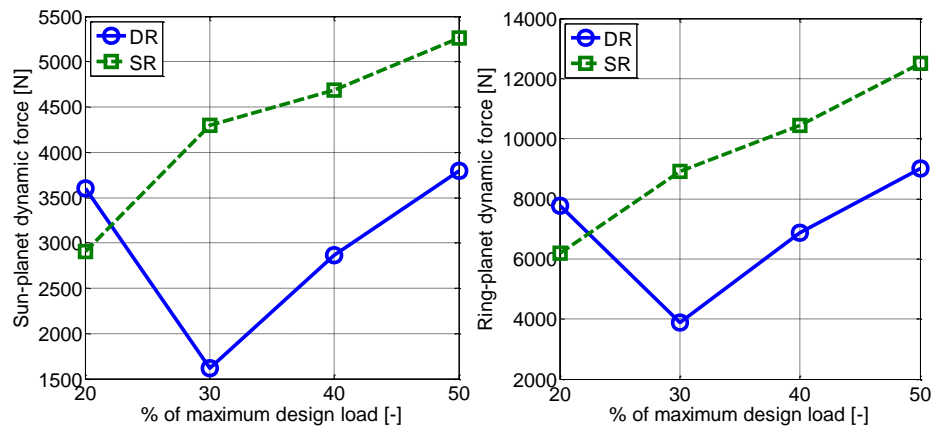


Figure 7-8 Maximum dynamic force for double-relief and short-relief cases in the interval of 20-50% of the design load

When combined with the outcomes of the analyses in the interval of 50-100% of the design load, Figure 7-8 shows that double-relief modification is very effective at the intermediate load levels. The maximum dynamic mesh forces are lower for double-relief modification for static mesh loads between 30-70% of the design load. In this interval, for the example PGT, the difference between dynamic mesh forces for short-relief and double-relief TPMs is significant. Provided an operational spectrum where mid-load levels are also important, this significant difference in dynamic mesh loads can be critical in terms of the fatigue life of the example PGT. Both TPM types are almost equally effective for the higher load levels that are closer to the design load. For the low-load levels (i.e. 0-30% of the design load), short-relief performs better than double-relief modification, mostly due to a higher contact ratio achieved at those load levels for short-relief TPM. However, the maximum mesh loads reached at low-load levels are not as high as those encountered at intermediate load levels.

7.6 Summary and Conclusion

In this study, dynamic analyses are performed for an example PGT with HCR spur gears, with two different TPM schemes, i.e. conventional linear relief and double-relief where TPM is applied in 2 steps with different slopes in triple contact region and double-relief region.

The advantages of double-relief TPMs have been discussed in early studies [74], in terms of static considerations, such as their ability to provide smooth LSTE curves at intermediate loads as well as limiting the maximum static mesh force faced by a single tooth pair. Regarding the dynamic effects of this TPM scheme, it was shown that in a comparison with its conventional linear counterpart, a double-relief TPM scheme resulted in less vibration and noise for a multi-mesh HCR spur gear system that is used in a helicopter [75]. Therefore the motivation for the current study is to show and characterize these improvements on an example PGT with HCR spur gears, using a mathematical model.

Ozguven's LSTE approach is used for this purpose, which is shown to be also working effectively for profile-modified gears [12,76]. In this approach, dynamic excitation to gears is modeled in terms of LSTE. Thus, although average mesh stiffnesses for the respective gear meshes are assumed, dynamic excitation due to tooth stiffness variation is included through loaded static transmission error (LSTE), which also includes gear errors and tooth profile modifications. This method greatly simplifies the complicated problem of modeling the mesh stiffness with profile modifications, as it combines the gear errors and elastic deflection of the gear teeth under one term, i.e. LSTE.

As the steady state solutions of the dynamic model are of interest, the model is solved using HBM with arc length continuation. This method is computationally

much more efficient than the numerical integration method in time domain. The validity of the solution method is shown on an example simulation by comparing solutions with HBM with those of time integration.

The dynamic characteristics of double-relief modifications are investigated on an example PGT with HCR spur gears. Comparisons are made with those obtained for the same PGT with conventional short-relief modification.

Both modifications are designed such that they are able to just avoid the corner contact at the maximum design load and one ends up with a minimum LSTE variation at the design load. Double-relief performed much better than short-relief especially at the intermediate loads, both in terms of vibration levels and dynamic mesh forces.

For the speed range under consideration, the maximum force (static mesh force + dynamic mesh force) on the respective sun-planet and ring-planet gear pairs are almost the same for the PGT with short-relief, for an extended range of loading. When fatigue evaluations are made based on a given operational spectrum, this will most probably mean that the PGT with short-relief spends more time on the critical service load levels than the PGT with double-relief. Therefore fatigue life of the example PGT is expected to be longer for the double-relief TPM case.

At load levels near to design load, both modification schemes perform equally well. For lightly loaded cases (between 0-20% design load for this case), short-relief is more successful than their double-relief counterpart from dynamics point of view. This outcome is considered to be a result of the following: In short-relief TPM, gear tooth profile is modified only on the triple contact region, therefore the contact ratio is greater than 2 for all load levels, unlike the case in double-relief modification. The dynamic mesh forces for double-relief TPM are higher than their short-relief

counterparts at lower load levels. However, the difference is not very significant when fatigue is considered.

CHAPTER 8

SUMMARY and FUTURE WORK

8.1 Summary

An extensive parametric study of PGT dynamics is performed in this dissertation. The effects of various design parameters on the dynamic behavior of PGTs are studied, emphasis is being on the ways of improving the dynamic response of PGTs.

The purely torsional mathematical model used throughout the dissertation study is introduced first. Information about the Harmonic Balance Method, which is used for solution of the mathematical model, is provided. The modal characteristics of PGTs are important both for understanding the dynamic response of PGTs and evaluating the effects of parameters. Therefore, general information about the modal properties of PGTs is also included in the dissertation.

Next, the concept of mesh phasing, which is also a key concept in PGT dynamics is discussed in detail with the focus being at the relationship between the mesh phasing and the natural modes of PGTs. Then the effects of the fundamental parameters, namely the amount of backlash between gear meshes, damping levels and the gear contact ratios, on PGT dynamic response are investigated. Feasible design guidelines for reducing the dynamic response of PGTs are provided out of the outcomes of the mentioned studies.

PGTs with thin ring gears are often used in rotorcraft main rotor drive systems not only because of the advantages in terms of weight but also due to their positive effects on the load sharing of PGTs. In this study the effects of elasticity parameters

on the torsional dynamics of PGTs are investigated. Uniformly curved beam theory is used for calculating the stiffness contribution of elastic rims.

TPMs are very effective means of reducing the vibration and the associated adversities such as noise and increased dynamic loading in spur gears. However TPM designs are usually performed with the target being the minimization of the loaded static transmission error. First it is shown for spur gears that a direct objective function of minimizing the dynamic transmission error can lead to ideal TPM designs. It is also demonstrated that the differences in response of rigid and compliant systems can be critical in determining the optimum TPM using such an approach. Next, the direct effect of TPMs on reducing the dynamic loads and increasing the tooth bending fatigue lives of spur gears are investigated.

After a detailed work on the effects of TPMs in spur gears, the effects and characteristics of TPMs on PGT dynamics are extensively studied. To begin with, the proposed analytical model for the evaluation of TPMs is verified by comparisons with a dedicated computational tool that is specialized in geared systems. After a successful validation of the analytical model, the effects of linear and parabolic TPMs on PGT dynamics are investigated under different operational conditions. Important outcomes are reached in terms of both the effectivity of TPMs and sensitivity of TPM parameters. A strong dependence of ideal TPM design on the mode shapes is observed. Differences between the LSTE-optimized TPMs and dynamically optimized TPMs are shown.

Finally effects of double-relief TPMs on the dynamic characteristics of the HCR PGTs are investigated. Potential advantages of double-relief TPMs in terms of fatigue are shown with comparisons between double-relief TPMs and conventional linear TPMs.

8.2 Future work

The study also reveals some points which can be studied extensively beyond the scope of the current work.

- Comparison of the results of the time-integration method with the analytical method showed that subharmonics can also be observed for nonlinear PGT dynamics, at higher speeds. HBM solution therefore can be extended to include the subharmonics.
- In this study, a purely torsional model is used since it is sufficient to address the effects of many parameters; however the model can be extended to a 2D model in order to investigate the effects of bearing stiffness on PGT dynamics.
- While rim elasticity effects on PGT dynamics are studied, only the torsional stiffness of compliant ring gears is taken into account. It would be interesting also to investigate the effects of the bending modes of the elastic rings on PGT dynamics.
- A brute-force optimization scheme is used throughout the dissertation work, which is adequately efficient to derive fundamental characteristics of TPMs on gear dynamics. In a further study where the emphasis is on finding the optimum solution of TPMs, employing an efficient optimization algorithm is going to be more convenient.

REFERENCES

- [1] <http://www.machinedesign.com/motion-control/world-planetary-gears>.
- [2] Chiang, T., 1973, "Reduction of Vibration and Noise Generated by Planetary Ring Gears in Helicopter Aircraft Transmissions," (November).
- [3] Musial, W., Butterfield, S., and McNiff, B., 2007, "Improving Wind Turbine Gearbox Reliability Preprint," Eur. Wind Energy Conf., pp. 1–13.
- [4] <http://www.rotaryeng.net/psrus.html>.
- [5] <https://mechanical-engg.com/gallery/image/1790-gearbox-of-a-wind-turbinejpg/>.
- [6] Cooley, C. G., and Parker, R. G., 2014, "A Review of Planetary and Epicyclic Gear Dynamics and Vibrations Research," Appl. Mech. Rev., **66**(4), p. 040804.
- [7] Al-shyyab, A., and Kahraman, A., 2007, "A Non-Linear Dynamic Model for Planetary Gear Sets," Proc. Inst. Mech. Eng. Part K J. Multi-body Dyn., **221**(4), pp. 567–576.
- [8] Inalpolat, M., and Kahraman, A., 2008, "Dynamic Modelling of Planetary Gears of Automatic Transmissions," Proc. Inst. Mech. Eng. Part K J. Multi-body Dyn., **222**(3), pp. 229–242.
- [9] Kahraman, A., 1994, "Planetary Gear Train Dynamics," J. Mech. Des., **116**(3), p. 713.
- [10] Eritenel, T., and Parker, R. G., 2009, "Modal Properties of Three-Dimensional Helical Planetary Gears," J. Sound Vib., **325**, pp. 397–420.
- [11] Kahraman, A., 1994, "Natural Modes Of Planetary Gear Trains," J. Sound Vib., **1**(173), pp. 125–130.
- [12] Liu, G., and Parker, R. G., 2008, "Dynamic Modeling and Analysis of Tooth Profile Modification for Multimesh Gear Vibration," J. Mech. Des., **130**(12), p. 121402.
- [13] Inalpolat, M., and Kahraman, A., 2010, "A Dynamic Model to Predict

- Modulation Sidebands of a Planetary Gear Set Having Manufacturing Errors,” *J. Sound Vib.*, **329**(4), pp. 371–393.
- [14] Sondkar, P., and Kahraman, A., 2013, “A Dynamic Model of a Double-Helical Planetary Gear Set,” *Mech. Mach. Theory*, **70**, pp. 157–174.
- [15] Lin, J., and Parker, R. G., 2002, “Planetary Gear Parametric Instability Caused By Mesh Stiffness Variation,” *J. Sound Vib.*, **249**(1), pp. 129–145.
- [16] Velez, P., and Flamand, L., 1996, “Dynamic Response of Planetary Trains to Mesh Parametric Excitations,” *J. Mech. Des. Trans. ASME*, **118**(March 1996), pp. 7–14.
- [17] Kahraman, A., and Blankenship, G. W., 1997, “Experiments on Nonlinear Dynamic Behavior of an Oscillator With Clearance and Periodically Time-Varying Parameters,” *J. Appl. Mech.*, **64**, pp. 217–226.
- [18] Tamminana, V. K., Kahraman, A., and Vijayakar, S., 2005, “A Study of the Relationship Between the Dynamic Factor and the Dynamic Transmission Error of Spur Gear Pairs,” *Int. Des. Eng. Tech. Conf. Comput. Inf. Eng. Conf.*, **1**(1), pp. 1–11.
- [19] Bahk, C.-J., and Parker, R. G., 2011, “Analytical Solution for the Nonlinear Dynamics of Planetary Gears,” *J. Comput. Nonlinear Dyn.*, **6**(2), p. 021007.
- [20] Eritenel, T., 2011, “Three-Dimensional Nonlinear Dynamics and Vibration Reduction of Gear Pairs and Planetary Gears,” *ProQuest Diss. Theses*, p. 218.
- [21] Cooley, C. G., 2012, “High-Speed Dynamics and Vibration of Planetary Gears, Vibration of Spinning Cantilevered Beams, and An Efficient Computational Method for Gear Dynamics,” *ProQuest Diss. Theses*.
- [22] Al-shyyab, A., 2007, “A Nonlinear Dynamic Model for Compound Planetary Gear Sets,” pp. 84–89.
- [23] Smith, J. D., 1974, “Dynamic Tooth Loads in Epicyclic Gears,” (May), pp. 578–584.
- [24] Botman, M., 1976, “Epicyclic Gear Vibrations,” *J. Eng. Ind.*, **98**(3), p. 811.
- [25] Lin, J., and Parker, R. G., 1999, “Analytical Characterization of the Unique

- Properties of Planetary Gear Free Vibration,” *J. Vib. Acoust.*, **121**(3), p. 316.
- [26] Ericson, T. M., and Parker, R. G., 2013, “Planetary Gear Modal Vibration Experiments and Correlation against Lumped-Parameter and Finite Element Models,” *J. Sound Vib.*, **332**(9), pp. 2350–2375.
- [27] Guo, Y., and Parker, R. G., 2010, “Purely Rotational Model and Vibration Modes of Compound Planetary Gears,” *Mech. Mach. Theory*, **45**(3), pp. 365–377.
- [28] Kahraman, A., 2001, “Free Torsional Vibration Characteristics of Compound Planetary Gear Sets,” *Mech. Mach. Theory*, **36**(8), pp. 953–971.
- [29] Kiracofe, D. R., and Parker, R. G., 2007, “Structured Vibration Modes of General Compound Planetary Gear Systems,” *Journal of Vibration and Acoustics*, p. 1.
- [30] Parker, R. G., and Lin, J., 2004, “Mesh Phasing Relationships in Planetary and Epicyclic Gears,” *J. Mech. Des.*, **126**(2), p. 365.
- [31] Parker, R. G., 2000, “A Physical Explanation for the Effectiveness of Planet Phasing To Suppress Planetary Gear Vibration,” *J. Sound Vib.*, **236**(4), pp. 561–573.
- [32] Kahraman, A., and Blankenship, G. W., 1994, “Planet Mesh Phasing in Epicyclic Gear Sets,” *Proceedings of the International Gearing Conference*, Newcastle, pp. 99–104.
- [33] Canchi, S. V., and Parker, R. G., 2008, “Effect of Ring-Planet Mesh Phasing and Contact Ratio on the Parametric Instabilities of a Planetary Gear Ring,” *J. Mech. Des.*, **130**(1), p. 014501.
- [34] Ambarisha, V. K., and Parker, R. G., 2006, “Suppression of Planet Mode Response in Planetary Gear Dynamics Through Mesh Phasing,” *J. Vib. Acoust.*, **128**(2), p. 133.
- [35] Kahraman, A., and Vijayakar, S., 2000, “Effect of Internal Gear Flexibility on the Quasi-Static Behavior of a Planetary Gear Set,” *J. Mech. Des.*, **123**(3), pp. 408–415.

- [36] Kahraman, A., Kharazi, A. A., and Umrani, M., 2003, “A Deformable Body Dynamic Analysis of Planetary Gears with Thin Rims [5],” *J. Sound Vib.*, **262**(3), pp. 752–768.
- [37] Abousleiman, V., and Velez, P., 2006, “A Hybrid 3D Finite Element/lumped Parameter Model for Quasi-Static and Dynamic Analyses of Planetary/epicyclic Gear Sets,” *Mech. Mach. Theory*, **41**(6), pp. 725–748.
- [38] Abousleiman, V., Velez, P., and Becquerelle, S., 2007, “Modeling of Spur and Helical Gear Planetary Drives With Flexible Ring Gears and Planet Carriers,” *J. Mech. Des.*, **129**(1), p. 95.
- [39] Chen, Z., Shao, Y., and Su, D., 2013, “Dynamic Simulation of Planetary Gear Set with Flexible Spur Ring Gear,” *J. Sound Vib.*, **332**(26), pp. 7191–7204.
- [40] Helsen, J., Marrant, B., Vanhollebeke, F., Coninck, F. De, Berckmans, D., Vandepitte, D., and Desmet, W., 2013, “Assessment of Excitation Mechanisms and Structural Flexibility Influence in Excitation Propagation in Multi-Megawatt Wind Turbine Gearboxes: Experiments and Flexible Multibody Model Optimization,” *Mech. Syst. Signal Process.*, **40**(1), pp. 114–135.
- [41] Helsen, J., Vanhollebeke, F., De Coninck, F., Vandepitte, D., and Desmet, W., 2011, “Insights in Wind Turbine Drive Train Dynamics Gathered by Validating Advanced Models on a Newly Developed 13.2 MW Dynamically Controlled Test-Rig,” *Mechatronics*, **21**(4), pp. 737–752.
- [42] Helsen, J., Vanhollebeke, F., Marrant, B., Vandepitte, D., and Desmet, W., 2011, “Multibody Modelling of Varying Complexity for Modal Behaviour Analysis of Wind Turbine Gearboxes,” *Renew. Energy*, **36**(11), pp. 3098–3113.
- [43] Tavakoli, M., and R. Houser, D., 1986, *Optimum Profile Modifications for the Minimization of Static Transmission Errors of Spur Gears*.
- [44] Fonseca, D. J., Shishoo, S., Lim, T. C., and Chen, D. S., 2005, “A Genetic Algorithm Approach to Minimize Transmission Error of Automotive Spur

- Gear Sets,” *Appl. Artif. Intell.*, **19**(2), pp. 153–179.
- [45] Yildirim, N., and Munro, R. G., 1999, “A Systematic Approach to Profile Relief Design of Low and High Contact Ratio Spur Gears,” *Proc. Inst. Mech. Eng. Part C J. Mech. Eng. Sci.*, **213**(March 1998), pp. 551–562.
- [46] Vexlex, P., Bruyère, J., and Houser, D. R., 2011, “Some Analytical Results on Transmission Errors in Narrow-Faced Spur and Helical Gears: Influence of Profile Modifications,” *J. Mech. Des.*, **133**(3), p. 031010.
- [47] Kahraman, A., and Blankenship, G. W., 1999, “Effect of Involute Tip Relief on Dynamic Response of Spur Gear Pairs,” *J. Mech. Des.*, **121**(2), p. 313.
- [48] Hotait, M. A., and Kahraman, A., 2013, “Experiments on the Relationship between the Dynamic Transmission Error and the Dynamic Stress Factor of Spur Gear Pairs,” *Mech. Mach. Theory*, **70**, pp. 116–128.
- [49] Bonori, G., Barbieri, M., and Pellicano, F., 2008, “Optimum Profile Modifications of Spur Gears by Means of Genetic Algorithms,” *J. Sound Vib.*, **313**(3-5), pp. 603–616.
- [50] Faggioni, M., Samani, F. S., Bertacchi, G., and Pellicano, F., 2011, “Dynamic Optimization of Spur Gears,” *Mech. Mach. Theory*, **46**(4), pp. 544–557.
- [51] Bahk, C.-J., and Parker, R. G., 2013, “Analytical Investigation of Tooth Profile Modification Effects on Planetary Gear Dynamics,” *Mech. Mach. Theory*, **70**, pp. 298–319.
- [52] Cigeroglu, E., and Samandari, H., 2012, “Nonlinear Free Vibration of Double Walled Carbon Nanotubes by Using Describing Function Method with Multiple Trial Functions,” *Phys. E Low-Dimensional Syst. Nanostructures*, **46**, pp. 160–173.
- [53] Yümer, M. E., Cigeroğlu, E., and Özgüven, H. N., 2010, “Non-Linear Forced Response Analysis of Mistuned Bladed Disk Assemblies,” *Vol. 6 Struct. Dyn. Parts A B*, (June), pp. 757–766.
- [54] Von Groll, G., and Ewins, D. J., 2001, “The Harmonic Balance Method with Arc-Length Continuation in Rotor/stator Contact Problems,” *J. Sound Vib.*,

- 241**(2), pp. 223–233.
- [55] Yuksel, C., and Kahraman, a., 2004, “Dynamic Tooth Loads of Planetary Gear Sets Having Tooth Profile Wear,” *Mech. Mach. Theory*, **39**(7), pp. 695–715.
- [56] Shen, Y., Yang, S., and Liu, X., 2006, “Nonlinear Dynamics of a Spur Gear Pair with Time-Varying Stiffness and Backlash Based on Incremental Harmonic Balance Method,” *Int. J. Mech. Sci.*, **48**, pp. 1256–1263.
- [57] Kahraman, A., and Singh, R., 1990, “Non-Linear Dynamics of a Spur Gear Pair,” *J. Sound Vib.*, **142**(1), pp. 49–75.
- [58] Gasmi, A., Joseph, P. F., Rhyne, T. B., and Cron, S. M., 2011, “Closed-Form Solution of a Shear Deformable, Extensional Ring in Contact between Two Rigid Surfaces,” *Int. J. Solids Struct.*, **48**(5), pp. 843–853.
- [59] Özgüven, H. N., and Houser, D. R., 1988, “Mathematical Models Used in Gear Dynamics—A Review,” *J. Sound Vib.*, **121**(3), pp. 383–411.
- [60] Wang, J., Li, R., and Peng, X., 2003, “Survey of Nonlinear Vibration of Gear Transmission Systems,” *Appl. Mech. Rev.*, **56**(3), p. 309.
- [61] Özgüven, H. N., and Houser, D. R., 1988, “Dynamic Analysis of High Speed Gears By Using Loaded Static Transmission Error,” *J. Sound Vib.*, **125**(1), pp. 71–83.
- [62] Maliha, R., Doğruer, C. U., and Ozguven, H. N., 2004, “Nonlinear Dynamic Modeling of Gear-Shaft-Disk-Bearing Systems Using Finite Elements and Describing Functions,” *J. Mech. Des.*, **126**, pp. 534–541.
- [63] Kahraman, a., Ligata, H., and Singh, a., 2010, “Influence of Ring Gear Rim Thickness on Planetary Gear Set Behavior,” *J. Mech. Des.*, **132**(2), p. 021002.
- [64] Kramberger, J., Šraml, M., Glodež, S., Flašker, J., and Potrč, I., 2004, “Computational Model for the Analysis of Bending Fatigue in Gears,” *Comput. Struct.*, **82**(23-26), pp. 2261–2269.
- [65] Lee Y., Pan J., H. R. B., 2005, *Fatigue Testing and Analyses*.
- [66] American Gear Manufactures Association, 2004, “ANSI/AGMA 2001-D04

Fundamental Rating Factors and Calculation Methods for Involute Spur and Helical Gear Teeth,” **04**, p. 66.

- [67] Harianto J., 1995, “The Effect of Manufacturing Errors on Predicted Dynamic Factors of Spur Gears,” Ohio State University.
- [68] Lin, H. H., Townsend, D. P., and Oswald, F. B., 1988, “Profile Modification to Minimize Spur Gear Dynamic Loading,” Des. Eng. Tech. Conf. Spons. by Am. Soc. Mech. Eng., pp. 24–28.
- [69] K. Tamminana, V., Kahraman, A., and Vijayakar, S., 2007, *A Study of the Relationship Between the Dynamic Factors and the Dynamic Transmission Error of Spur Gear Pairs*.
- [70] Vijayakar, S., 1991, “A Combined Surface Integral and Finite Element Solution for a Three Dimensional Contact Problem,” Int. J. Numer. Methods Eng., **31**(May 1990), pp. 525–545.
- [71] Parker, R. G., Agashe, V., and Vijayakar, S. M., 2000, “Dynamic Response of a Planetary Gear System Using a Finite Element / Contact Mechanics,” J. Mech. Des., **122**(September), pp. 304–310.
- [72] Chen, Z., Shao, Y., and Su, D., 2013, “Dynamic Simulation of Planetary Gear Set with Flexible Spur Ring Gear,” J. Sound Vib., **332**(26), pp. 7191–7204.
- [73] Parker, R. G., 2000, “A Physical Explanation for the Effectiveness of Planet Phasing To Suppress Planetary Gear Vibration,” J. Sound Vib., **236**(4), pp. 561–573.
- [74] Yildirim, N., and Munro, R. G., 1999, “A New Type of Profile Relief for High Contact Ratio Spur Gears,” Proc. Inst. Mech. Eng. Part C J. Mech. Eng. Sci., **213**(March 1998), pp. 563–568.
- [75] Yildirim, N., Gasparini, G., and Sartori, S., 2008, “An Improvement on Helicopter Transmission Performance through Use of High Contact Ratio Spur Gears with Suitable Profile Modification Design,” Proc. Inst. Mech. Eng. Part G J. Aerosp. Eng., **222**(8), pp. 1193–1210.
- [76] Ozturk, V. Y., Cigeroglu, E., and Özgüven, H. N., 2014, “Optimum Profile

Modifications for the Minimization of Dynamic Transmission Error,” *International Gear Conference 2014*, Woodhead Publishing Limited, pp. 596–605.

- [77] Yavuz, S. D., Saribay, Z. B., and Cigeroglu, E., 2018, “Nonlinear Time-Varying Dynamic Analysis of a Spiral Bevel Geared System,” *Nonlinear Dyn.*, pp. 1–19.
- [78] Ferhatoglu, E., Cigeroglu, E., and Özgüven, H. N., 2018, “A New Modal Superposition Method for Nonlinear Vibration Analysis of Structures Using Hybrid Mode Shapes,” *Mech. Syst. Signal Process.*, **107**, pp. 317–342.

APPENDIX A

PUBLISHED PAPERS DURING PHD

Proceedings of the ASME 2015 International Design Engineering Technical Conferences &
Computers and Information in Engineering Conference
IDETC/CIE 2015
August 2-5, 2015, Boston, Massachusetts, USA

DETC2015-47136

Optimization of Tooth Bending Fatigue Characteristics of Spur Gear Pairs using a Gear Dynamics-based Approach

Yalın Öztürk
Turkish Aerospace Industries
Helicopters Group
Ankara, Turkey
yalozturk@tai.com.tr

Ender Ciğeroğlu
Middle East Technical University
Mechanical Engineering
Department
Ankara, Turkey
ender@metu.edu.tr

H. Nevzat Özgüven
Middle East Technical University
Mechanical Engineering
Department
Ankara, Turkey
ozguven@metu.edu.tr

ABSTRACT

A gear tooth profile optimization study is performed with the target being defined as the maximization of tooth bending fatigue life for a selected operational range, where the operating torque and speed ranges are defined along with their corresponding durations. For this purpose, a nonlinear lumped gear dynamics model is combined with the S/N curve of the gear material in order to estimate tooth bending fatigue life of the spur gear pair. The differences between the predicted lives of the optimally modified and non-modified gear pairs are presented based on example spur gear pairs. The proposed tooth bending fatigue life estimation is compared with the standard AGMA procedure.

INTRODUCTION

Fatigue life of a gear pair is usually one of the greatest concerns for the gear designer since an unexpected failure in such components would typically lead to loss of power and motion transmission, results of which can be catastrophic. One of the most common gear failure mechanisms is the gear tooth bending fatigue failure, which would stop the operation of power and motion transmission immediately.

Although in the literature there exists a large number of theories in fatigue field, those are yet to be fully adapted to the case hardened materials, like gears. Having stated that, tooth bending fatigue problem is relatively easier than the tooth contact fatigue problem since it is not dependent on lubrication or surface roughness. In a general gear bending fatigue problem, stress levels are expected to be relatively low such that plastic deformation is not expected for properly manufactured gears. Then, using the stress-life (S-N) approach is considered to be appropriate. The common approach to find

an endurance limit, below which no fatigue failure occurs, is widely disputed [1], as many engineering materials, including high strength steels, may not have such a limit. Strain-life approach for estimation of the fatigue lives of gears is also employed by several researchers. Glodez et al. [2] employed the strain-life based Coffin-Manson relation to model the crack initiation phase of spur gears; for the prediction of the crack propagation life, a linear elastic fracture mechanics (LEFM) approach is employed.

Many parameters such as gear root geometry, load distribution along the teeth, material properties, residual stresses etc. have been identified which could affect the bending fatigue lives of gears. Besides those, depending on the application and operation conditions (speeds and loads), certain measures can be of great help in order to improve the bending fatigue characteristics of a gear pair. A more direct approach to gear tooth bending fatigue, in which both the magnitude and number of occurrence of bending stress cycles are considered, is possible by bridging the gear dynamics with operational spectrum (in terms of load and speed) data. It is common practice in gear industry to employ profile modifications in micro-scale in order to both reduce the noise transmitted by the geared system and to improve the fatigue characteristics of the gear pair. Studies have shown that with proper profile modifications, dynamic factors which can be thought as the ratio of tooth loads (or bending moments at the root) in dynamic condition to those values obtained at static condition can be minimized.

Harianto [3] calculated several dynamic factors based on different dynamic factor definitions, both for the gears with modified and non-modified tooth profiles. He concluded that deviations from optimal profile modifications often exceed the

Y. Öztürk , E. Ciğeroğlu and H. N. Özgüven “Optimization of Tooth Bending Fatigue Characteristics of Spur Gear Pairs using a Gear Dynamics-based Approach,” in ASME 2015 International Design Engineering Technical Conferences, 2015.

AGMA recommendations of dynamic factor for non-optimal modification gear.

Another possible positive effect of a proper profile modification, which is disregarded most of the time, is that it can reduce the number of bending stress cycles that the gear pair is subjected to during its normal operation. Depending on the operation speeds, this effect may even be more dominant than the reduction of the dynamic factors. Hotait et al. [4] showed experimentally that there is a linear relationship between the dynamic factor and dynamic transmission error (DTE) data such that one can be estimated by using the measurement of the other. In his experimental work, it is also possible to see that at some operating speeds, number of stress cycles at the root is greater than one for a given single mesh cycle.

Having stated that it is possible to improve the bending fatigue characteristics of gear pairs by proper modifications, the importance of finding an optimal profile modification scheme, which can function efficiently for given torque and speed values, has to be underlined. Loaded static transmission error (LSTE) optimization efforts go back to the study of Tavakoli and Houser in 1986 [5]. In their study, an objective function based on the mean value of the transmission error harmonics under different design torques was used in search of optimal tooth profile. In 2005, Fonseca et al. [6] employed a genetic optimization algorithm to the same static model of Tavakoli and Houser [5]. These studies reveal that optimization efforts based on LSTE fluctuation minimization are very effective when torque is the only parameter considered regarding the operational characteristics of gear pairs.

Further improvement towards reducing actual vibration levels can be achieved via optimization efforts targeted at DTE minimization. Bonori et al. [7] performed dynamic analyses to check the quality of their genetic algorithm based LSTE optimization method. In 2011, Faggioni et al. [8] developed an optimization model with 8 parameters and concluded that optimization which is directly targeted minimizing DTE produced better results than an optimization study which aims to minimize LSTE. Most recently in 2014, Ozturk et al. [9] showed that for some cases employing a DTE-minimization on top of a multi-degree of freedom (MDoF) dynamic model is necessary to avoid misleading results that can be obtained otherwise with LSTE minimization using a single-degree of freedom (SDoF) dynamics model.

In this study, a tooth bending fatigue life estimation procedure which is based on gear dynamics will be presented. A single-degree of freedom model is preferred in this study for its simplicity, although such a model will be insufficient for the cases where the compliances of the other elements of the drive system cannot be neglected. The procedure will be explained in detail with an example spur gear pair which is made of high strength alloy steel 42CrMo6. A tooth profile optimization study will be performed aimed at achieving the maximum tooth bending life for the example gear pair, taking the operational spectrum into account. Tooth root stress cycles will be calculated based on a SDoF nonlinear gear dynamics model

using rainflow counting method. Those stress values will be input to the fatigue model which is based on the S/N curve of the gear pair material.

GEAR DYNAMICS MODEL USED FOR TOOTH BENDING FATIGUE OPTIMIZATION

There exists a variety of gear dynamics models in the literature, which can be categorized under many different groups. A comprehensive review of gear dynamics models can be found in the study of Özgüven and Houser [10], and more recently it is given by Wang et al. [11].

In the current study, first, the model proposed by Özgüven and Houser in 1988 [12] is used in optimization. This model is based on a validated approximation, which uses LSTE rather than static transmission itself, as an excitation to a SDoF model with average constant mesh stiffness. The linear equation of motion of a gear pair is given in terms of dynamic transmission error, x , as:

$$m_e \ddot{x}(t) + 2\zeta \sqrt{m_e k_{ave}} \dot{x}(t) + k_{ave} x(t) = k_{ave} x_s(t) \quad (1)$$

Here m_e is the equivalent mass of the gear pair, ζ is the viscous damping ratio, k_{ave} is the average mesh stiffness and x_s is the loaded static transmission error. It was concluded that the displacement excitation resulting from time varying mesh stiffness is more important than the change in the system natural frequency resulting from the mesh stiffness variation [12]. This model was shown to be a very effective one by using experimental results for gear pairs that have no profile modification. Moreover, recently, Ozturk et al. [9] showed that the model provides a good level of accuracy even for the cases where the resulting LSTE variation (hence the dynamic excitation) is at very low levels. The nonlinear version of this model is used throughout this study, where the nonlinearity due to the backlash between the mating gears is also considered. The nonlinear equation is solved in time domain using a 4th-5th order Runge-Kutta integration. LSTE and average mesh stiffness values are supplied to the dynamic model by using the computer code STEP (Spur Gear Transmission Error Program) developed at the Ohio State University. Using STEP, it is also possible to obtain static load distribution solutions for modified tooth profiles.

The dynamic model will be used to obtain dynamic root stresses, resulting from dynamic mesh forces. The equation for dynamic mesh force (in case of no tooth separation) is given in [12] as follows:

$$W(t) = W_0 + k_{ave}(x(t) - x_s(t)) + 2\zeta \sqrt{m_e k_{ave}} \dot{x}(t) \quad (2)$$

Here W_0 is the static load. Along with the LSTE and average mesh stiffness input, the moment arm (with respect to root of the gears) information is also gathered from STEP, enabling to obtain stress numbers, which are simply the multiplication of mesh forces with the respective moment arms. The real stress values are obtained through a correlation of stress numbers with

the static stress results obtained through WindowsLDP of OSU, which is capable of employing finite element formulation for the calculation of root stresses. With this approach, it is aimed to achieve as realistic a stress calculation as possible.

The dynamic root stress data is then directed to the rainflow counting algorithm, in order to extract stress cycle information, which, along with the rpm and duration of the operating condition data, is used in life estimation analysis.

FATIGUE MODEL FOR TOOTH BENDING LIFE ESTIMATION

Gears in most applications are subject to relatively low stress levels, so that in comparison to crack propagation period, most of the fatigue life is spent in the crack initiation phase. Therefore, the stress-life (S-N) approach can be considered as an appropriate method of predicting bending fatigue life of gears.

Although in a traditional S-N curve, it is assumed that below a certain level of stress (endurance limit), no fatigue damage occurs, existence of such a limit is widely questioned for most of the engineering materials, including the steels used in gearing industry. For this reason, a two-slope S-N curve [13] is used to capture the damage in regions both above and below the fatigue limit separately.

Following equations can be used for stress values above and below the fatigue limit respectively:

$$N_i = N_{FL} \left(\frac{\Delta\sigma}{\Delta\sigma_{FL}} \right)^{\frac{1}{b}}, \Delta\sigma > \Delta\sigma_{FL} \quad (3)$$

$$N_i = N_{FL} \left(\frac{\Delta\sigma}{\Delta\sigma_{FL}} \right)^{\frac{2}{b}+1}, \Delta\sigma < \Delta\sigma_{FL} \quad (4)$$

In these equations, N_{FL} stands for the number of cycles at the endurance limit $\Delta\sigma_{FL}$, $\Delta\sigma$ is the applied stress level and b is the slope of the S-N curve in the region where the stresses are above the endurance limit, in log-log scale. These are the general S-N curve equations which can be employed to many engineering materials, including steel, with the constants varying for each different material. In this study, 42CrMo6 is selected as the gear material and the required parameters are taken from [2]. Table 1 shows those parameters:

Table 1. S-N CURVE PROPERTIES FOR 42CrMo6

Material	$\Delta\sigma_{FL}$	N_{FL}	b
42CrMo6	550	3e6	-0.0816

Rainflow ranges have been widely used for estimating fatigue damage from variable amplitude loading. Rainflow cycle counting method is based on the analogy of raindrops falling on a pagoda roof and running down the edges of the roof. As per the SAE and the ASTM standards, the three-point cycle counting rule uses three consecutive points in a load-time history to determine whether a cycle is formed. Details of

rainflow counting algorithm used in this study can be found in [14].

For this study, the stress-time history data is run through a three-point rainflow cycle counting algorithm and stress cycles are extracted. Respective damage for the operating duty cycle under consideration is then calculated using the material S/N curve by implementation of Miner's rule for damage accumulation.

PROCEDURE FOR TOOTH BENDING FATIGUE LIFE ESTIMATION

The procedure proposed in this study for estimating the tooth bending fatigue life for a spur gear pair is a combination of the previously mentioned gear dynamics model and the fatigue model. This procedure is shown in Figure 1.

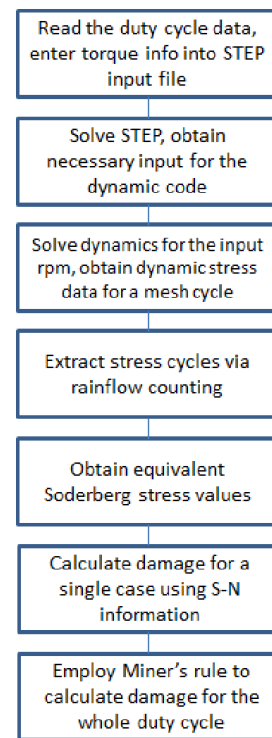


Figure 1. PROCEDURE FOR GEAR TOOTH BENDING LIFE ESTIMATION

The procedure is explained below in detail for a sample spur gear pair with a defined duty cycle.

Example

The tooth bending fatigue life is going to be estimated for the following gear pair (Table 2). The gear pair under consideration consists of 2 identical spur gears. Tooth profiles are non-modified. The damping ratio is taken as 0.05 since it is used in many gear dynamics modeling studies including [12].

Table 2. EXAMPLE SPUR GEAR PAIR

Number of teeth	50
Module	3 mm
Equivalent mass	0.7824 kg
Base diameter	140.95 mm
Tip diameter	153.74 mm
Center distance	150 mm
Damping ratio	0.05

When the operating speeds are near the natural frequency of the gear pair system, or correspond to those levels at which the system can be excited by the higher harmonics of the excitation due to the LSTE, the dynamic effects can become dominant and hence a dynamic response analysis becomes a necessity. The tooth bending life of this spur gear pair is going to be estimated for the given duty cycle (Table 3). Note that the duty-cycle given in Table 3 may as well be interpreted as a portion of a total duty cycle which only contains the critical intervals regarding the fatigue life.

Table 3. DUTY CYCLE UNDER CONSIDERATION

Case	Torque [Nm]	Speed [rpm]	Duration [hours]
1	550	1160	400
2	600	1240	40
3	730	940	80
4	600	1140	200
5	600	1850	20

The steady state normal tooth bending stress results for the different cases of the duty cycle are shown in Figure 2. The assumption of a uniaxial stress state is reasonable because of the geometry and the loading characteristic of a spur gear. The static case when a torque of 600Nm is applied is also given for comparison as Case 0:

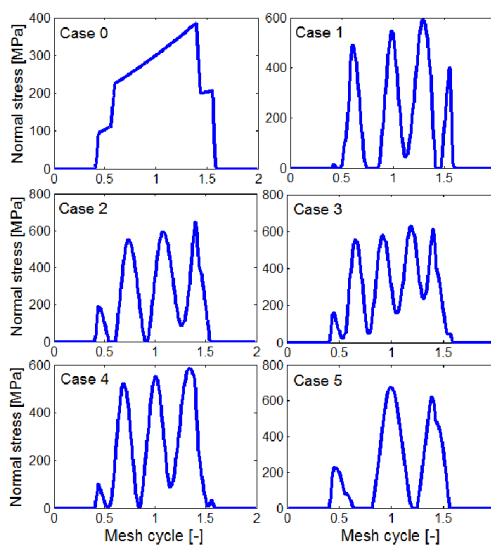


Figure 2. TOOTH ROOT NORMAL STRESS RESULTS

As expected, the dynamic stress results show a more complex behavior than that of the static case. Not only the peak stress levels go higher, but also the number of stress cycles which can be effective in damaging of the teeth increases. One can also observe the loss of contact phenomenon in Case 1 and Case 5, where the root stress levels drop to 0. The stress cycles are extracted with the Rainflow counting method. Table 4 shows the stress cycles for Case 3. Note that here the minor cycles (i.e. cycles with very low stress ranges) are not shown.

Table 4. RAINFLOW STRESS CYCLES FOR CASE 3

No. of cycles	From [MPa]	To [MPa]	Range [MPa]	Mean [MPa]	Equivalent Soderberg Stress [MPa]
1	237	613	376	425	359
1	556	50	506	303	383
1	580	160	420	370	359
1	629	0	629	314.5	486

The last column in Table 4 shows the equivalent Soderberg stress values. The following operation is used in order to compensate for the tensile mean stress effects on high-cycle fatigue strength. Note that other stress correction methods can also be employed at this step.

$$S_{ar} = \frac{S_a}{1 - \frac{S_m}{S_y}} \quad (5)$$

In this equation S_{ar} is the fully-reversed stress amplitude, S_a is the stress amplitude, S_m is the mean stress level and S_y is the yield strength of the material. The Soderberg stress values are entered into the S/N curve equation along with the rpm and duration information in order to check if the gear pair can survive in the projected lifetime. Table 5 shows the damages related to the respective cases.

Table 5. FATIGUE LIVE SUMMARY FOR THE GEAR PAIR

Case	Cycles	Cycles to fail	Damage [%]
1	2.78e7	5.00e8	5.5
2	2.98e6	1.94e7	15.4
3	4.51e6	5.52e7	8.2
4	1.37e7	6.66e8	2.1
5	2.22e6	3.96e6	56.1
Total	-	-	87.3

Comparison with the AGMA approach

Although a direct comparison with the fatigue calculation concept in AGMA standard is not possible, it is safe to say that AGMA does not consider the mentioned effect of secondary stress cycles due to dynamic effects. AGMA considers the cyclic nature of loading in the factor Y_N , stress cycle factor for bending strength [15]. However calculation of this factor does not take into account the possibility of having more than one stress cycle during a single mesh cycle, as the formula for the number of stress cycles (N) is given as:

$$N = 60 L n q \quad (6)$$

Here L is life in hours, n is rpm and q is number of contacts per revolution. AGMA gives several S/N charts for finding Y_N , which is used in calculating an allowable bending stress number.

AGMA also employs a dynamic factor, K_v , in order to account for the dynamic loading. Studies [3] have shown that deviations from optimal profile modifications often exceed the AGMA recommendations of dynamic factor for gears with non-optimal modification. With this information, one can modify the dynamic factor to be used by using a gear-dynamics model. However even this updated factor may not be enough to cover all the dynamic effects in a fatigue calculation.

Consider the case shown below obtained at 620 Nm torque at 1155 rpm:

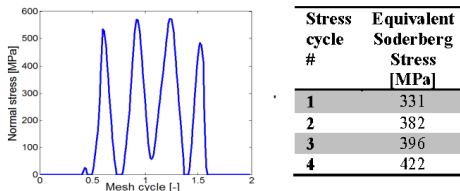


Figure 3. STRESS CYCLE INFORMATION FOR THE SAMPLE CASE

Note that the gear pair is the same gear pair that was investigated in the previous section. Table 6 gives the expected fatigue damage information for this case, using the S/N curve for 42CrMo6. The number of cycles to fail is highlighted for the peak stress and for the total stress time history.

Table 6. CYCLES TO FAIL FOR THE RESPECTIVE STRESS CYCLES

Stress cycle	# of cycles to fail
1	4.61e11
2	1.59e10
3	6.80e9
4	1.52e9
Total mesh cycle	1.15e9

It can be clearly observed from Table 6 that the omission of stress cycles with smaller ranges (secondary stress cycles) can lead to a miscalculation regarding the lifetime of the gear pair. One should also consider that there may be even cases which are more critical in terms of fatigue damage estimations than the case shown in this example. The fatigue properties of the material and the severity of the loading usually determine the level of the effect of the secondary stress cycles.

Although in most applications gear designers can end up with safe designs by using the conventional dynamic factor and stress cycle factor approach, it should be kept in mind that for some specific speed and torque levels, the secondary stress cycles can also affect the tooth bending life of the gear pair.

BENDING FATIGUE LIFE OPTIMIZATION USING PROFILE MODIFICATIONS

Profile modifications are known to be very effective in reducing the vibration and noise in spur gears, since, when properly applied, they reduce the dynamic excitation to the geared system, in terms of loaded static transmission error (LSTE). This mentioned reduction of the dynamic loading of the system also means an improvement in both bending and contact fatigue lives.

There have been many studies, both theoretical and experimental, showing the improvement in dynamic load factors after the employment of proper profile modifications [3, 16].

In this study an optimization scheme which, instead of obtaining minimum dynamic load factors, is directly targeted at obtaining the maximum tooth bending fatigue life for a spur gear pair is suggested. Studies [8, 9] have shown that DTE minimization based optimization work can lead to better results than those based on LSTE minimization, so a similar approach is followed here regarding the tooth bending fatigue lives. A comparison with LSTE optimization is not in the scope of this work.

A 4-parameter optimization model is used here, the variables being amount of tip modification and the start of the modification both for the pinion and the gear. A brute-force

optimization technique is employed. The gear pair used in the optimization model is the same as the one used throughout this study. The optimization scheme can be applied on different duty cycles; here an example is given for the duty cycle in Table 3.

Table 7 shows the results of the optimization study for various arbitrary profile modification scenarios, including the optimum one for tooth bending fatigue life. Note that a case with a life estimation which is worse than the no profile modification case is also shown.

Table 7. DAMAGE SUMMARIES OBTAINED FOR DIFFERENT PARAMETER CONFIGURATIONS

Profile Modification (PM)	Pinion PM Amount [μm]	Pinion PM Start [$^{\circ}\text{RA}$]	Gear PM Amount [μm]	Gear PM Start [$^{\circ}\text{RA}$]	Damage [%]
No PM	-	-	-	-	87.3
1	25	24.6	25	24.3	42.7
2	28	24	25	24.6	1.0
3	31	24.6	28	24	14.8
4	31	24.6	31	24	4.6
5	28	24.6	31	24.6	271.7
Best PM	28	24	31	24	0.0012

As can be observed from Table 7, when combined with the nature of the fatigue characteristics for the steel, an optimum profile modification can easily guarantee the safe operation of a spur gear pair throughout its lifecycle, when tooth bending fatigue is the only concern. Another important outcome of this study is that, a bad selection for the profile modification can endanger the gear pair, making a premature failure possible such that even an unmodified gear pair behaves better tooth bending fatigue-wise. Small variations in the optimization parameters tend to change the fatigue characteristics very dramatically, which underlines the importance of selection of the objective function as maximization of fatigue life, instead of a LSTE minimization.

The steady state stress cycle information for the duty cycle given in Table 3 is given in Figure 4 for the optimum profile modification case.

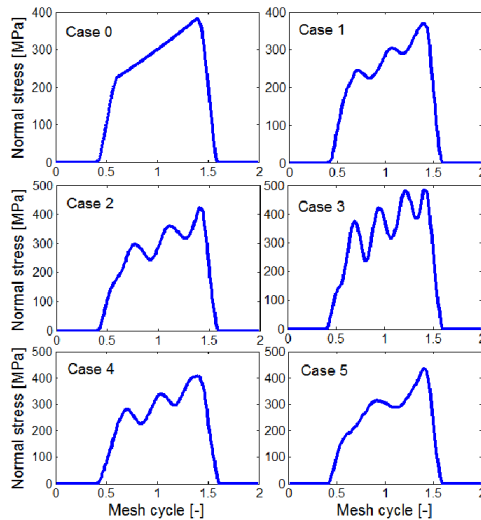


Figure 4. TOOTH ROOT NORMAL STRESS TIME HISTORIES FOR THE OPTIMAL PM CONFIGURATION

With the application of the optimal profile modification, not only the stress-based dynamic factors reduce, but also the secondary stress cycles decrease to such levels that they can be neglected in bending fatigue life calculations. Therefore in terms of improving the tooth bending fatigue life, the effect of a good profile modification is not limited to reduction of the maximum stress at the root region.

CONCLUSIONS

In this study, a procedure to estimate the tooth bending fatigue lives of spur gear pairs is explained. A SDoF gear dynamics model is incorporated into the life estimation model in order to get more accurate stress cycles at the actual operating scenarios. This procedure is then employed in a 4-parameter profile modification optimization study where the target is to obtain maximum tooth bending fatigue life for an example spur gear pair with a pre-defined duty cycle.

The relatively low bending stress levels expected at the root region of spur gears make it appropriate to apply HCF theory for fatigue life estimation. A 2-slope S-N curve is used here in order not to neglect the stresses below the fatigue limit. Soderberg equation is used to take into account the effects of mean tensile stresses. For calculating the accumulation of the damage during a duty cycle, Miner's rule is preferred.

The dynamic stress plots show that depending on the operation speed, it is possible to observe more than one stress cycle which can be effective in damaging of the gears when tooth bending fatigue is considered. A 3-point rainflow

counting algorithm is employed for detecting the stress cycles during a single gear mesh period.

When a safety analysis is performed for a gear pair, the common approach is to apply certain factors in order to compensate for the dynamic nature of loading and stress cycles. The calculations can further be improved by the replacement of dynamic factors stated in gearing standards (AGMA, ISO, DIN) by more accurate ones based on a dynamic analysis. However the effect of secondary stress cycles can still get neglected with such an approach, misleading to overestimated bending fatigue lives. A more accurate life estimation is possible using the procedure explained in this study.

A proper tip modification design is sought for both of the mating gears by optimizing the modification parameters, i.e. start and magnitude of the tip reliefs. When the overall solution domain is investigated, the sensitivity of the fatigue life estimations turns out to be quite high. With a properly optimized tip relief, it is possible to get rid of the adverse dynamic effects hence obtain life estimations which practically guarantee a safe operation throughout the whole life cycle of the gear pair. On the other hand, an improper profile modification (even with slightly different parameters) could lead to a premature failure of the gear pair. The stress plots for the best profile modification scenario are also investigated using the example gear pair. It is observed that not only the dynamic stress factors reduce but also the secondary stress cycles disappear.

REFERENCES

- [1] Singh, A., (2000), An experimental investigation of bending fatigue initiation and propagation lives, ASME 2000 Design Engineering Technical Conferences and Computers and Information in Engineering Conferences, Baltimore, Maryland.
- [2] Glodez, S., Sraml, M., and Kramberger, J., (2002), A computational model for determination of service life of gears, *International Journal of Fatigue*, 24, (10) 1013-1020.
- [3] Harianto J., (1995), The effect of manufacturing errors on predicted dynamic factors of spur gears, M.Sc. Thesis, The Ohio State University.
- [4] Hotait M.A., Kahraman A., (2013), Experiments on the relationship between the dynamic transmission error and the dynamic stress factor of spur gear pairs, *Mechanism and Machine Theory*, 70, 116–128.
- [5] Tavakoli M.S., Houser D.R. (1986), Optimum profile modifications for the minimization of static transmission errors of spur gears, *Journal of Mechanism Transmissions and Automation in Design*, **108**, 86–95.
- [6] Fonseca D.J., Shishoo S., Lim T.C., Chen D.S. (2005), A genetic algorithm approach to minimize transmission error of automotive spur gears sets, *Applied Artificial Intelligence*, 19, 2, 153–179.
- [7] Bonori G., Barbieri M., Pellicano F. (2008), Optimum profile modifications of spur gears by means of genetic algorithms, *Journal of Sound and Vibration*, 313, 603–616.
- [8] Faggioni M., Samani F. S., Bertacchi G. Pellicano F. (2011), Dynamic optimization of spur gears, *Mechanism and Machine Theory*, **46**, 544–557.
- [9] Ozturk V. Y., Cigeroglu E., Özgüven H. N., (2014), Optimum profile modifications for the minimization of dynamic transmission error, *International Gear Conference*, Lyon, France.
- [10] Özgüven H.N., Houser D.R. (1988), Mathematical models used in gear dynamics - A review, *Journal of Sound and Vibration*, **121**, 3, 383–411.
- [11] Wang J., Li R., Peng X. (2003), Survey of nonlinear vibration of gear transmission systems, *Applied Mechanics Rev.*, **56**, 3, 309-329.
- [12] Özgüven H. N., Houser D. R. (1988), Dynamic analysis of high speed gears by using loaded static transmission error, *Journal of Sound and Vibration*, **125**, 71–83.
- [13] Ligata H., (2007), Impact of system level factors on planetary gear set behavior, Ph.D. Thesis, The Ohio State University.
- [14] Lee Y., Pan J., Hathaway R.B., Barkey M.E. (2005), *Fatigue testing and analysis*, Elsevier.
- [15] ANSI/AGMA 2001-D04, (2004), *Fundamental Rating Factors and Calculation Methods for Involute Spur and Helical Gear Teeth*, American Gear Manufacturers association.
- [16] Lin H. H., Townsend D. P., Oswald F. B., (1988), Profile modification to minimize spur gear dynamic loading, ASME Design Engineering Technical Conference, Orlando, Florida.

Optimum profile modifications for the minimization of dynamic transmission error

V.Y. Ozturk^{1,2}, E. Cigeroglu¹, H.N. Özgüven¹

Middle East Technical University, Mechanical Engineering Department, Turkey
Turkish Aerospace Industries, Turkey

An optimization study is performed target being the reduction of dynamic transmission error (DTE) for a selected operational range, where the operating torque and speed ranges are defined. For this purpose, two different models, i.e. a single degree of freedom (SDOF) lumped gear dynamics model and a multi-degree of freedom (MDOF) lumped model of a gear pair which is combined with shaft and bearing dynamics are employed. The differences between the optimization results obtained through loaded static transmission error (LSTE) minimization and DTE minimization using different models are presented based on example spur gear pairs.

1 INTRODUCTION

Reduction of vibration and noise is mostly achieved by proper tooth profile modifications in geared systems. Generally, minimization of the peak-to-peak values of loaded static transmission error (LSTE) is found to be “effective enough” in eliminating the vibration-based problems. Since it is not possible to have a profile modification on gear teeth which will minimize LSTE variation at all loads, usually a further optimization effort is necessary to find the optimum profile modification which will give the “best” result for a drive system operating under different torque levels throughout its operational life.

LSTE optimization efforts go back to the study of Tavakoli and Houser in 1986 (1). In their study, an objective function based on the mean value of the transmission error harmonics under different design torques was used in search of optimal tooth profile. In 2005, Fonseca *et al.* (2) employed a genetic optimization algorithm to the same static model of Tavakoli and Houser (1). These studies reveal that optimization efforts based on LSTE fluctuation minimization are very effective when torque is the only parameter considered regarding the operational characteristics of gear pairs.

Further improvement towards reducing actual vibration levels can be achieved via optimization efforts targeted at DTE minimization. Bonori *et al.* (3) performed dynamic analyses to check the quality of their genetic algorithm based LSTE optimization method. Recently in 2011, Faggioni *et al.* (4) developed an optimization model with 8 parameters and concluded that optimization which is directly targeted minimizing DTE produced better results than an optimization study which aims to minimize LSTE.

In the this study, a MDOF model is also employed along with a SDOF model in order to investigate the differences between optimization results obtained by using different models. The objective in the optimization is set as reducing the peak-to-peak

stress cycles are considered, is possible by bridging the gear dynamics with operational spectrum (in terms of load and speed) data. It is common practice in gear industry to employ profile modifications in micro-scale in order to both reduce the noise transmitted by the geared system and to improve the fatigue characteristics of the gear pair. Studies have shown that with proper profile modifications, dynamic factors which can be thought as the ratio of tooth loads (or bending moments at the root) in dynamic condition to those values obtained at static condition can be minimized.

Harianto [3] calculated several dynamic factors based on different dynamic factor definitions. He concluded that deviations from optimal profile modifications often exceed the AGMA recommendations of dynamic factor for non-optimal modification gear. Hotait et al. [4] showed experimentally that there is a linear relationship between the dynamic factor and dynamic transmission error data such that one can be estimated by using the measurement of the other. In his experimental work, it is also possible to see that at some operating speeds, number of stress cycles at the root is greater than one for a given single mesh cycle.

Another possible positive effect of a proper profile modification, which is disregarded most of the time, is that it can reduce the number of bending stress cycles that the gear pair is subjected to during its normal operation. Depending on the operation speeds, this effect may even be more dominant than the reduction of the dynamic factors.

LSTE optimization efforts go back to the study of Tavakoli and Houser in 1986 (1). In their study, an objective function based on the mean value of the transmission error harmonics under different design torques was used in search of optimal tooth profile. In 2005, Fonseca *et al.* (2) employed a genetic optimization algorithm to the same static model of Tavakoli and Houser (1). These studies reveal that optimization efforts based on LSTE fluctuation minimization are very effective when torque is the only parameter considered regarding the operational characteristics of gear pairs.

Further improvement towards reducing actual vibration levels can be achieved via optimization efforts targeted at DTE minimization. Bonori *et al.* (3) performed dynamic analyses to check the quality of their genetic algorithm based LSTE optimization method. Recently in 2011, Faggioni *et al.* (4) developed an optimization model with 8 parameters and concluded that optimization which is directly targeted minimizing DTE produced better results than an optimization study which aims to minimize LSTE.

In the this study, a MDOF model is also employed along with a SDOF model in order to investigate the differences between optimization results obtained by using different models. The objective in the optimization is set as reducing the peak-to-peak transmission error. The only parameter to be optimized is selected as the amount of tip relief, where the starting position of the modifications is set at the highest point of single tooth contact. A broad range of operating speeds along with various torque levels are covered in the case studies considered.

2 VALIDATION OF THE GEAR DYNAMICS MODEL USED FOR DTE OPTIMIZATION

There exists a variety of gear dynamics models in the literature, which can be categorized under many different groups. A comprehensive review of gear dynamics models can be found in the study of Özgüven and Houser (5), and more recently it is given by Wang *et al.* (6).

In the current study, first, the model proposed by Özgüven and Houser in 1988 (7) is used in optimization. This model is based on a validated approximation, which uses LSTE rather than static transmission itself, as an excitation to a SDOF model with an average constant mesh stiffness. The equation of motion of a gear pair is given in terms of dynamic transmission error, x , as:

$$m_e \ddot{x}(t) + 2\zeta \sqrt{m_e k_{ave}} \dot{x}(t) + k_{ave} x(t) = k_{ave} x_s(t) \quad (1)$$

Here m_e is the equivalent mass of the gear pair, ζ is the viscous damping ratio, k_{ave} is the average mesh stiffness and x_s is the loaded static transmission error. It was concluded that the displacement excitation resulting from time varying mesh stiffness is more important than the change in the system natural frequency resulting from the mesh stiffness variation. This model was shown to be a very effective one by using experimental results for gear pairs that have no profile modification. However, the accuracy of the model is not shown for gear pairs with profile modification, especially for gears with optimum tooth profile for a given load, where the resulting LSTE variation (hence the dynamic excitation) is at very low levels.

The following equation represents the differential equation of a SDOF model of a gear pair, in which time-varying mesh stiffness is used without any approximation:

$$m_e \ddot{x}(t) + c \dot{x}(t) + k(t)x(t) = F - m_e \ddot{e}(t) \quad (2)$$

In this model, c is the viscous damping coefficient, $k(t)$ is the time-dependent mesh stiffness, F is the constant gear mesh force and $e(t)$ is the static transmission error due to gear errors and profile modifications (also called non-loaded transmission error) (NLTE). In 2007, it has been shown by Tamminana *et al.* (8) that this model yields accurate results for gear pairs with profile modification, comparing theoretical DTE values with experimental data.

Although Equation (2) yields accurate results without making an approximation for the time-varying mesh stiffness, the model proposed by Özgüven and Houser (7) is preferred in several applications as it can be easily implemented to MDOF models of gears and gear-shaft-bearing systems, providing solutions in frequency domain. However, it is found necessary to study the accuracy of this model when it is used for gears with tooth modification where LSTE is minimized.

For this purpose, dynamic analysis of the gear system described in Table 1 is carried out using both of the models described above. The gear pair, which is composed of identical gears, has tooth modification such that LSTE variation is reduced to a very low level for a given torque value at which the dynamic analysis is performed. Thus, when the first model is used, as the internal excitation due to mesh stiffness variation is represented by LSTE, the level of excitation on the system becomes very low. Comparison of the dynamic analysis results obtained for such a case with those of the variable mesh stiffness model will reveal the accuracy of the constant mesh stiffness model when used for gears with optimum tooth profile modification.

Table 1 Properties of gear pair used for comparison of both models

Number of teeth	25
Module	4 mm
Equivalent mass	0.23 kg
Base diameter	93.97 mm

Face width	15 mm
Torque applied	107.9 Nm
Peak-to-peak LSTE (non-modified)	5.1 μm
Peak-to-peak LSTE (modified)	0.6 μm

Comparison is made for two damping ratio values, namely $\zeta = 0.1$ and $\zeta = 0.05$. Figure 2 and Figure 3 show the comparisons of DTEs by using both models for the specified damping values. Peak-to-peak DTE (PPDTE) values are plotted against normalized frequency, which is defined as $\sqrt{k_{ave}/m_e}$.

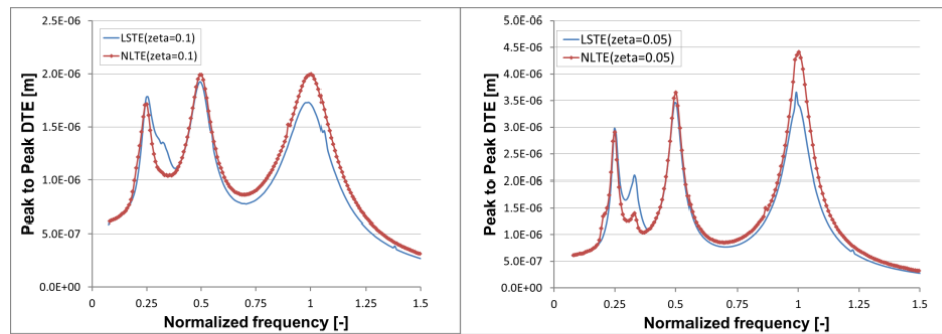


Figure 1 Model comparison for $\zeta = 0.1$ (left) and $\zeta = 0.05$ (right)

Although some minor discrepancies are observed between the results obtained by two models, recalling that these differences are observed only at a very extreme case where LSTE variation is minimum. It is concluded that results match well enough to safely continue with the constant mesh stiffness model in optimization studies, which makes it possible to use a MDOF model for the dynamic analysis of a gear-shaft-bearing system in frequency domain.

3 DESCRIPTION OF MDOF MODEL USED IN OPTIMIZATION STUDIES

Along with the SDOF model, a MDOF gear dynamics model which is based on the approximation proposed by Özgüven and Houser (7) is used while performing optimization studies. The model takes into account the shaft and bearing dynamics, onto which the gear pair is mounted. This model is a linear version of the model developed by Maliha *et al.* (9). Nonlinear effects due to backlash are not included in the model.

For the finite element modeling of the shafts, the axial motions are assumed to be negligible; hence, each node in the finite element model of a shaft will have five degrees of freedom (DOFs), i.e. 2 translational and 3 rotational DOFs. The flexible bearings are modeled in terms of radial stiffness and damping elements.

The gear pair is modeled by two disks, representing the inertia of the gears, which are connected to each other by a linear spring and a damper that represents the gear mesh. The system is excited by the displacement excitation represented by the LSTE. Further details of the model can be found in the study of Maliha *et al.* (8).

In both SDOF and MDOF models, the profile modification is represented by Fourier series with 5-harmonics which are found to be sufficient. The average mesh stiffness and the harmonics of LSTE, which are the necessary input parameters, are supplied to the dynamic model by using the computer code STEP (Spur Gear Transmission Error

Program) developed at the Ohio State University. A MATLAB code is developed in order to perform the dynamic analysis and optimizations required in this study.

3.1 Comparison of Results Obtained by SDOF and MDOF Models

The differences between the responses, in terms of PPDTE, obtained by using SDOF and MDOF models are presented for two different configurations. In the first configuration, the gear pair is mounted on relatively short (hence more rigid in transverse direction) shafts; whereas, for the second configuration, the same gears are mounted on longer shafts. Details of the gear-shaft-bearing systems under consideration are given in Table 2. It should be noted that all other properties except lengths of the shafts used in both configurations are identical and the bearings used at the ends of the shafts have the same stiffness and damping properties.

Table 2 Characteristics of the dynamic system

Gears	
Number of teeth	75
Module	3.2 mm
Equivalent mass	2.47 kg
Base diameter	232 mm
Face width	30 mm
Shafts	
Outer radius	55 mm
Inner radius	40 mm
Density	7800 kg/m ³
Elastic Modulus	206 GPa
Length of short shafts	0.1 m
Length of long shafts	1 m
Bearings	
Stiffness	1x10 ¹² N/m
Damping coefficient	1x10 ⁵ Ns/m

3.1.1 Short shafts

In the first example, gears are placed in the middle of the shafts that are 0.1 m long. The response of the system (DTE) for an arbitrary torque and profile modification in a wide speed range is shown in Figure 2. Note that ω_{norm} is the normalized shaft speed where the normalization is with respect to the natural frequency of the SDOF model. Investigating the figure, it can be clearly seen that responses of the SDOF model and the MDOF model are very close to each other due to the rigidity of the shafts considered. Therefore, it is expected that optimization studies carried out by using either of the models (SDOF or MDOF models), for this particular case, will lead to similar results.

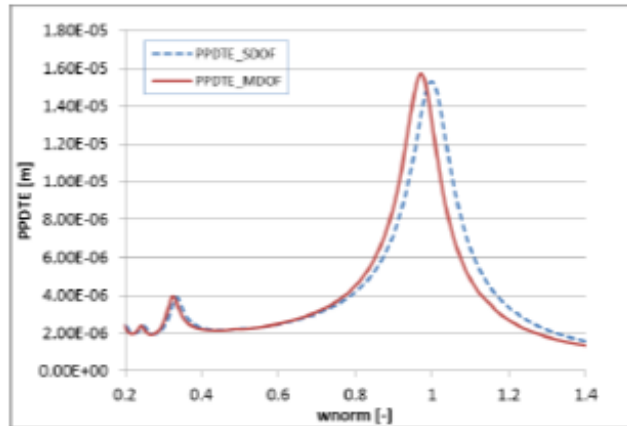


Figure 2 Response of MDOF and SDOF models for “short shafts” case

3.1.2 Long shafts

In the second case, gears are placed in the middle of 1 m long shafts. Figure 3 shows that, in this case, the shaft flexibility affects the total response of the gear pair considerably, and therefore SDOF and MDOF models yield relatively different results, as expected.

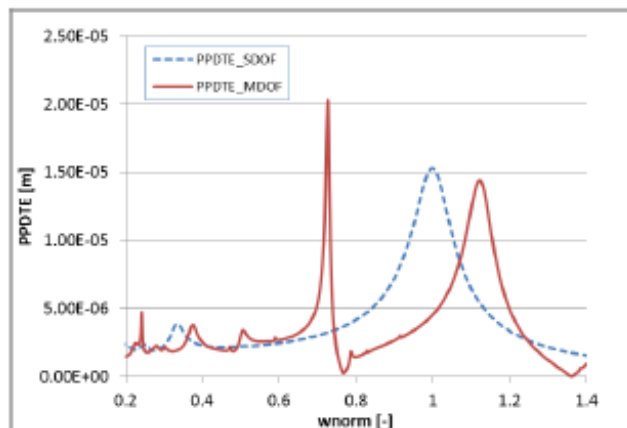


Figure 3 Response of MDOF and SDOF models for “long shafts” case

Figure 3 reveals that the coupled transverse-rotational modes along with the multi-harmonic LSTE input make the dynamic response more complex compared to the case of short shafts. In case those modes fall in the operating speed range, optimization using a SDOF or a MDOF dynamic model can make a significant difference. Note that this figure corresponds to an arbitrary torque and profile modification case, i.e. one may even find more differences between the results obtained with SDOF and MDOF models depending on the configurations and relative values of the system parameters.

4 OPTIMIZATION

The possible different dynamic responses due to using different dynamic models are revealed in the previous section. In this section, optimization is carried out by using both of the dynamic models, and optimum values obtained are compared. Optimum profiles

obtained by using DTE optimization are also compared with those calculated by using LSTE optimization. The objective of the optimization is set as the minimization of the maximum amount of peak-to-peak transmission error. The reason for such an objective function is to decrease the maximum value of the dynamic force at the gear mesh, which has the most dominant effect on the fatigue life of a gear pair. The only parameter to be optimized is selected as the amount of the linear tip relief. The starting positions of the modifications, which are applied to both gears, are fixed at the highest point of single tooth contact.

Since a single-parameter optimization study is carried out, a brute-force optimization technique is applied because of the respectively lower computational cost. For the whole set of possible profile modifications, a solution is performed at each point in the given parameter domain which is characterized by certain speed and torque ranges. The maximum of PPDTE value is thereafter extracted from the obtained responses for the respective profile modification and compared with the others. The profile modification which leads to the minimum of the maximum PPDTE is labelled as the optimum profile modification. Note that when LSTE optimization is made, only a single torque range is considered and the objective function is taken as the minimization of the maximum peak to peak LSTE.

Since the responses of SDOF and MDOF models differ significantly from each other for longer shaft case, in the rest of this study, optimization is performed for only the long shafts configuration defined in section 3.1.2,

4.1 Results

In this section, some example cases are presented in order to show the differences between the optimization results obtained from different models. The details of the example cases can be found in Table 3. Note that in all cases, the design torque is taken as 1000 Nm.

Table 3 Details of the example cases

Case 1	
Torque range	50-100% of design torque
Speed range	2200-2400 rpm
Initial modification	3 μm
Modification increment	5 μm
Case 2	
Torque range	0-50% of design torque
Speed range	1600-1800 rpm
Initial modification	0 μm
Modification increment	5 μm
Case 3	
Torque range	20-40% of design torque
Speed range	1600-1800 rpm
Initial modification	2 μm
Modification increment	2 μm
Case 4	
Torque range	80-100% of design torque
Speed range	1000-1200 rpm

Initial modification	10 μm
Modification increment	2 μm
Case 5	
Torque range	0-20% of design torque
Speed range	600-800 rpm
Initial modification	0 μm
Modification increment	2 μm

For the first two cases, where optimization in a wide torque range is considered, the comparisons are made between the optimization results obtained through the static, SDOF-dynamic and MDOF-dynamic models. The results (normalized with respect to the minimum of the maximum PPDTE obtained) for these cases are presented in Figure 4.

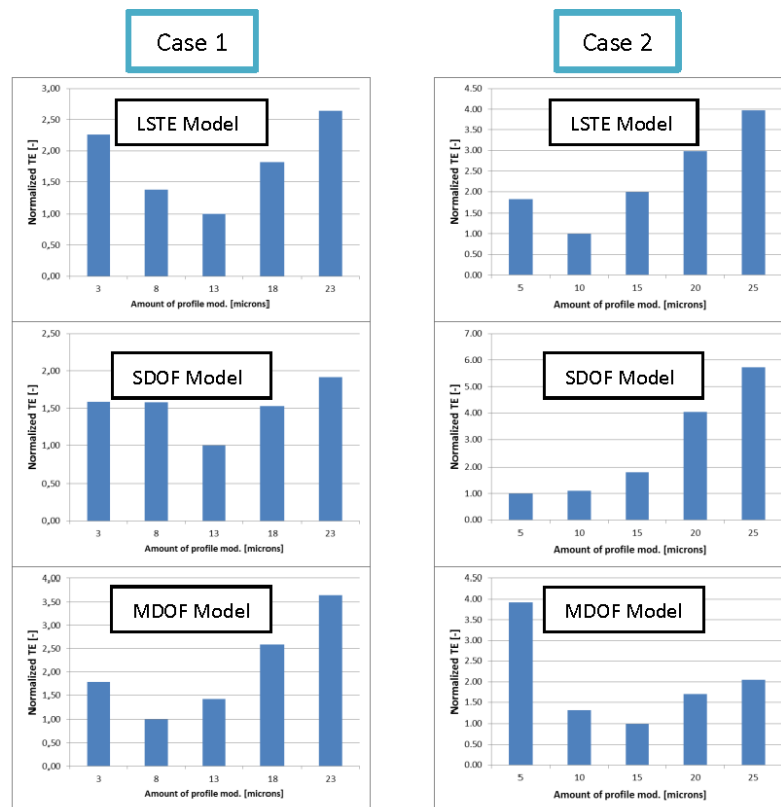


Figure 4 Sample optimization results for Case 1 and Case 2

It is observed from the results obtained that, for Case 1, while the SDOF model proposes the 3rd modification (i.e. 18 μm) as the optimum one, which is also proposed by the LSTE model, the MDOF model suggests that the minimum DTE is obtained when the 2nd modification (i.e. 13 μm) is applied to the gear teeth. In Case 2, the difference between the optimum profile modifications proposed by the SDOF model (5 μm) and MDOF model (15 μm) is as large as 10 μm . The differences between LSTE based optimization and DTE based optimization are also clearly observable for Case 2, which are in accordance with the findings of the study of Faggioni et.al. (4).

In Case 3-Case 5, torque ranges considered in the optimization are limited to 20% of the design torque. The increment of profile modification is kept as low as 2 μm , in order to observe if discrepancies still exist between the results of different models even under such minor modification differences. For these cases, only the comparison of the optimization results between SDOF and MDOF models are considered and the results are given in Figure 5.

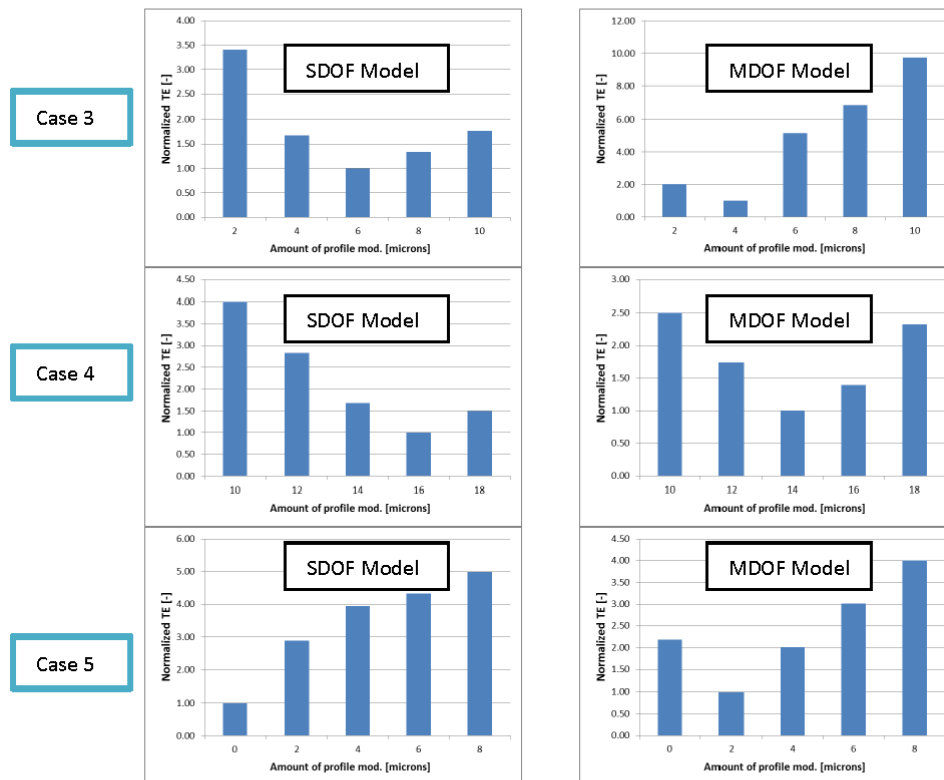


Figure 5 Sample optimization results for Case 3, Case 4 and Case 5

In this case study, the torque range considered is smaller compared to that of the previous case study; hence, the optimum profile modifications obtained from the SDOF and MDOF models are slightly different from each other. The comparison of the results obtained by using SDOF and MDOF models for the same gear system indicates that those differences can be more important under the influence of operational conditions. Case 3 can be used to explain the differences. SDOF model suggests that, considering wear on the gears, the 1st modification (2 μm) can be preferred instead of the 2nd modification (4 μm), which is the optimum one, since DTE increases significantly if due to tooth wear profile modification reaches to 6 μm . However, if MDOF model is used, the 3rd modification (6 μm), which is the optimum one, can be used, since the increase, as well as the rate of increase in DTE is small even wear occurs.

5 CONCLUSIONS

In this study, profile modification optimization is performed using 3 different models. The first model is based on the minimization of LSTE variation. In the second and third models, profile modification optimization is achieved through minimization of DTE

variation. The second model considers only the spur gear pair dynamics, whereas the third one, which is a MDOF model, takes also the effects of shaft and bearing dynamics into account. The differences between the optimization results obtained by the mentioned models are studied.

For the second and third models, which consider the dynamics of the respective systems, gear pair dynamics is modeled based on a previous study by Özgüven and Houser (5). The mentioned model employs the approximation of using an average value for gear mesh stiffness and includes the effect of mesh stiffness variation through a displacement excitation in the form of LSTE. This model is preferred in this study, since it can be easily implemented to a MDOF model, providing solutions in frequency domain. In order to verify the accuracy of the model for the cases where optimum profile modifications are used and therefore very small LSTE variations are observed, first a comparison is made between DTEs obtained through this model and an exact gear dynamics model, which employs time-variant mesh stiffness. The comparison revealed that the invariant mesh stiffness approximation can also be used in the dynamic analysis of gear pairs where LSTE excitation is at very low levels.

Before proceeding with optimization, possible different outcomes of using SDOF and MDOF models are investigated on two different cases. The first case with shorter shafts represents a relatively rigid configuration of a gear-shaft-bearing system, whereas the second case is an example of a significantly more compliant system. The results obtained through both models turned out to be very similar for the first case. However, for the second system under consideration, the responses obtained with SDOF and MDOF models are found to be considerably different from each other, as expected. It is shown that when combined with multi-harmonic excitation, the complex dynamic nature of compliant systems resulting from coupled transverse-rotational modes observed in operational speed ranges makes MDOF models more suitable to be used in optimization studies.

In optimization studies, differences are observed between the best profile modifications suggested by LSTE-based model and those obtained by using optimization models based on DTE minimization. This observation is in line with the findings of Faggioni *et al.* (4). In this study, the main emphasis is placed on the comparison of the optimization results obtained from SDOF and MDOF dynamic models. Important differences are observed between the optimum profile modifications obtained by SDOF and MDOF dynamic models for gears on compliant shafts. It is therefore concluded that the optimum tooth profiles obtained by considering only the dynamics of a gear pair may not represent the best tooth profile modification when these gears are on flexible shafts and/or bearings. It has been also shown that when parameters such as quality of manufacturing and wear of the gears are of concern, such differences can be even more important. Therefore, it can be said that for compliant systems, neglecting the shaft and bearing dynamics and employing SDOF gear dynamics models may lead to incorrect decisions for determination of the optimum profile modification.

Finally, it should be noted that in this study only the amount of tip relief is taken as a parameter to be optimized. However, when more parameters such as shape of the profile modification (linear, parabolic) and the starting position (in terms of roll angles) of profile modifications are included in the optimization study, the differences between the results obtained from SDOF-based and MDOF-based optimization models may be even more significant.

employing SDOF gear dynamics models may lead to incorrect decisions for determination of the optimum profile modification.

Finally, it should be noted that in this study only the amount of tip relief is taken as a parameter to be optimized. However, when more parameters such as shape of the profile modification (linear, parabolic) and the starting position (in terms of roll angles) of profile modifications are included in the optimization study, the differences between the results obtained from SDOF-based and MDOF-based optimization models may be even more significant.

6 REFERENCES

- (1) Tavakoli M.S., Houser D.R. (1986), Optimum profile modifications for the minimization of static transmission errors of spur gears, *Journal of Mechanism Transmissions and Automation in Design*, **108**, 86–95.
- (2) Fonseca D.J., Shishoo S., Lim T.C., Chen D.S. (2005), A genetic algorithm approach to minimize transmission error of automotive spur gears sets, *Applied Artificial Intelligence*, **19**, 2, 153–179.
- (3) Bonori G., Barbieri M., Pellicano F. (2008), Optimum profile modifications of spur gears by means of genetic algorithms, *Journal of Sound and Vibration*, **313**, 603–616.
- (4) Faggioni M., Samani F. S., Bertacchi G. Pellicano F. (2011), Dynamic optimization of spur gears, *Mechanism and Machine Theory*, **46**, 544–557.
- (5) Özgüven H.N., Houser D.R. (1988), Mathematical models used in gear dynamics - A review, *Journal of Sound and Vibration*, **121**, 3, 383–411.
- (6) Wang J., Li R., Peng X. (2003), Survey of nonlinear vibration of gear transmission systems, *Applied Mechanics Rev.*, **56**, 3, 309-329.
- (7) Özgüven H. N., Houser D. R. (1988), Dynamic analysis of high speed gears by using loaded static transmission error, *Journal of Sound and Vibration*, **125**, 71–83.
- (8) Tamminana V.K., Kahraman A., Vijayakar S. (2007), A study of the relationship between the dynamic factors and the dynamic transmission error of spur gear pairs, *Journal of Mechanical Design*, **129**, 75-84.
- (9) Maliha R., Dogruer C., Özgüven H.N. (2004), Nonlinear dynamic modeling of gear-shaft-disk-bearing systems using finite elements and describing functions, *Journal of Mechanical Design*, **126**, 536-541.

CURRICULUM VITAE

PERSONAL INFORMATION

Surname, Name: Öztürk, Veysel Yalın
Nationality: Turkish (TC)
Date and Place of Birth: 11 June 1985, Muş
Marital Status: Married
Email: e139323@metu.edu.tr

EDUCATION

Degree	Institution	Year of Graduation
MS	RWTH Aachen Automotive Engineering	2010
BS	METU Mechanical Engineering	2007
High School	Ankara Atatürk Anadolu High School, Ankara	2003

WORK EXPERIENCE

Year	Place	Enrollment
2010-Present	Turkish Aerospace Industries (TAI)	Senior Structural Analysis Engineer
2006 July	Bosch Türkiye A.Ş.	Intern Engineering Student
2005 July	ASELSAN	Intern Engineering Student

PUBLICATIONS

1. Y. Öztürk , E. Ciğeroğlu and H. N. Özgüven “Optimization of Tooth Bending Fatigue Characteristics of Spur Gear Pairs using a Gear Dynamics-based Approach,” in *ASME 2015 International Design Engineering Technical Conferences*, 2015.

2. V. Y. Ozturk, E. Cigeroglu, and H. N. Özgüven, “Optimum profile modifications for the minimization of dynamic transmission error,” in International Gear Conference 2014, 2014, pp. 596–605.